Past Earth System Sensitivity:

Forcing and feedback mechanisms on orbital timescales using regional and global models

Dissertation zur Erlangung des akademischen Grades
Doktor der Naturwissenschaften (Dr. rer. nat.)

vorgelegt von Michael Stärz
geb. in Pegnitz
Fachbereich Physik und Elektrotechnik,
Universität Bremen.

Mai 2013

Abstract

Orbital parameters are assumed to drive glacial/interglacial cycles. However, pre-Quaternary (>2.7 myr ago) glacial cycles do not exhibit distinctive glacial amplitudes in the geological record. An atmosphere-ocean general circulation model (GCM) with dynamic vegetation is used for an extensive suite of studies, comprising changes in obliquity and precession, differential atmospheric CO_2 values and climate background states representative for Pre-industrial, and Tortonian (11–7 myr), a relatively warm climate state prior Northern Hemisphere glaciation, is set up to test the sensitivity of climate. The model results show that the magnitude of impact of external insolation forcing is most dependent on atmospheric CO_2 values and, to a lesser degree, on the background climate. Depending on the actual state of the climate system, sea-ice has been identified as a key regulator for mediating orbital forcing into a nonlinear climate response at high latitudes. This high latitude feedback has potential implications for Cenozoic hothouse climate as well as glacial inception.

GCMs are tested and challenged by the ability to reproduce paleoclimate key intervals. In order to account for climate changes associated with soil dynamics, a soil scheme is developed, which is asynchronously coupled to a state-of-the-art atmosphere-ocean GCM with dynamic vegetation. The scheme is tested for conditions representative of a warmer (mid-Holocene, 6 kyr before present, BP) and colder (Last Glacial Maximum, 21 kyr BP) than pre-industrial climate. For these different climates the computed change in considered physical soil properties (i.e. albedo, total water holding field capacity, and texture) leads globally to an amplification of climate anomalies. Especially regions like the transition zones between desert/savannah and taiga/tundra, exhibit an increased response as a result of the modified soil treatment. In comparison to earlier studies, the inclusion of the soil feedback pushes the model simulations towards the warmer end in the range of mid-Holocene studies and beyond current model estimates of global cooling during the Last Glacial Maximum (LGM). The main impact of the interactive soil scheme on the climate response is governed via positive feedbacks, including vegetation dynamics, snow, sea-ice, local water recycling, which might amplify forcing factors ranging from orbital to tectonic timescales.

Due to the lack of spatially and temporally sufficiently resolved reconstructions, the extent, thickness and drift patterns of sea-ice and icebergs in the glacial Arctic remains poorly constrained. Earlier studies are contradictory and propose either a cessation of the marine cryosphere, or an ice drift system operating like present-day. Here, the marine Arctic cryosphere during the LGM is examined using a high-resolution, regional ocean-sea-ice model. Whereas in the modern western Arctic Basin sea-ice can circulate in the Beaufort Gyre for decades, glacial model studies present an extreme shortcut of sea-ice drift. The results show a clockwise sea-ice drift in the western Arctic Basin that merges into a direct trans-Arctic path towards Fram Strait. This is consistent with dated ice plough marks on the seafloor which show the orientation of iceberg drift in this direction. Also ice-transported iron-oxide grains deposited in Fram Strait, can be matched by their chemical composition to similar grains found in potential sources from the entire circum-Arctic. The model results indicate that the pattern of Arctic sea-ice drift during the LGM is established by wind fields and seems to be a general feature of the glacial ocean. Contradicting to former proxy reconstructions the model results do not indicate a cessation in ice drift during the LGM.

Contents

Chapter 1

Introduction

1.1 Motivation

The last 65 myr of Earth's climate has undergone dramatic changes during the Cenozoic (Zachos et al., 2001). The general evolution within the Cenozoic Era has been characterized by hothouse to icehouse conditions via a long-term climate cooling paced by superimposed fluctuations (orbital parameters), trends (greenhouse gases, plate tectonics) and impacts (ocean gateway configurations, mountain uplift, ice sheet evolution) (Zachos et al., 2001; Pagani et al., 2005). One feature of hothouse climate, also known as "equable climate", is the markingly attenuated meridional temperature gradient mostly due to a more temperate polar climate (Jenkyns et al., 2004; Moran et al., 2006; Huber and Caballero, 2011; Salzmann et al., in revision). Several proposals of solution have been submitted dealing with vegetation dynamics (Otto-Bliesner and Upchurch, 1997), enhanced oceanic vertical mixing and polar heat transport (Sloan et al., 1995), and raised methane levels as well as heightened polar stratospheric clouds (Sloan and Pollard, 1998). As exemplified by the Pliocene Epoch, Fedorov et al. (2013) point out that, by means of a numerical climate model, all combined equable climate state characteristics cannot be simultaneously reproduced despite considering these potential mechanisms. Neither is the multi-model ensemble able to reproduce the low temperature gradient between low and high latitudes suggested by proxy data (Salzmann et al., in revision). Alternatively, the proxy record of the mid-Pliocene warm Period (3.3–3 myr before present, BP) can be interpreted as an integrated signal of multiple orbital cycles, since orbital time frequencies in the order 10–100 kyr are within the geological dating error. Earth system models of intermediate complexity show that the seasonal and latitudinal variation of solar energy at orbital timescales can be transferred via ice-sheet and vegetation feedbacks into an amplified annual temperature signal, thus fitting modelled temperatures of warm orbits more closely to reconstructions (Willeit et al., 2013).

Orbital Parameters. As climate cooling crossed a critical threshold, gradual Northern Hemisphere and therefore bipolar glaciation appeared (ca. 3 myr BP). The evolution of the Greenland ice-sheet is traditionally hypothesized to amplify the orbital signal, which leads to strengthened glacial/interglacial cycles of the Quaternary (Lisiecki and Raymo, 2005). In general, the orbital signal forces ice-sheet growth with a linear lag-phase of 5 kyr

(Milankovitch, 1941). Further, the ice-driven feedback might result in an atmospheric CO_2 response, amplifying the initial signal (Ruddiman, 2006a,b). However, prior to Greenland ice-sheet growth, the impact of orbital parameters on high level CO_2 climate sensitivity might have been different relative to the Quaternary glacial/interglacial cycles (Ruddiman, 2006b). Hypothetically, the interplay of orbital parameters under a warmer climate state (Sloan and Morrill, 1998) effects nonlinear feedbacks in the Earth system, amplifying or dampening synergies.

Soil evolution. Currently, the inability of state-of-the-art General Circulation Models (GCMs) to reproduce an equable climate at hothouse conditions, or high amplitude glacial/interglacial cycles within, versus low amplitudinal cycles prior the Quaternary raise the question of potentially absent feedback mechanisms in the models (e.g. ice-sheet interactions, radiative dust forcing, permafrost and wetland dynamics). For instance, now GCMs have the ability to resolve land surface characteristics via the explicit simulation of dynamic vegetation, while its importance has been recognized already 30–40 yr ago. As an alternative approach reconstructed paleo vegetation maps serve as a tool for prescribing terrestrial vegetation as land surface boundary conditions for the models. Nevertheless, another disregarded potential feedback—though pointed out by multiple modeling studies—is soil gradation. Since soil evolution occurring on timescales of years to kilo years (Jenny, 1941), it is not only essential for deep past climate, but also for last glacial/interglacial alterations. Model sensitivity experiments, set up for the warmer than present-day mid-Holocene (6 kyr BP) and Last Glacial Maximum (21 kyr BP), have shown some response in transitional climate regimes like the African Sahel boundary and the North Siberian taiga/tundra treeline.

Glacial Arctic Ocean. The Arctic Ocean is of special interest because it fosters amplified climate changes for past, present and future projections and is known to be a driver of the global climate system. North Siberia, embedded in the Arctic region, is interacting with the Arctic Ocean through several feedback mechanisms. An initial warming perturbation causes sea-ice decrease. This exposes ocean water and thus drastically decrease sea surface albedo and subsequently causes ocean surface warming, which gives a rise to further ice melting. Regional warming in the Arctic represses land snow cover resulting in low surface albedo, transferring more solar energy into sensible heat. A third mechanism comes into play when warming endures for several decades, i.e. the timescale of vegetation migration. A northward shift of the forest treeline, caused by warming perturbations, can reduce planetary albedo via canopy masking the snow on the ground. All three mechanisms have a positive feedback on each other, amplifying polar climate. During the LGM, these three mechanisms (together with ice-sheet dynamics) positively interacted with climate, and reinforced polar cooling, isolating the Arctic region as a consequence. Due to isolation and severe conditions, marine and terrestrial geological remnants of the glacial Arctic are quite sparse. As yet there is hardly any knowledge of the glacial Arctic Ocean water characteristics, sea-ice dynamics, and its influence on the North Atlantic and vice versa. Due to the lack of data and strongly reduced sediment fluxes, the glacial Arctic Ocean is supposed to be blocked from the atmosphere by a permanent ice lid. Nevertheless, several partly contradicting hypotheses about characteristics and dynamics of the glacial Arctic ice-cover have been raised. So far, global climate models tested for a much colder state of climate variability, like the Last Glacial Maximum, are not reliable in reproducing the Arctic Ocean system and reveal a lack in capturing its full

dynamics.

1.2 Research questions

Climate Sensitivity is defined by the equilibrium global temperature anomaly caused by changes in radiative forcing (modulated by fast feedbacks, i.e. water-vapor, cloud, lapse-rate, snow, sea-ice), more precisely by a doubling of CO_2 concentrations in the atmosphere. The term 'Earth system sensitivity' encompasses climate sensitivity and further considers slow feedbacks (e.g. vegetation migration, land ice-sheets, carbon cycle, plate tectonics,...) in calculations of the global energy balance (PALEOSENS Project Members; Rohling et al., 2012). Due to its uncertainty proxy data of the geological past usually show a time integrated climate signal rather reflecting Earth system sensitivity than climate sensitivity (e.g. Lunt et al., 2010). Present state-of-the-art climate models are tested and evaluated for these past climate states (Braconnot et al., 2007, 2012; Haywood et al., 2013). This work targets, by applying numerical climate models, for a better understanding of Earth system sensitivity by focusing on potential regions of strong nonlinear behavior (Arctic region), regarding potential feedback mechanisms (soil gradation), and testing the sensitivity of external orbital timescale forcing.

The present work is structured chapter-wise, beginning with the formulation of research questions in the introduction, followed by a methodological part and model description in Chap. 2. Subsequently, Chap. 3, 4 and 5 address a specific research question, the results are discussed and conclusions are drawn therein. The work finishes with main conclusions and an outlook in Chap. 6. Here, the scientific questions will be specified in more detail.

- In **Chapter 3**, the interplay of orbital parameters within a warmer than pre-industrial world is analyzed. As a null-hypothesis, the climate impact of orbital parameters in a warmer world is indifferent to the Pre-industrial. If this hypothesis is rejected, how strong can CO_2 modulate the imprint of the orbital signal into climate? Can atmospheric CO_2 changes mimic a temperature anomaly, which is originally caused by changes of orbital parameters? The Tortonian climate (11–7 myr ago) serves as an adequate test ground, because background climate was about 3°C warmer than present-day with only partial or ephemeral land ice on Greenland, excluding the potential ice-sheet feedback in the Northern Hemisphere. The Tortonian Stage encompasses multiple cycles of orbital harmonics in its time frame, allowing to vary orbital parameters within its natural limits. Furthermore, CO_2 levels can be modulated in sensitivity studies, in the range of proxy uncertainty (278–450 parts per million volume in the atmosphere, ppmv) (Tripati et al., 2009; van de Wal et al., 2011). The Miocene, including the Tortonian, is characterized by relatively stable CO_2 values in the atmosphere decoupled from major climate reorganizations within this time period (Pagani et al., 2005). The orbital signal (obliquity and precession) is supposed to be imprinted in geological data, though prior to the Pliocene-Pleistocene transition the amplitudes, shown in the $\delta^{18}O$ (ratio of stable oxygen isotopes) signal of benthic foraminifera were strongly extenuated (Lisiecki and Raymo, 2005). Traditionally, the orbital signals are thought to force ice-sheet dynamics in a glacial world. A suite of sensitivity studies performed with a GCM elaborate these effects by using end members of obliquity and precession at high values of eccentricity versus pre-industrial and Tortonian background conditions. Further, the

set of orbital parameter experiments at Tortonian background conditions is modulated once by pre-industrial CO_2 levels (278 ppmv) and once by elevated atmospheric CO_2 content (450 ppmv) to disentangle the effect of CO_2 forcing and climate background conditions.

- **Chapter 4** deals with dynamics of land surface characteristics in a GCM. State-of-the-art GCMs encompass changes of land surface conditions with respect to vegetation dynamics, but disregard possible feedbacks, i.e. evolving physical soil characteristics. The Chapter addresses the question how soil impacts trend and intensity of climate and due to this, how it feeds back to climate. Do soil characteristics evolve linearly in a warmer and in a colder than pre-industrial scenario? Which regions are most sensitive to soil changes and via which mechanisms of the climate system do they interact with? In a first step, the author, in companion with colleagues, created a simple soil scheme, which diagnoses physical soil characteristics based on terrestrial vegetation dynamics and by the assumption of temperature thresholds. Secondly, the soil scheme is asynchronously coupled with an atmosphere-ocean GCM with vegetation dynamics. The fully integrated impact of soil dynamics is exemplified in time-slice experiments of the mid-Holocene and the LGM (Stärz et al., 2013).

- In **Chapter 5** the reader is introduced to hypotheses of the enigmatic glacial Arctic Ocean (Stärz et al., 2012). Questions raised in this context are: How dynamic are the marine and cryospheric components of the glacial Arctic Ocean? Is there interaction via the single glacial Arctic Ocean gateway, the Fram Strait, for Northern North Atlantic waters and vice versa? For the first time the author and colleagues apply a well-established high-resolution Arctic ocean/sea-ice model to boundary conditions of the Last Glacial Maximum and compare the results with proxy data. This model is currently used for operational sea-ice cover predictions in the "integrated Arctic observing system" as benefit for instance for ship routing (Kauker et al., 2009). The author and colleagues propose a new hypothesis of glacial Arctic sea-ice dynamics based on a collection of proxy records and regional modeling outcomes.

Within this work, hypotheses and research questions indicated above are tested by numerical models. Whereas studies of the glacial Arctic Ocean require the usage of a regional model (NAOSIM—North Atlantic/Arctic Ocean Sea-ice Model) to resolve detailed spatial aspects, the analysis of (soil-) feedbacks and insolation sensitivity of the Earth's climate is held by studies with a GCM (COSMOS—Community of Earth System Models).

Chapter 2

Methods and model description

2.1 COSMOS

The Community of Earth System Models (COSMOS) used in this study consists of three coupled model components (atmosphere, ocean, land surface). The atmospheric component is the ECHAM5 model (Roeckner et al., 2003) with a spectral resolution of T31 (3.75°) and L19 (19 layers in the vertical dimension) which is an adequate compromise between sufficient resolution and CPU time for longer simulation length (Roeckner et al., 2006). The ocean model MPI-OM uses an orthogonal curvelinear grid (size of a grid cell ca. 1.5°), characterized by high grid resolution at deep water formation areas of the Labrador Sea and the Weddell Sea near the grid poles (Greenland, Antarctica; see Stepanek and Lohmann, 2012). The model comprises 40 layers in vertical space (Marsland et al., 2003). The transfer of fluxes and momentum between atmosphere and ocean is handled by the coupler OASIS3 without any flux corrections (Jungclaus et al., 2006). The modular land surface scheme JSBACH (Raddatz et al., 2007) with a dynamic vegetation module (Brovkin et al., 2009) is embedded in the ECHAM5 atmosphere model.

JSBACH is based on the semi-empirical terrestrial ecosystem model BETHY, which incorporates an energy and water balance, photosynthesis, phenology (not used in our approach because of the simulation of dynamic vegetation) and a carbon balance compartment (Knorr, 2000). JSBACH is using a tiling approach in which the actual cover fraction of each plant functional type (PFT) is associated to a tile for each grid cell. If the grid cell is not fully covered by the sum of all tiles, the residual is interpreted as bare soil. In our studies JSBACH is using the standard model configuration of eight PFTs that can potentially cover each grid cell. The land surface energy balance incorporates soil albedo, leaf area index of the actual PFTs, the albedo of stems, snow fraction on the ground and on canopy, and the masking effect of snow under canopy. Further background information of the COSMOS model suite and its components can be found in Jungclaus et al. (2006). So far, COSMOS has been applied to various paleo setups including the Holocene (Wei et al., 2012; Wei and Lohmann, 2012; Varma et al., 2012), the Last Glacial Maximum and MIS3 (Zhang et al., 2012; Gong et al., 2013), the Last Interglacial (Lunt et al., 2013), the Pliocene (Stepanek and Lohmann, 2012) and the Tortonian (Knorr et al., 2011).

2.1.1 Orbital sensitivity studies

Here, we use the COSMOS GCM (Chap. 2) for orbital sensitivity studies. Temporal and spatially resolved solar radiation, based on the orbital configuration, is calculated following Berger (1978). Earth's orbital parameters are set to favor a "warm" (maximum obliquity and

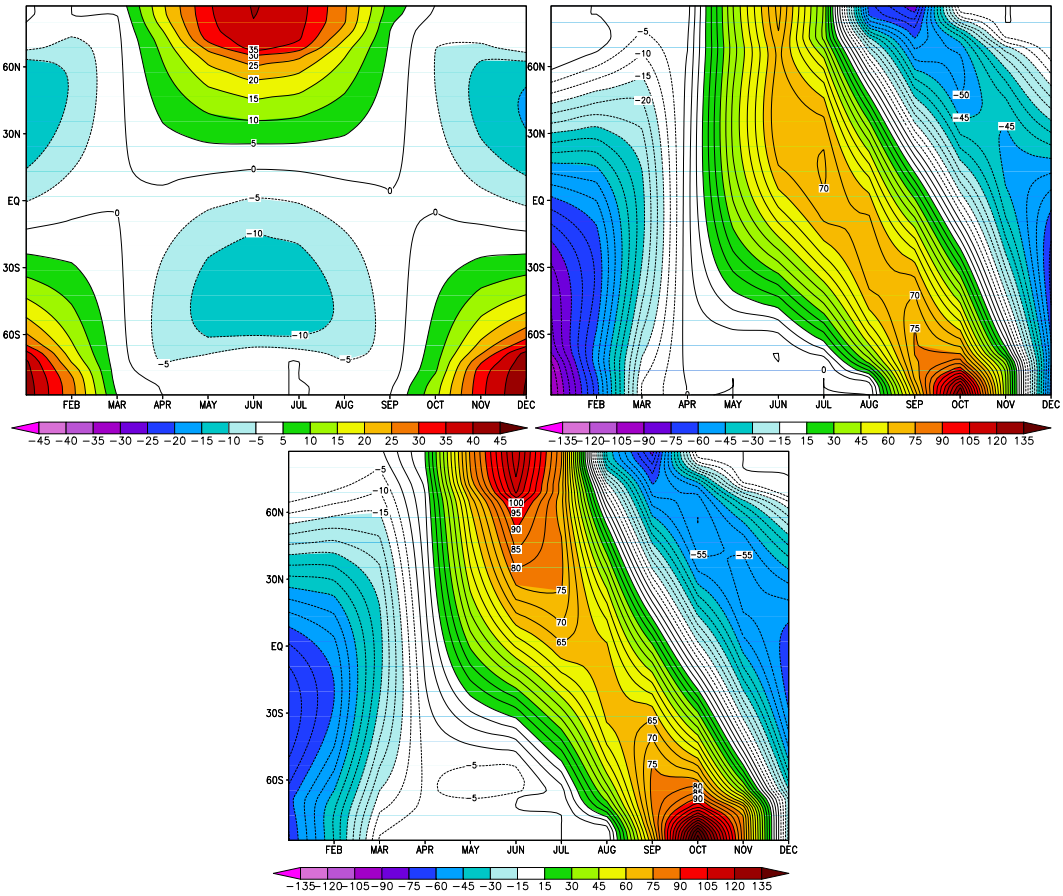

Figure 2.1.1: Global anomaly of seasonal and latitudinal insolation forcing ($W\,m^{-2}$) of high obliquity (upper left), perihelion in summer solstice (upper right), and the combination of both orbital parameters with respect to a "cold orbit" setting (low obliquity and perihelion in winter solstice). In all experiments eccentricity of the Earth's orbit is set on high value (0.04).

minimum precession) versus a "cold orbit" (minimum obliquity and maximum precession), while eccentricity is kept constant (Fig. 2.1.2; Table 2.1). The monocausal impact, and the combination of precession and obliquity forcing, are disentangled from the synergy, using a strategic suite of model studies (Table 2.1). Furthermore via orbital sensitivity studies are performed for pre-industrial (Wei et al., 2012) and Tortonian (Knorr et al., 2011) boundary conditions to test orbital impact on different climate states. The Tortonian setup differs from the Pre-industrial with respect to gateway configurations (opened Central American Seaway,

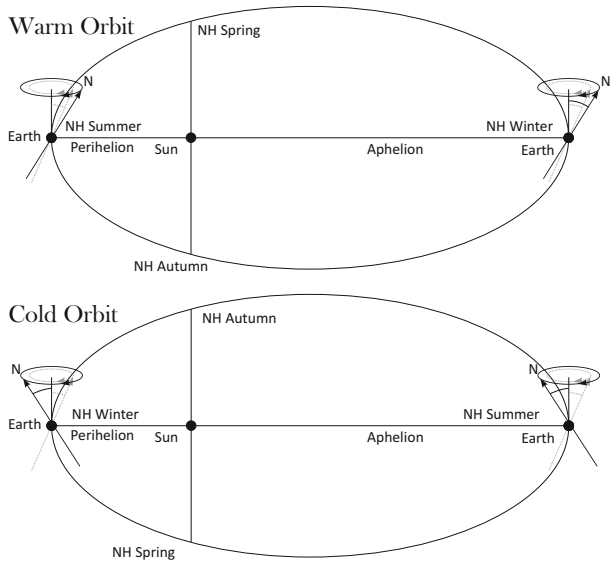

Figure 2.1.2: Earth's parameter configuration for a "warm orbit" in the upper panel versus a "cold orbit" in the lower panel. In both cases eccentricity of the orbital ellipse is set on high value.

closed Hudson Bay), landmass distribution (southward shift of Australia), orogenesis (i.e. lowered Tibetan Plateau, South American Andes, Alps, Rocky Mountains), and removal of the Greenland Ice-Sheet (Knorr et al., 2011; Micheels et al., 2011). In order to isolate CO_2 forcing from Tortonian boundary conditions, the orbital model studies are performed with pre-industrial CO_2 levels of (278 ppmv) and a high end member (450 ppmv) of reconstructed CO_2 for the Tortonian (Pagani et al., 2005; Hönisch et al., 2009; Tripati et al., 2009; van de Wal et al., 2011; Table 2.1), following the approach of Stein and Alpert (1993). The starts starts with equilibrated climate conditions for Tortonian (Knorr et al., 2011) and Pre-industrial (Wei et al., 2012). In total 12 model studies are being performed. Each run 500 model years whereof the last 100 yr are analyzed.

In order to test the sensitivity of climatic evolution on obliquity forcing at changing atmospheric CO_2 levels, we run another two model studies initialized with high atmospheric CO_2 levels (450 ppmv) steadily decreasing towards the pre-industrial CO_2 level (Sect. 3.3.5). The slope of the linear CO_2 ramp is -1 ppmv yr^{-1}. The two model studies differ by high and low end members of obliquity (Table 2.1). The focus of this study is rather on a mechanistic understanding of the forcing factors and the fast response of Northern Hemisphere sea-ice evolution since slow components of the climate system (ocean and vegetation dynamics) cannot adjust to the fast varying CO_2 forcing.

Table 2.1: Strategic suite of obliquity, precession, and atmospheric CO_2 end members. Eccentricity is fixed at high values (0.04) in order to reinforce the precession signal. The set of model studies is annexed by two transient CO_2 ramp studies.

simulation	obliquity (°)	precession (° from vernal equinox)	CO_2 level (ppmv)
PI_wO_wP_278	24	113.5	278
PI_wO_cP_278	24	293.5	278
PI_cO_wP_278	22	113.5	278
PI_cO_cP_278	22	293.5	278
TO_wO_wP_278	24	113.5	278
TO_wO_cP_278	24	293.5	278
TO_cO_wP_278	22	113.5	278
TO_cO_cP_278	22	293.5	278
TO_wO_wP_450	24	113.5	450
TO_wO_cP_450	24	293.5	450
TO_cO_wP_450	22	113.5	450
TO_cO_cP_450	22	293.5	450
TO_wO_cP_450–278	24	293.5	450→278
TO_cO_cP_450–278	22	293.5	450→278

2.1.2 The soil scheme—Upgrading the vegetation module JSBACH

This part of the dissertation addresses the principles of a soil scheme and its coupling to JSBACH. Subsequently, in Chap. 4 the scheme is tested and discussed.

Design of the soil scheme

Physical soil properties are dependent on the accumulation of organic matter and therefore of the specific vegetation type above (e.g. Vamborg et al., 2011). Moreover, observational data to total water holding field capacities of soils are limited and tuned to optimized rooting depths in order to fit to vegetation demands (Hagemann et al., 1999). In our approach, pedogenetic factors like climate and topography are indirectly captured by simulated vegetation distribution whereas parent material is ignored. The soil parameters (soil albedo, maximum water holding field capacities of soils) are determined from integrated PFTs of each grid cell using the dynamic land surface model JSBACH (Fig. 2.1.3). For each grid cell the contribution of all area-weighted soil tiles creates a mean of soil characteristics. All time-slice experiments start from a quasi-equilibrium climate state. The 1st iteration is based on averaged 100 yr of model output to calculate physical soil properties (soil albedo in the spectrum of visible and near-infrared light, soil data flags FAO, maximum water holding field capacity of soils). After the first iteration, the model is run for 600 yr in total with an asynchronous coupling timestep of 200 yr, again taking the preceding 100 yr of model output as input for the soil scheme (Fig. 2.1.3). The final 100 yr of model output and physical soil characteristics of the 3rd iteration are used for analysis.

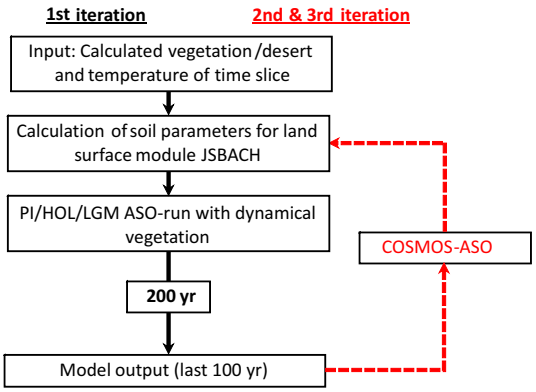

Figure 2.1.3: Flowchart of asynchronous coupling procedure between soil scheme and COSMOS-ASO.

Look-up table of the soil scheme

The conventional soil parameters in JSBACH comprise the snow-free soil albedo in the visible (0.3–0.7 µm) and near infrared (0.7–3 µm) light spectrum, the total water holding capacity of soil (h_{cws}), and soil data flags from the United Nations Food and Agriculture Organization (FAO) soil classification (Hagemann et al., 1999; Rechid et al., 2009). The original data set of snow-free soil albedo has been derived from modified satellite measurements of the Moderate Resolution Imaging Spectroradiometer (MODIS) (Rechid et al., 2009). FAO soil data flags are based on Gildea and Moore (Henderson-Sellers et al., 1986), and range from sand (1) to loam (3) and clay (5). The assessment of h_{cws} in global and regional modeling is quite uncertain and is estimated from a data set of the permanent wilting point (h_{pwp}) and the maximum amount of water that plants may extract from the soil before they start to wilt (h_{ava}), based on optimized rooting depths (Hagemann et al., 1999). In our model-consistent approach, the association of soil properties to PFTs is developed using the last 100 yr output of a 2000 yr pre-industrial equilibrium model run (Wei et al., 2012). The main properties of defined soil tiles are displayed in its latitudinal distribution (Fig. 2.1.4). Only dominant cover fractions of modeled PFTs (>50% cover per grid cell) are considered to create associated soil tiles. This approach is extended by adding soil tiles for global desert fraction (defined as the fraction within a grid cell, which is not covered by any vegetation for at least 50 yr) and a parametrization for the Arabian Peninsula/Sahara desert region in order to consider extremes of water holding field capacities and albedo of bare soils identified in Fig. 2.1.4 (yellow crosses). Furthermore we subdivide globally distributed C3 grasses into "warm" (>0°C mean annual temperature, MAT) and "cold" C3 grasses (<0°C MAT) to account for a more realistic climate sensitivity. The PFT "cold shrubs" does not exceed cover fractions of 50% and therefore it is ignored in the calculation. Since cold shrubs are always associated to grid cells dominated by cold C3 grasses, both classes are combined to one soil tile. The adjusted classification of physical soil characteristics is shown in Fig. 2.1.4. Calculated means of the data set are summarized in Table 2.2. In general, desert soil tiles are characterized by low water holding field capacities and high soil albedo. C4 perennial grasses also have relatively high soil albedo and maximum field capacities of water due to high rooting depth. Soil tiles associated to

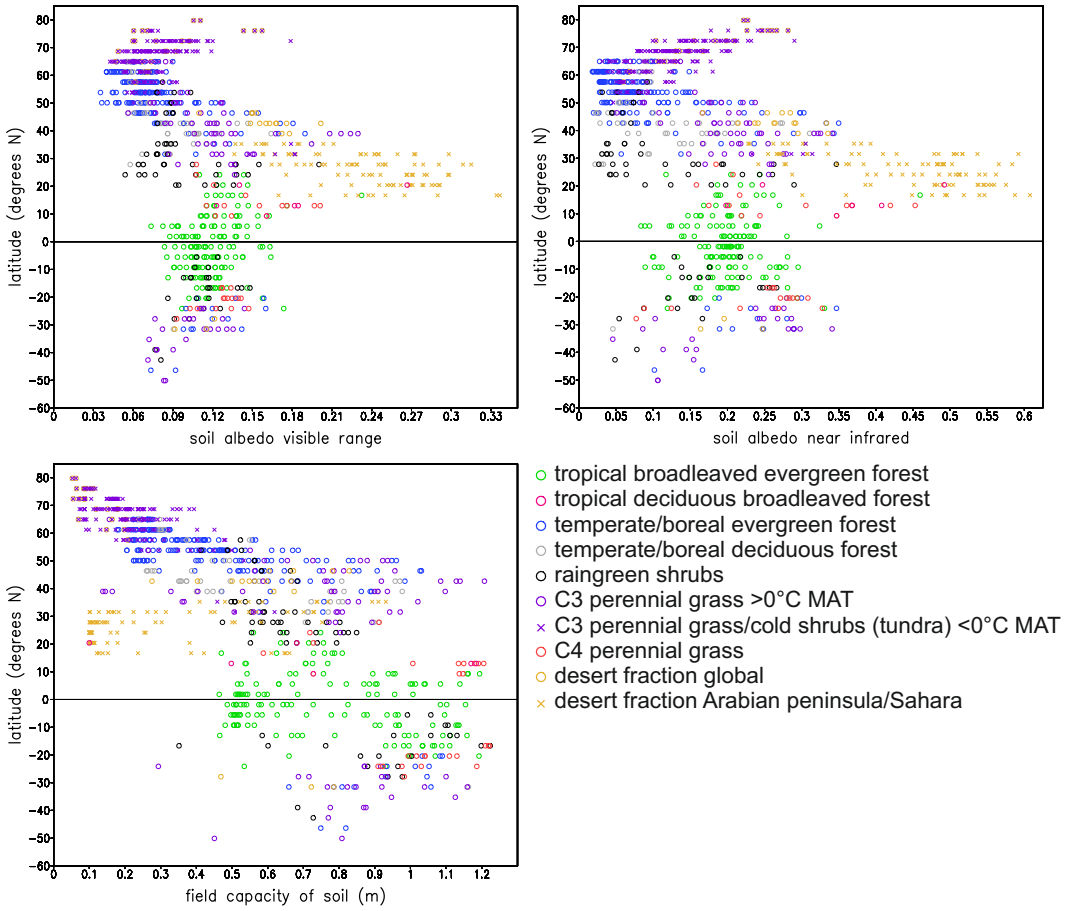

Figure 2.1.4: Standard physical soil properties (abscissa) associated with JSBACH plant functional types along latitudes. Albedo values have been derived from modified satellite measurements of the Moderate Resolution Imaging Spectroradiometer (MODIS) (Rechid et al., 2009), water holding field capacity of soils are optimized to plant rooting depths (Hagemann et al., 1999).

Table 2.2: Physical characteristics of soil tiles (original data retrieved from Hagemann et al., 1999 and Rechid et al., 2009, see Fig. 2.1.4).

Soil tiles based on calculated PFTs		h_{cws} (m) (total water holding field capacity of soil)	soil texture (FAO soil data flags)	α_{vis}, soil albedo VIS (0.3-0.7 µm)	α_{nir}, soil albedo NIR (0.7-3 µm)
tropical broadleaved evergreen forest		0.77	loam and clay	0.12	0.20
tropical deciduous broadleaved forest		0.73	loam	0.18	0.34
temper./boreal evergreen forest		0.50	loam	0.08	0.10
temper./boreal deciduous forest		0.58	loam	0.09	0.11
raingreen shrubs		0.68	loam	0.12	0.17
C3 perennial grass	C3 perennial grass > 0°C MAT	0.77	loam	0.12	0.21
	C3 perennial grass/cold shrubs (tundra) < 0°C MAT	0.23	loam	0.08	0.13
C4 perennial grass		1.07	loam	0.14	0.26
desert fraction	desert fraction global	0.17	loam	0.20	0.37
	desert fraction in Sahara, Arabian Peninsula >50% (13-35.26°N)	0.11	loam	0.25	0.49

tropical canopy have medium soil albedo and high total water holding field capacities. Soil tiles of temperate/boreal forest, typically located at mid and high northern latitudes have relatively low soil albedo (Fig. 2.1.4, Table 2.2), since at these locations land albedo increases with leaf area index (LAI) during summer months (Rechid et al., 2009). The FAO soil data flags according to Gildea and Moore (Henderson-Sellers et al., 1986) are a coarse classification of soil texture and are not discriminable due to our soil tiles. The calculated mean in soil texture is loam (3) for all soil tiles except for "tropical broadleaved evergreen forest", to which a finer mixture of loam and clay (4) is associated to. By calculation of means, extremes of physical soil properties vanish; therefore we conclude that the constructed lookup-table of physical soil tiles is rather a conservative estimate.

Soil dynamics

The soil scheme computes the actual soil tiles n consistent to the procedure described in Section 2.1.2. Then soil properties sol_n (h_{cws}, fao, $a_{s,vis}$, $a_{s,nir}$) referring to the lookup-table (Table 2.2) are calculated by a vegetation index. The vegetation index weights the cumulative cover fraction of soil tiles f_i per grid cell:

$$sol_n = \frac{\sum_{i=1}^{11} (f_i sol_i)}{\sum_{i=1}^{11} f_i} \tag{2.1.1}$$

Grid cells affected by the Arabian Peninsula/Sahara desert parametrization (Sect. 2.1.2) are not weighted by the procedure. The Arabian Peninsula/Sahara desert parametrization is defined by grid cells of at least 50% desert coverage between a latitudinal belt (13–35.26°N). We use a sill value of 50% desert fraction for a better representation of the Sahel (desert/savannah) transition zone where vegetation cover is generally overestimated by JSBACH (Vamborg et al., 2011).

Land surface processes

The following Sections describe physical model formulations in which soil characteristics (i.e. soil albedo, total water holding field capacity of soils, soil texture) are involved.

Land surface albedo. The basic land surface albedo scheme in ECHAM5 considers bare-soil albedo and albedo of snow that covers ground and forest canopy as a function of temperature (Roeckner et al., 2003). Changes of soil albedo with respect to soil wetness can impact climate (Levis et al., 2004), are included in some models (Wang, 2005) but are not considered in ECHAM5/JSBACH. The fractional snow cover at the ground depends on snow depth (in mm water equivalent) and slope of the terrain. The fractional snow cover of the canopy is defined by snow depth at the canopy and interception capacity (Roeckner et al., 2003). JSBACH expands this scheme by calculation of cover fraction of tiles n and leaf area index LAI_n. For tiles of grass and shrubs, snow cover on the ground $f_{sn,s}$ is also assumed to shade leaves. Albedo in the visible and near infrared range is calculated likewise and therefore is not discriminated:

$$\alpha_n = \left(f_s\,(1-f_s)\,e^{-LAI_n/2}\right)(1-f_{sn,s})\,\alpha_s + (1-f_s)\left(1-e^{-LAI_n/2}\right)(1-f_{sn,s})\,\alpha_l + f_{sn,s}\alpha_{sn} \tag{2.1.2}$$

The shading effect of forest is split into snow cover on canopy $f_{sn,c}$ and bare soil $f_{sn,s}$. Furthermore, a stem area of 1 is introduced to all forest PFTs, which is of particular interest in order to consider the seasonal change of deciduous forest.

$$\begin{aligned}\alpha_n &= \left(f_s\left(1-f_s\right)e^{(-LAI_n+stem)/2}\right)\left(\left(1-f_{sn,s}\right)\alpha_s+f_{sn,s}\alpha_{sn}\right)\\ &+\left(1-f_s\right)\left(e^{-LAI_n/2}-e^{(-LAI_n+stem)/2}\right)\left(\left(1-f_{sn,c}\right)\alpha_s+f_{sn,c}\alpha_{sn,c}\right)\\ &+\left(1-f_s\right)\left(1-e^{-LAI_n/2}\right)\left(\left(1-f_{sn,c}\right)\alpha_l+f_{sn,c}\alpha_{sn,c}\right)\end{aligned} \tag{2.1.3}$$

The soil albedo a_s in Eq. 2.1.2 and Eq. 2.1.3 is asynchronously updated (timestep 200 yr) regarding the cover fraction of soil tiles in Eq. 2.1.1.

Soil water. The iterative calculation of total water holding field capacity of soils h_{cws} potentially affects surface runoff, drainage and infiltration of water in the ECHAM5 bucket model and the uptake of plant available water in JSBACH (Roeckner et al., 2003). Also, the carbon assimilation pathway of plants is directly coupled to transpiration via stomata and therefore, it is dependent on the plant availability of soil-water content. At first, non-stressed CO_2 canopy conductance is determined by the photosynthetic demand (Knorr, 2000). If transpiration is higher than the actual soil-water content, the stressed canopy conductance of carbon through the stomata is scaled by a water stress factor f_{ws}. This factor is calculated from the relationship of actual soil-water h_{ws} provided by the hydrological model, the soil-water at the permanent wilting point h_{pwp} (default $h_{pwp} = 0.35$), and the maximum soil-water capacity h_{cws}:

$$f_{ws} = \frac{h_{ws} - h_{pwp}}{h_{cws} - h_{pwp}} \tag{2.1.4}$$

Quantities that change the soil-water content h_{ws}[1] are rainfall R (the part not intercepted by canopy), bare-soil evaporation, evapotranspiration and dew deposition (summarized as E), snow melt on ground and canopy (M_{sn}), surface runoff (R_s), and drainage (D). The modulation of h_{cws} can alter surface runoff and drainage. If the whole grid-cell becomes saturated, surface runoff R_s will be calculated by the traditional bucket model:

$$R_s = Q - (h_{cws} - h_{ws}) \tag{2.1.5}$$

where the total water input (Q) sums up to

$$Q = R + E + M_{sn} \tag{2.1.6}$$

If the soil is partly undersaturated, there will be still surface runoff due to the contribution of sub-grid scale areas which are saturated. Therefore, Eq. 2.1.5 is extended by

$$R_s = Q - (h_{cws} - h_{ws}) + \left(\left(1 - \frac{h_{ws}}{h_{cws}}\right)^{1/(1+b(\sigma))} - \frac{Q}{(1+b(\sigma))\,h_{cws}}\right)^{1+b(\sigma)} \tag{2.1.7}$$

[1] In order to account for the heterogeneous field capacities on a sub-grid scale, h_{ws} is defined by a probability density function $F(h_{ws})$ (Dümenil and Todini, 1992; Roeckner et al., 2003).

where the last term stands for the heterogeneous storage capacity controlled by the shape factor b, which is a function using a sub-grid scale parametrization of the standard deviation of height (σ) within the grid-cell. Infiltration (I) is simply defined by

$$I = Q - R_s \tag{2.1.8}$$

Infiltration into frozen soil is not allowed ($R_s = Q$). Three classes of drainage D are discriminated depending on the value of h_{cws},

$$D = \begin{cases} 0 & if\ \{h_{ws} \leq 0.05 h_{cws}\} \\ d_{min}\left(\frac{h_{ws}}{h_{cws}}\right) & if\ \{0.05 h_{cws} \leq h_{ws} \leq 0.90 h_{cws}\} \\ d_{min}\left(\frac{h_{ws}}{h_{cws}}\right) + (d_{max} - d_{min})\left(\frac{h_{ws} - 0.09 h_{cws}}{h_{cws} - 0.09 h_{cws}}\right)^{3/2} & if\ \{h_{ws} > 0.90 h_{cws}\} \end{cases} \tag{2.1.9}$$

with $d_{min} = 2.8 * 10^{-7} kg\, m^{-2}\, s^{-1}$ and $d_{max} = 2.8 * 10^{-5} kg\, m^{-2}\, s^{-1}$. No drainage occurs for soil-water content below 5% of the maximum field capacity. Drainage is assumed to follow soil-water content according to a linear relationship within 5% and 90% of h_{cws} ("slow drainage"), and exponential increase when h_{ws} exceed 90% of the maximum field capacity ("fast drainage").

Soil temperature. The model soil temperature from the surface to the bottom (10 m) is discretised by five unevenly spaced layers (thickness of the layer z) in order to calculate temperature propagation. Thermal conduction, soil density ρ_s , soil specific heat c_s and thermal diffusivity $\boldsymbol{\kappa}_s$ of snow-free soils are defined for ice sheets, glaciers and soils based on the FAO soil map. The material properties describe the thermal conductivity

$$\lambda_s = \rho_s c_s \kappa_s \tag{2.1.10}$$

which appears in the thermal diffusion equation

$$\rho_s c_s \frac{\delta T}{\delta t} = -\frac{\delta}{\delta z}\left(-\lambda_s \frac{\delta T}{\delta z}\right) \tag{2.1.11}$$

Equation 2.1.11 describes the temperature propagation δT through a soil layer of distinct thickness δz within a timestep δt. If snow is present on the soil, a mass-weighted function of the first soil layer and snow is used to derive material properties (Roeckner et al., 2003).

Experimental design

In this study three reference runs are taken: A Pre-industrial PI_ctl (Wei et al., 2012), a relatively warm mid-Holocene climate state (HOL, 6 kyr BP) HOL_ctl (Wei et al., 2012), and a model run representing the Last Glacial Maximum (LGM ca. 19 kyr BP) colder than present-day LGM_ctl (Zhang et al., 2012). All simulations have been performed using the conventional COSMOS-ASO configuration (atmosphere-ocean coupled model with dynamic vegetation) and the setup procedure of the Paleoclimate Modeling Intercomparison Project PMIP2 (Braconnot et al., 2012). They are run into an equilibrium climate state. The setup of HOL_ctl uses a different orbital parameter configuration and methane concentration in

the atmosphere of 650 instead of 760 parts per billion compared to Pre-industrial (Wei et al., 2012). Adjustments of boundary conditions for LGM include orbital parameters, sea-level drop, ice-sheet extent, elevation and an initial salinity increase of the glacial ocean by 1. A deviation from the PMIP2 protocol is a tuning of land-sea mask and ocean gateways, and LGM_ctl is initialized from a glacial ocean which enables a more realistic glacial ocean circulation (Zhang et al., 2012). The length of simulation PI_ctl and HOL_ctl is 3000 yr, whereas LGM_ctl is integrated for 5400 yr in total. The last timestep of each reference run is used for initialization of the soil experiments and run for another 600 yr in total (see Sect. 2.1.2). The impact of the soil scheme on climate (HOL, LGM) is examined using a factor separation technique that has been devised by Stein and Alpert (1993) for identifying synergies in numerical models. The effect of soil and climate (HOL_sol-PI_sol and LGM_sol-PI_ctl, respectively) are being disentangled by subtracting the single contribution of climate. Here, the effect of soil under warmer/colder climate is indicated by $\hat{f}_{i,sol}$:

$$\hat{f}_{i,sol} = (sol_i - PI\_sol) - (ctl_i - PI\_ctl) \quad (2.1.12)$$

$$soil\ feedback = (climate + soil) - climate \quad (2.1.13)$$

where the index i represents the respective climate state (LGM, HOL). This procedure cancels out the error of routine (PI_sol-PI_ctl), which arises by inducting the soil scheme into COSMOS-ASO. We have to assume that the magnitude of error of routine, calculated for Pre-industrial, is the same as in our paleo simulations.

2.2 NAOSIM

The North Atlantic/Arctic Ocean Sea-Ice Model (NAOSIM) has been developed at the Alfred Wegener Institute (Kauker et al., 2003; Köberle and Gerdes, 2003). The spatial domain of the ocean/sea-ice model captures the Arctic Ocean, the Nordic Seas and the northern North Atlantic (90°N–50°N). The model has a horizontal resolution of 0.25 × 0.25° per grid box (ca. 27 × 27 km^2, respectively) and 30 unevenly spaced levels in the vertical. A dynamic-thermodynamic sea-ice model with a viscous plastic rheology (Hibler, 1979) is coupled to the ocean model (Kauker et al., 2003).

2.2.1 Experimental design

Atmospheric forcing

The present model studies are forced by differing atmospheric boundary conditions including the parameters 2 m air temperature above surface, dew point temperature, total cloud cover, precipitation, zonal and meridional component of wind speed, and surface wind stress. The modern control run (CTRL) is forced by atmospheric data fields provided by the NCEP/NCAR reanalysis project (Kalnay et al., 1996), whereas glacial atmospheric data was generated by simulations of an atmospheric general circulation model (Lohmann and Lorenz, 2000; Romanova et al., 2004).

The atmospheric boundary forcing of model study LGMC is derived from a dataset of the global atmospheric model ECHAM3/T42L19, which was adapted to the glacial boundary

conditions by Lohmann and Lorenz (2000). In one sensitivity study that used sea surface temperature, ice cover as well as albedo reconstruction as per CLIMAP (1981), Lohmann and Lorenz (2000) decreased CLIMAP SSTs in the tropics (30°S–30°N) by 3°C. Compared to the standard atmospheric LGM run, the sensitivity study with artificial cooling in the tropics is in better agreement with marine and terrestrial proxy data (Lohmann and Lorenz, 2000) and is used as present atmospheric boundary forcing for LGMC.

For another model study (LGMG), the atmospheric data fields are provided by the same atmosphere model, ECHAM3/T42L19 with glacial setup but based on GLAMAP (Romanova et al., 2004). LGMG atmospheric boundary conditions are forced by glacial SST, albedo, and sea-ice reconstruction of the Atlantic region provided by GLAMAP 2000 (Glacial Atlantic Ocean Mapping; Paul and Schäfer-Neth, 2003). In contrast to CLIMAP (1981), reconstructions of GLAMAP 2000 exhibit year-round warmer SSTs in the North Atlantic and summer ice free conditions in the central and eastern part of the Nordic Seas with winter expansion south of Iceland and Faeroe (Pflaumann et al., 2003). The atmospheric data fields force NAOSIM twice per day and are repeated over a 15-yr cycle.

Glacial Arctic freshwater budget

So far, knowledge of the glacial Arctic freshwater budget is sparse. In general, the glacial circum-Arctic ice-sheets hindered the northward transport of latent heat (Stein, 2008). This resulted in an isolated Arctic domain characterized by decreased temperatures and humidity and in consequence with reduced meteoric precipitation and a weakened hydrological cycle (Lohmann and Lorenz, 2000). The Pacific westerlies are split into a shifted branch southward to the flank of the Laurentide ice sheet at 40–50°N latitude (Clark et al., 1999; Lambeck et al., 2002) and a northward excursion across the Canadian Arctic as indicated by modeling results (e.g. Lohmann and Lorenz, 2000). The Siberian sector is influenced by cold, dry winds on the lee side of the Fenno-Scandinavian ice sheet (Hubberten et al., 2004; Siegert and Marsiat, 2001; Siegert and Dowdeswell, 2004) as well as an anticyclonic regime over Siberia that hinders the advection of Atlantic air masses (Arkhipov et al., 1986; Velichko et al., 1997). Furthermore, the Bering Land Bridge connecting Asia and North America is blocking the Pacific inflow of freshwater for the Arctic Ocean. As a consequence the total freshwater budget for the Arctic Ocean is decreased (Martinson and Pitman, 2007). The presumed glacial Arctic river inflow roughly corresponds to half (1800 $km^3\,yr^{-1}$) of today's annual budget of 3300 $km^3\,yr^{-1}$ (Aagaard and Carmack, 1989), which ranges between glacial runoff in the AGCM (1082 $km^3\,yr^{-1}$) and a modeling study using a more realistic river routing (ca. 2000 $km^3\,yr^{-1}$; Alkama et al. 2008). The model takes into account changes in salinity by water transport, precipitation, snowmelt, sea-ice melting, freezing, and river runoff. Apart from the salinity advection term in the ocean, salinity fluxes in the model are not associated with momentum and volume. An additional salinity restoring term at the sea surface using the present climatology of salinity fields (Levitus et al., 1994; Levitus and Boyer, 1994; National Snow and Ice Data Center, 1997), prevents the model climate from broadly drifting in the Arctic Ocean and is necessary to obtain a halocline (Steele et al., 2001). The restoring term has a long time scale of 180 days and the additional freshwater flux adds ca. 17 $mm\,yr^{-1}$ to the Arctic Ocean. The salinity restoring term is applied to all model studies presented here. In one sensitivity study (LGMC_sal), we applied glacial sea surface salinity from a climate model output (Shin et al., 2003b,a) in order to discuss the impact on the results.

Model setup

The control run (CTRL) uses the ocean/sea-ice model used by Kauker et al. (2003) and Köberle and Gerdes (2003). The atmospheric forcing data consists of the NCEP/NCAR reanalysis project (Kalnay et al., 1996) for the period 1948–2007. The last 30 yr (1977–2007) of CTRL are used for comparison with the glacial sensitivity studies. For the change in morphology of the glacial ocean, the present-day land-sea mask (NOAA, 1988) is adapted to the ice sheets in the Northern Hemisphere (Ehlers and Gibbard, 2007) and sea level is lowered by 120 m (Fairbanks, 1989). In order to depict thermodynamic processes on a sub-grid scale, like open water areas between sea-ice, seven ice classes are defined following a Gaussian distribution around the mean sea-ice thickness. Model studies without limitations show sea-ice thickness >80 m after 120 modeled years along the northern Barents Sea shelf edge, north of Greenland and Baffin Bay without reaching an equilibrated sea-ice thickness. In the glacial model runs, the potential mean sea-ice thickness of each grid cell is limited to a maximum of 30 m in order to reach equilibrium. The upper limit of mean sea-ice thickness in the sea-ice model was motivated by the maximum height of pressure ridges observed by present-day observations of first-year ice as reported by Polyak et al. (2010). As a consequence of the glacial water storage over land, an additional increase in salinity of 1 psu (practical salinity unit) is prescribed for the open boundary condition of the northern North Atlantic inflow. In order to account for a temperature decrease, the lateral temperature at the southern boundary is reduced by 2°C, consistent with global ocean simulations (e.g. Butzin et al., 2005). Experiments testing the prescribed southern boundary characteristics (barotropic stream function) with a glacial model setup have only minor effects on the through flow of the Arctic Ocean (cf. Fig. 5.3.9). The ocean model is initialized by an LGM simulation of a general circulation model (NCAR-CCSM; Shin et al., 2003b,a) and the initial conditions of the sea-ice model (zonal and meridional component of sea-ice drift velocities, snow-cover thickness, sea-ice thickness) are set to zero to avoid any preconditioning. The total water mass of the upper Arctic Ocean layer (0-1000 m) of the NAOSIM present-day setup is typically exchanged within 30 yr (Karcher and Oberhuber, 2002) in agreement with observations on tracer contaminants (Macdonald and Bewers, 1996; MacDonald et al., 2004). The lengths of the model runs are 120 model years, only the last 30 yr are used for analysis. Major contribution of present water mass exchange happens through western Fram Strait, where salty and warm Atlantic waters enter the Arctic Ocean in the upper ca. 200 m (Fig. 5.3.8, p. 76). All of our glacial model simulations exhibit a displaced inflow of bottom waters >2 $\mathrm{m\,s^{-1}}$ stronger than the Atlantic Water Current in CTRL, which equals an increase of surface outflow of the Arctic Ocean because of mass conservation (Fig. 5.3.8b-f, p. 76 and Fig. 5.3.9, p. 75). Changes in the barotropic stream function (±50% psi compared to LGMC) at the southern boundary of the prescribed northern North Atlantic inflow as already shown for present-day conditions (Kauker et al., 2005) do not significantly impact rates of water exchange at Fram Strait (Fig. 5.3.9, p. 75). In response experiments with present-day setup Kauker et al. (2005) state that barotropic anomalies at 50°N latitude do not pass the Greenland-Scotland Ridge, but an increase of 2°C for the upper 500 m of the southern boundary water column effectively warms the West Spitsbergen Current by ca. 0.5°C (as shown in 300 m depth) within two years. In order to analyze the importance of glacial wind fields with respect to the respective SST reconstruction and the presence of glacial ice sheets, we performed another sensitivity study. The sensitivity study (LGMC_PDw, LGMG_PDw) uses the glacial setup (LGMC, LGMG) and is run with present-day wind fields (Lohmann and Lorenz, 2000).

Chapter 3

Control of orbital parameters, CO_2 and boundary conditions on climate sensitivity

3.1 Milankovitch's theory

The theoretical foundation of the astronomical theory of glacial cycles was developed by Milankovitch (1941), who fundamentally broadened the former theory of Croll (1875) by conflating Earth's orbital parameters eccentricity (elliptical shape of Earth's orbit) and obliquity (tilt of Earth's rotational axis) with precession (length of perihelion) into the calculation of latitudinal and seasonal solar insolation (Fig. 3.2.1). In his linear model, low boreal summer insolation is critical to maintain snowfields throughout the year to build up ice-sheets. Since then the theory was enriched by additional conceptual models (e.g. greenhouse gases, internal ice dynamics) that try to explain discrepancies between the climate history as suggested by the theory, and proxy data ($\delta^{18}O$ stack) by nonlinear effects in Earth's climate system (Paillard, 2001; Ruddiman, 2006a,b and references therein). However, the amplitude of glacial/interglacial cycles in $\delta^{18}O$ records is remarkably diminished prior to Northern Hemisphere glaciation ca. 2.7 myr ago (Lisiecki and Raymo, 2005). Here, we use a GCM to test a suite of orbital parameter configurations at their extremes in order to narrow down orbital impact (Sloan and Morrill, 1998) on different climate states. The climate states are characterized by an ice-free Greenland (Tortonian climate state, 11–7 myr ago) prior, and a Greenland Ice-Sheet after (pre-industrial climate state) the Northern Hemisphere glaciation during the late Pliocene. Additionally, we perform model studies of different atmospheric CO_2 values for the Tortonian. We elaborate the effect orbital parameter settings in context of different atmospheric CO_2 values.

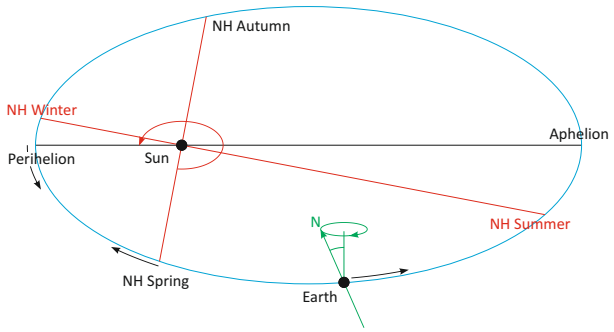

Figure 3.2.1: Earth's orbital parameters: Obliquity (tilt of the Earth's rotational axis, green), precession (length of perihelion, red) and eccentricity (shape of the Earth's orbit, blue).

3.2 Principles of orbital parameters

The dominant driver's of insolation variations are obliquity and precession (Fig. 3.2.1). The tilt of the Earth's axis of rotation (obliquity) controls the latitudinal distribution of top of the atmosphere incoming solar radiation. It gives a rise to a displacement of the ice-sheet equilibrium line, which divides the ice sheet into net-accumulation and -ablation regions. For instance, a relative decrease of high latitude insolation by bated obliquity cools polar regions and hence results in ice-sheet growth by shifting the equilibrium line equatorwards.

The precession parameter, given in degrees, describes the length of perihelion of the Earth's ellipsoidal orbit from the vernal equinox. It expresses the amplitude of the seasonal cycle. According to Milankovitch (1941), maximum precession (i.e. winter solstice in perihelion) results in cold summers (and mild winters), which favors ice-sheet growth. Although the insolation effect of the eccentricity of the Earth's orbit (Fig. 3.2.1) and its climatic effect is small, it strongly modulates the precession signal, dampening or reinforcing its climatic effect.

3.3 Results

The Section begins with the description of the monocausal influence of orbital parameters under pre-industrial conditions with respect to "cold orbit" conditions (Sect. 3.3.1), followed by a summary of results from experiments with identical orbital parameter configuration, for Tortonian climate at pre-industrial (278 ppmv) and increased (450 ppmv) atmospheric CO_2 concentrations (Sect. 3.3.2) (Pagani et al., 2005; Hönisch et al., 2009; Tripati et al., 2009; van de Wal et al., 2011). Subsequently, the integrated results of obliquity and precession forcing are shown with a focus on their synergy (Sect. 3.3.3). Finally, the seasonal cycle of Arctic sea surface temperature (SST) and sea-ice is examined and complemented by an analysis of the evolution of a perennial Arctic sea-ice cover under transient CO_2 forcing.

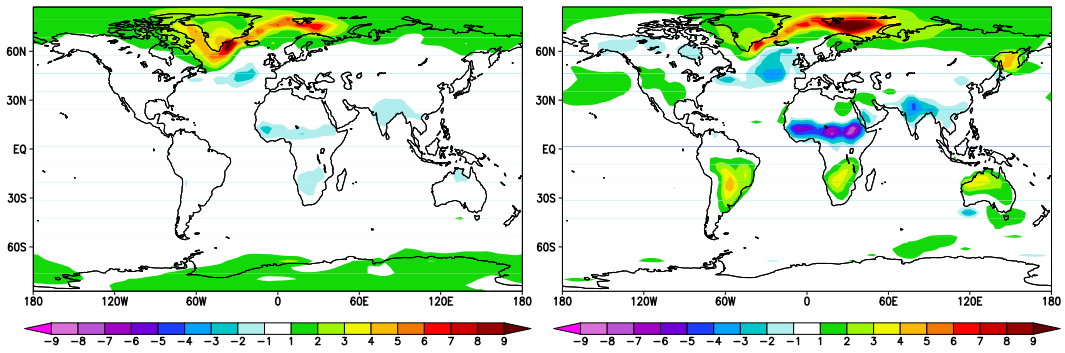

Figure 3.3.1: Surface air temperature anomaly (°C) of high obliquity ((PI_wO_cP_278)-(PI_cO_cP_278), left), and strong precession ((PI_cO_wP_278)-(PI_cO_cP_278), right) with respect to a "cold orbit" pre-industrial setting (PI_cO_cP_278).

3.3.1 Obliquity and precession forcing at pre-industrial conditions

In general, obliquity forcing does not cause a strong global average signal in surface air temperature (SAT; -0,03°C), although warming in the polar regions is amplified by sea-ice retreat especially around Greenland/Barents Sea via associated sea-ice albedo feedbacks (Fig. 3.3.1). Interestingly the precession forcing creates similar, but stronger, SAT signal in the North Polar Region alike obliquity (Fig. 3.3.1). Pronounced seasonality beyond the Polar Region favors summer warming and ice melting within the polar circle, whereas the absence of insolation during the polar night disables negative orbital forcing. This nonlinearity in precession forcing causes global mean temperature anomalies of +0.24°C (Table 3.1). In both cases, high latitude warming slows down the northward heat transport of the Atlantic Meridional Overturning Circulation (AMOC), causing local cooling in the northern North Atlantic as a consequence. In low latitudes the obliquity forcing indirectly amplifies the seasonal amplitude: A strong tilt of the Earth's rotational axis shifts the equator relative to the celestial equator and thus the inclination angle of insolation, mimicking a pseudo-precession signal in the seasonal cycle. Since the obliquity forcing is in phase at both Hemispheres, an intensified seasonal cycle results in stronger boreal summer and winter monsoons at low latitudes, which causes elevated inland moisture transport and reflects latent cooling over the continents (Fig. 3.3.1). A similar, but higher magnitude temperature pattern is shown in the intensification of North African and Indian/Chinese Monsoon caused by precession forcing, whereas decreased continental precipitation by boreal winter monsoon causes latent warming in the Southern Hemisphere.

Table 3.1: Global mean surface air temperature anomalies (°C).

orbit	PI (278 ppmv)	TO (278 ppmv)	TO (450 ppmv)
cO_cP	14.4	15.8	19.3
wO_cL-cO_cP	-0.03	0.27	0.04
cO_wP-cO_cP	0.24	0.46	0.48
wO_wP-cO_cP	0.36	0.58	0.57
synergy	0.15	-0.14	0.05

3.3.2 Obliquity and precession forcing at Tortonian conditions and differential CO_2 levels

Similar to pre-industrial conditions, high obliquity forcing for the Tortonian causes bipolar warming (Fig. 3.3.2) and intensified monsoons in both hemispheres, independent of CO_2. However, the Arctic warming anomaly at 450 ppmv CO_2 is muted compared to 278 ppmv, mainly due to the absence of seasonal sea-ice around Greenland and the Barents Sea. SAT at Antarctica is not sensitive to orbital forcing. Precession forcing for the Tortonian (278 ppmv CO_2) causes a similar warming in the Arctic region like obliquity, which also extends to North Siberia. In combination with less effective latent cooling at the Sahel zone and Southwest Asia, this sums up to a global warming anomaly of +0.46°C. Precession forcing under warm Tortonian conditions (450 ppmv CO_2) shows a warming of similar magnitude (+0.48°C), although sensitivity of precession forcing in the Arctic region is strongly attenuated (Fig. 3.3.2d) compared to Tortonian conditions at pre-industrial CO_2 levels (Fig. 3.3.2c).

3.3.3 Impact and synergy of the combined orbital forcing on pre-industrial and Tortonian conditions at differential CO_2 levels

The combined signal of obliquity and precession forcing applied to pre-industrial conditions displays highest warming (>+9°C) at the sea-ice edge around Greenland and in the Barents Sea (Fig. 3.3.3). The warming of the Arctic Ocean is >+3°C and extends towards North Siberia and Norway. Obliquity forcing causes a moderate warming in Antarctica. The precession forcing dominates the strong latent cooling at Sahel and South Asia and the relative warming, caused by decreased continental precipitation, at the horse latitudes (30°N, S), similar to the monocausal influence of precession forcing (Fig. 3.3.1). Parallel to Fig. 3.3.1, cooling in the northern North Atlantic Ocean is associated to reduced northward heat advection by the AMOC. Under Tortonian boundary conditions with moderate CO_2 (278 ppmv), the two orbital forcing factors show a similar SAT anomaly pattern as seen in the pre-industrial model study. However, continental warming extends further equatorwards, impacting Europe and the Sahara region. Monsoonal cooling is not as strong as shown in the pre-industrial model study. At high levels of CO_2, the Tortonian model climate shows differences at the location of the sea-ice margin compared to low CO_2 levels. Around the coast of Greenland and Barents Sea, SAT anomalies are weaker than in the pre-industrial and Tortonian (278 ppmv CO_2) model studies. Instead, in the Southern Hemisphere the transformation from Antarctic perennial to seasonal sea-ice (not shown) causes strong regional warming in the Ross Sea (Fig. 3.3.3).

The synergistic effect, with respect to the temperature signal in Fig. 3.3.3, can be

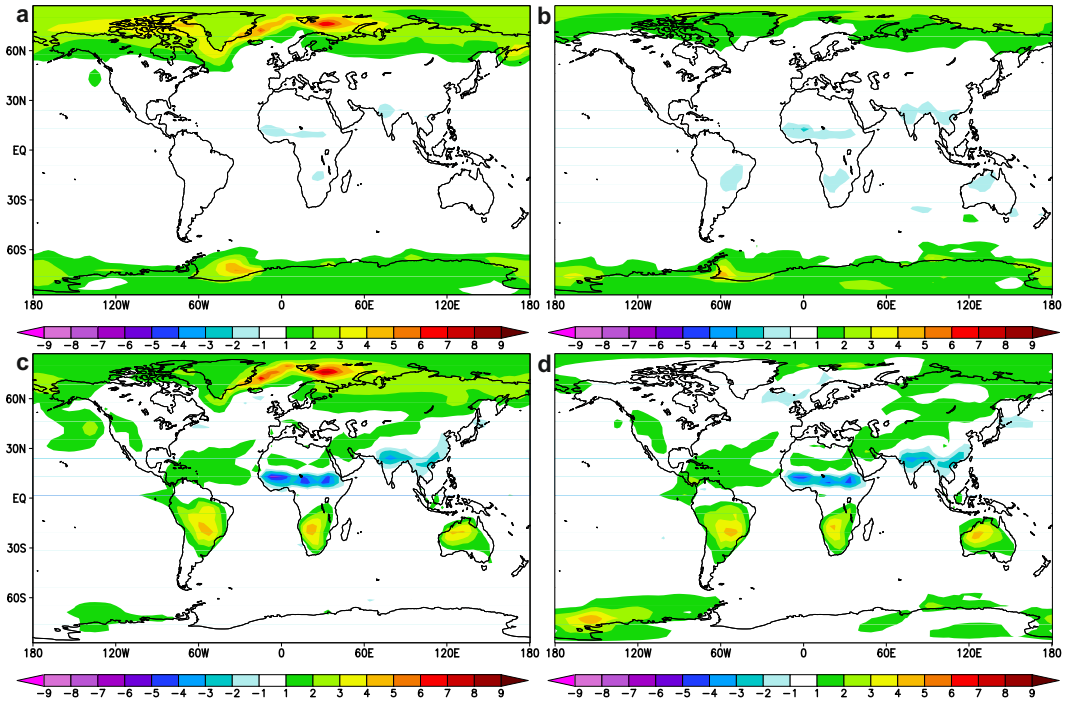

Figure 3.3.2: Tortonian surface air temperature anomaly (°C) of obliquity forcing at (a) low ((TO_wO_cP_278)-(TO_cO_cP_278)), (b) high ((TO_wO_cP_450)-(TO_cO_cP_450)) CO_2 levels, and precession forcing at (c) low ((TO_cO_wP_278)-(TO_cO_cP_278)), (d) high ((TO_cO_wP_450)-(TO_cO_cP_450)) CO_2 levels.

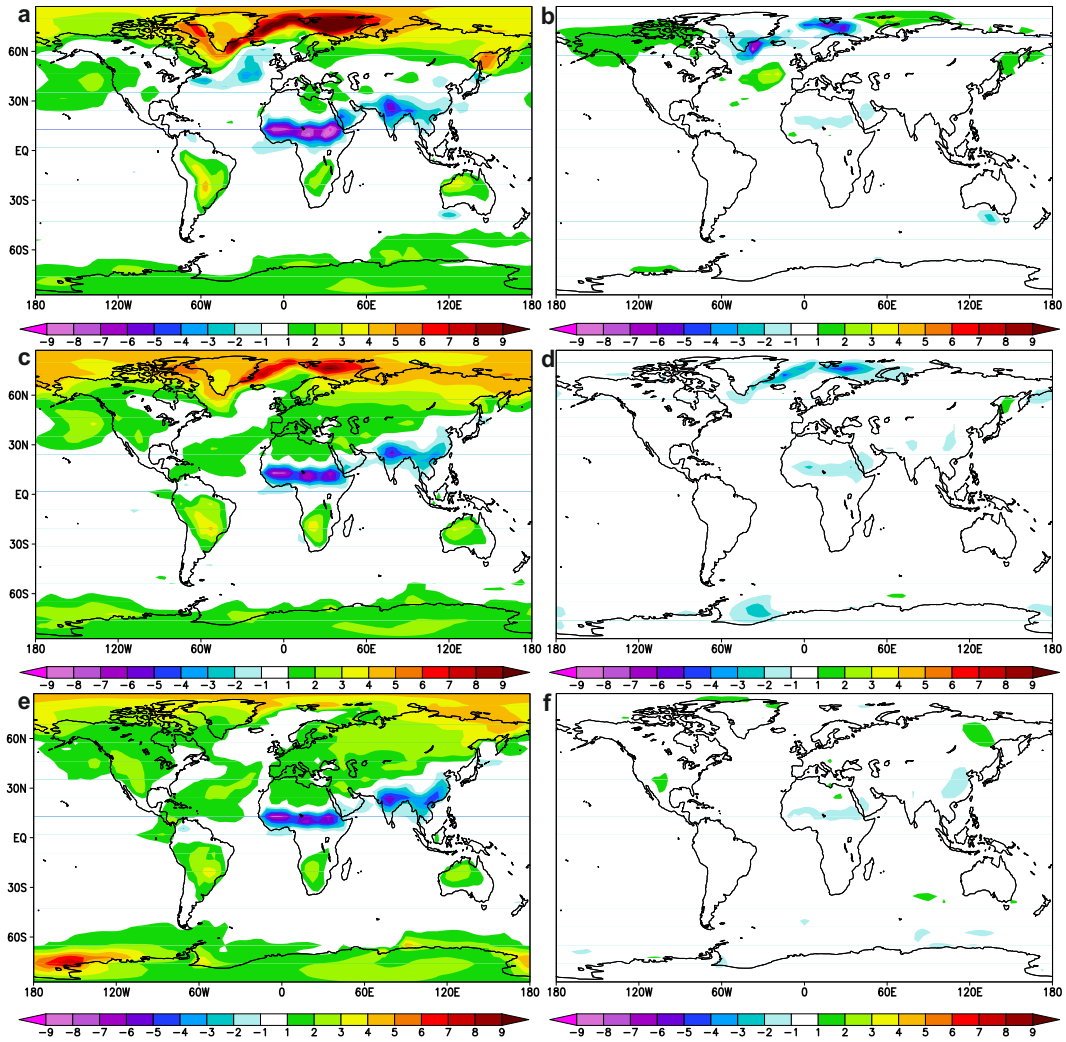

Figure 3.3.3: Surface air temperature anomaly (°C) of coupled precession and obliquity forcing for (a) Pre-industrial and (b) its synergy, (c) Tortonian and (d) its synergy and (e) Tortonian at high CO_2 levels (450 ppmv) and (f) its synergy.

interpreted as the surplus of warming caused by the combination of obliquity and precession forcing. If the monocausal impact of each, obliquity and precession, sums up to the equal of both combined factors, the synergy is zero. Positive synergy values denote a warmer, negative values indicate a colder temperature signal than derived from the linear combination of both forcings. Both pre-industrial and Tortonian simulations at 278 ppmv CO_2 (Fig. 3.3.3) show a strongly decreased synergistic effect at the Arctic sea-ice margin. This demonstrates a strong nonlinear effect of sea-ice in the climate system. However, other regions like the Northern North Atlantic in the pre-industrial model runs tend to warm due to the synergistic effect: The Atlantic Meridional Overturning Circulation (AMOC) is less reduced, and thus more heat is advected northwards than the linear combination of obliquity and precession forcing suggests. For Tortonian climate, the AMOC, a potential nonlinear subsystem of the climate, is strongly muted since pacific waters are imported through the open Central American Seaway, which effectively diminishes the strength of the AMOC (Knorr et al., 2011). All three climate states, Pre-industrial, Tortonian, and Tortonian at high CO_2 levels (450 ppmv) show all some reinforced synergistic cooling at the Sahel boundary (Fig. 3.3.3). The global synergistic effect is a some warming for Pre-industrial (+0.15°C) and a cooling for the cold Tortonian (278 ppmv CO_2, -0.14°C). There is no effect for the warm Tortonian (450 ppmv CO_2, +0.05°C) setup (Table 3.1).

3.3.4 Orbital impact on the seasonal cycle of Arctic sea-ice at different climate states

In order to gain a mechanistic understanding of the modeled sea-ice dynamics, we analyze the seasonal cycle of integrated sea-ice cover. Since the orbital parameter setting is optimized for the Northern Hemisphere, the focal point is on the analysis of Arctic sea-ice cover and SST (Fig. 3.3.4). In principle all diverging orbital studies (changes in obliquity and/or precession with respect to a cold orbit) settings (see Fig. 3.3.4 black line) show a warming trend in Arctic SST and a decline in sea-ice cover. For Pre-industrial, simulations with obliquity (green line) and precession (yellow line) forcing exhibit a similar effect on integrated Arctic sea-ice cover. The precession forced SST warming gradually diverge for warmer background climate states (Fig. 3.3.4d, f) compared to obliquity forced studies. For the Pre-industrial, the effects of obliquity and precession sum up to the combined effect of both factors (Fig. 3.3.4a), which proofes a linear relationship. Since Arctic Ocean water is covered almost the whole year by sea-ice, there is no strong impact on Arctic SST (Fig. 3.3.4b). The warmer Tortonian climate at pre-industrial CO_2 levels (+1.4°C compared to Pre-industrial, Table 3.1) is characterized by reduced sea-ice cover compared to Pre-industrial, but no appreciable warming of SST is observed (Fig. 3.3.4d). The Tortonian studies at 450 ppmv CO_2 level are characterized by summer ice-free conditions in the Arctic (except for the cold orbit). In these simulations summer SSTs are strongly increased while winter SST is still at freezing temperature. The surplus of insolation for the "warm orbit" configuration also prolongs summer ice-free conditions by ca. 2–3 months, additionally warming ocean waters. One cause is the extra amount of heat, stored in the Arctic Ocean, that delays sea-ice formation in autumn (Fig. 3.3.4e).

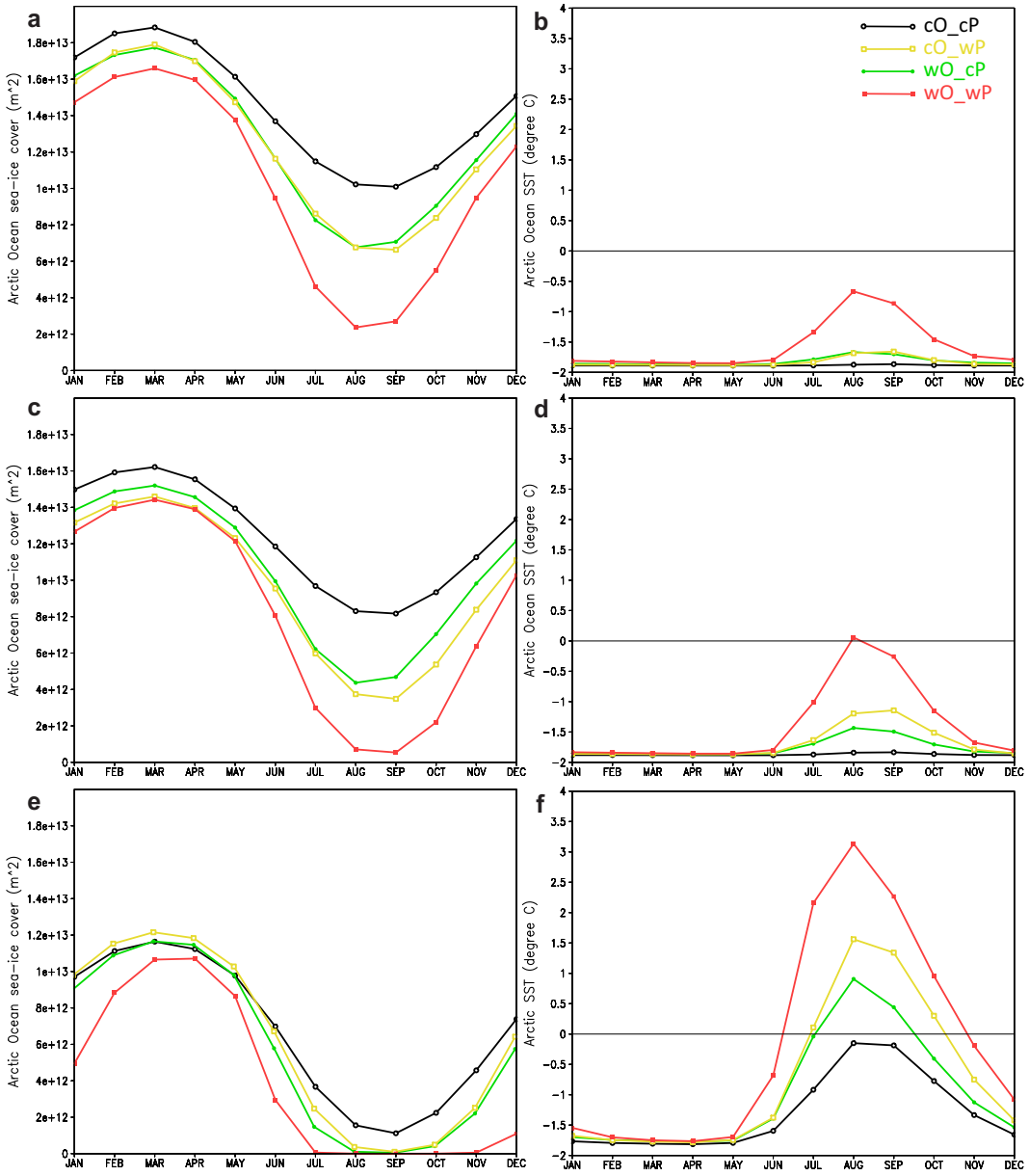

Figure 3.3.4: Seasonal cycle of sea-ice cover in the Northern Hemisphere (NH) on the left versus Arctic sea surface temperature (SST) on the right for orbital sensitivity studies at diverse climate states. Displayed integrated Arctic sea-ice cover (m^2) for (a) Pre-industrial, (c) Tortonian (278 ppmv CO_2), (e) Tortonian (450 ppmv CO_2) and Arctic SST (°C) for (b) Pre-industrial, (d) Tortonian (278 ppmv CO_2), and (f) Tortonian (450 ppmv CO_2).

3.3.5 Changes of the impact of obliquity by transient CO_2 forcing

In order to understand the high climate sensitivity of obliquity forcing at 278 ppmv CO_2 levels versus low sensitivity of obliquity forcing at 450 ppmv for a Tortonian setup (+0.27°C and +0.04°C global mean SAT, respectively; Table 3.1), we applied transient descending CO_2 forcing (450–278 ppmv). In the analysis, we focus on the evolution of the marine cryosphere in the Northern Hemisphere (Fig. 3.3.5). Fig. 3.3.5 shows the evolution of seasonal cycle of NH sea-ice cover with ice free ocean conditions during late summer from the beginning of the simulation with 450 ppmv CO_2 in the atmosphere to the end of the experiment with 278 ppmv CO_2.

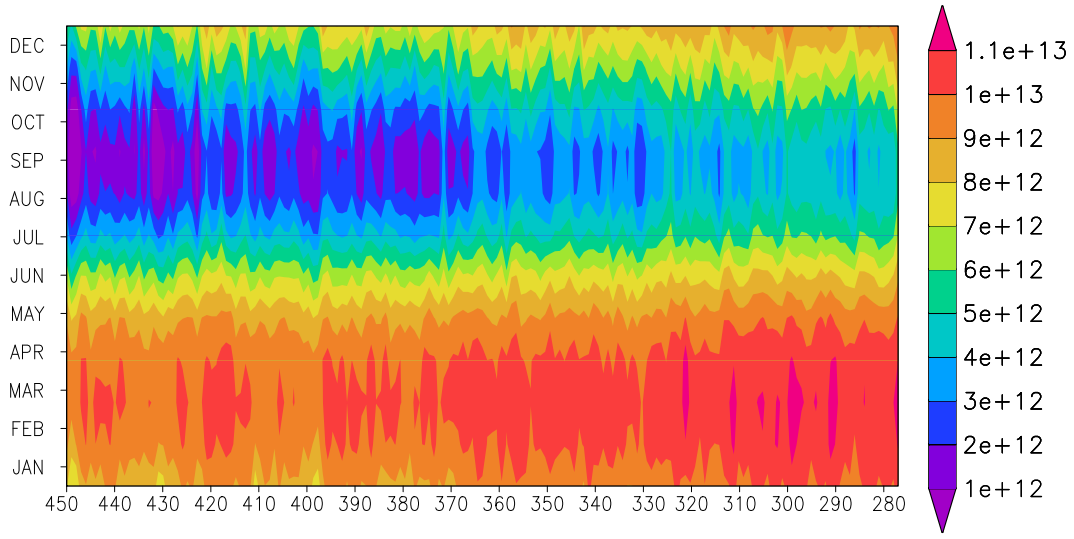

Figure 3.3.5: Evolution of the seasonal cycle, abscissa, of integrated Northern Hemisphere sea-ice cover (m^2) under transient CO_2 forcing (1 ppmv yr^{-1}), ordinate. "Cold orbit" obliquity-forcing (see TO_cO_cP_450–278, Table 2.1) is applied to the Tortonian model setup.

There is a threshold for the development of perennial ice of ca. 365–330 ppmv. At CO_2 values of about 330 ppmv a permanent ice cover establishes. Further CO_2 reduction continuously increases sea-ice cover during summer as well as winter. The cumulative volume of northern hemispheric sea-ice shows a similar evolution like sea-ice cover. The anomaly plot of "cold orbit" obliquity versus "warm orbit" settings (Fig. 3.3.6, lower panel) illustrates the impact of obliquity on sea-ice volume depending on CO_2 concentrations. At CO_2 values higher than 365 ppmv, obliquity forcing can shift the timing of ice-free conditions, and hence the volume, at the transition from polar night to polar day of about two months (June–July). The rapid transition towards permanent Arctic ice-cover is associated with an increase in sea-ice volume especially from June to August. In this critical CO_2 regime, the obliquity forcing dominates changes in sea-ice volume at the transition from polar night to polar day. Below 365 ppmv CO_2, anomalous sea-ice volume, which endures throughout the summer, also impacts the subsequent winter causing nonlinearities in the climate system. This increases the sensitivity of climate to obliquity forcing characterized by seasonal Arctic sea-ice cover

(see Fig. 3.3.2).

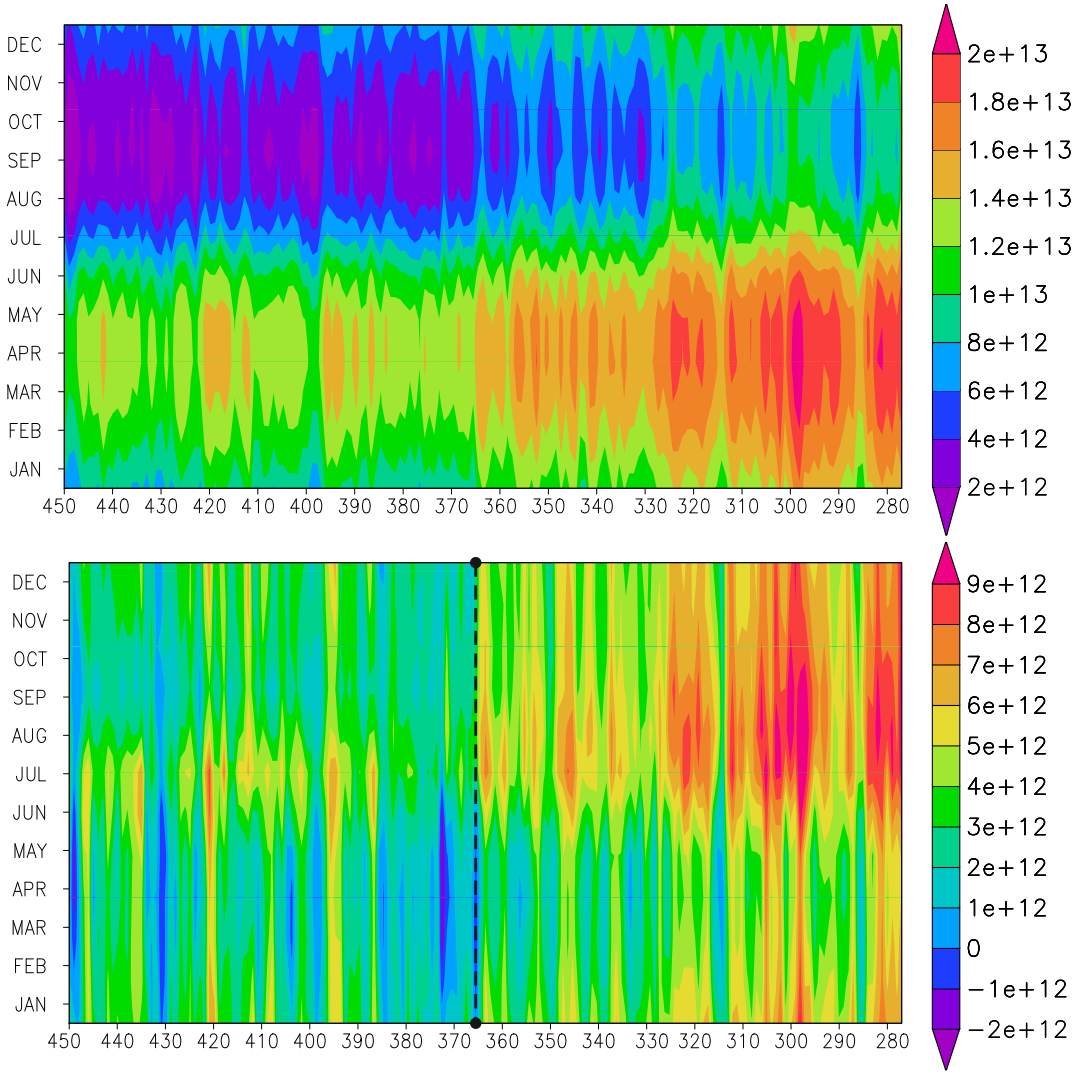

Figure 3.3.6: Evolution of the seasonal cycle, abscissa, of integrated Northern Hemisphere sea-ice thickness (m^3) under transient CO_2 forcing (1 ppmv yr^{-1}), ordinate. The upper panel displays results of the transient simulation with "cold orbit" parameters (see TO_cO_cP_450–278, Table 2.1) at Tortonian boundaries, the lower panel shows the anomaly of transient simulation with "cold orbit" parameters compared to high values of obliquity setting (TO_wO_cP_450–278). The dashed line indicates the threshold from seasonal to permanent Arctic sea-ice.

In order to analyze the nonlinear effect of obliquity on sea-ice in more detail, we compare the linear trends of both CO_2 ramp studies with modified obliquity parameters before and

after the establishment of the permanent sea-ice cover at 365 ppmv CO_2 (Fig. 3.3.7).

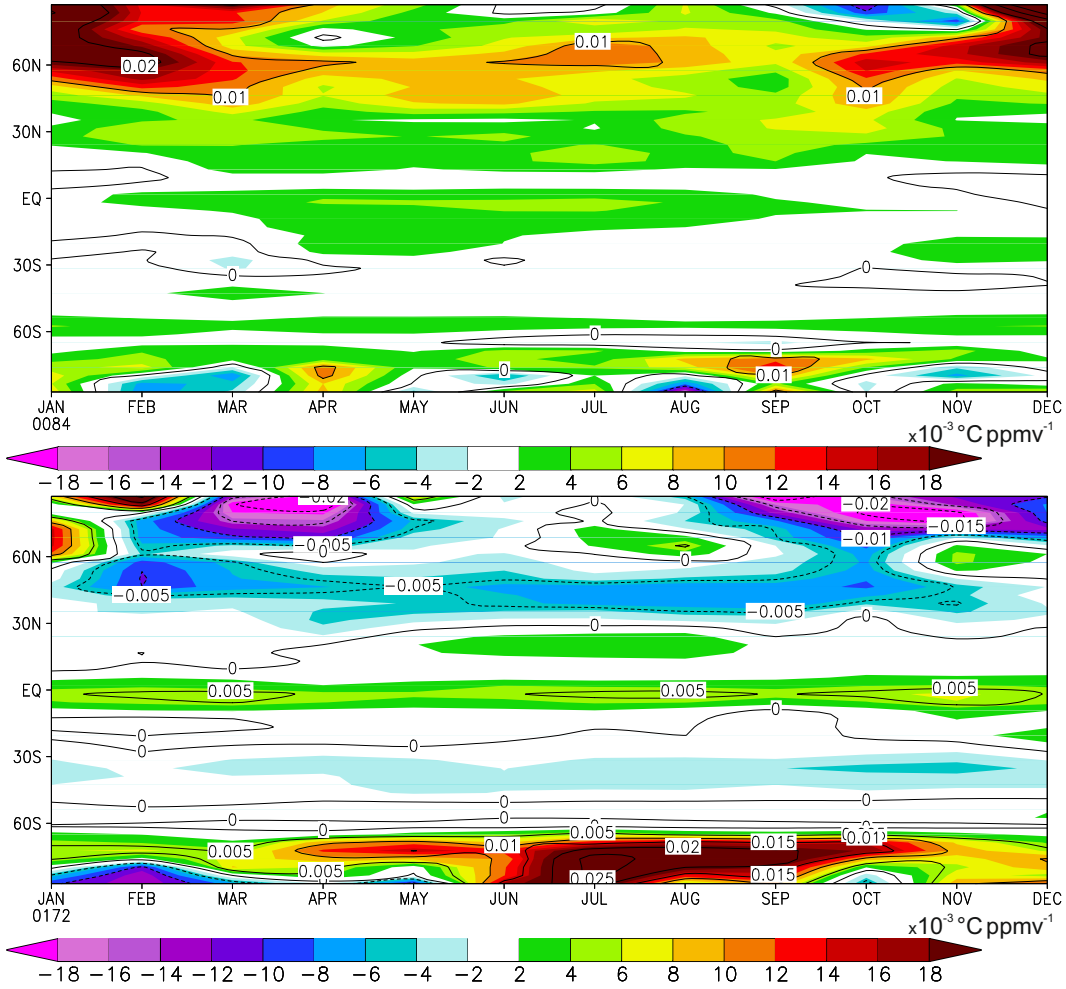

Figure 3.3.7: Both panels display the anomalous trend (linear regression) (°C ppmv^{-1}) of a "cold orbit" with respect to a "warm orbit" obliquity setting (TO_cO_cP_450–278)-(TO_wO_cP_450–278), once for the transient CO_2 forcing 450–365 ppmv (upper panel), and once for the CO_2 forcing interval 365–278 ppmv (lower panel). Positive values denote higher climate sensitivity for a "warm orbit", negative values indicate higher climate sensitivity for a "cold orbit" obliquity setting.

For transient CO_2 forcing, high obliquity (warm orbit) shows a stronger climate sensitivity (60–90°N) for seasonal Arctic sea-ice cover, especially during winter months (Fig. 3.3.7, upper panel). However, after crossing the threshold, the model study with low obliquity settings (cold orbit) shows increased sensitivity to obliquity forcing (Fig. 3.3.7, lower panel). Towards the equator the signal is strongly dampened.

3.4 Discussion

3.4.1 Deconvolution of the synergy from the combined orbital impact

The end members of obliquity and precession simulations show a strong amplification of SAT especially in the Arctic region (Fig. 3.3.1). Obliquity modulates the latitudinal distribution of insolation, preferentially affecting sea-ice in both hemispheres, whereas precession typically alters the seasonality of the signal. Synchronous obliquity forcing at the poles can be seen in the SAT anomaly, whereas precession forcing does not cause appreciable warming in the Antarctic (Fig. 3.3.1). Yet, based on different forcing mechanisms (latitudinal change versus seasonal change in insolation), precession forcing has the ability to mimic a mean SAT signal in the Arctic as obliquity. Both, obliquity and precession exhibit a strong impact on sea-ice changes and thus on climate (Gallimore and Kutzbach, 1995; Jackson and Broccoli, 2003; Tuenter et al., 2005). Most of the orbital signal is imprinted in temperature anomalies at the sea-ice border, whereas thick sea-ice in the Arctic interior remains almost unaffected, consistent with former modeling studies (Tuenter et al., 2005). Additionally consistent with our results, climate models do not show strong synergistic effects (e.g. Valdes, 2011; Willeit et al., 2013). Still, Willeit et al. (2013) use a model of intermediate complexity with ice-sheet dynamics and reproduce global temperatures comparable to the late Pliocene. This model data conformance is fitted by tuning orbital parameters within a reasonable range, based on the assumption that the proxy record is biased towards warm temperatures (Willeit et al., 2013).

It appears that the monocausal impact of obliquity and precession almost equals the combined effect (Fig. 3.3.3). The sea-ice component does not show a strong nonlinear response to the applied orbital forcing. Jackson and Broccoli (2003) show that sea-ice thickness has the strongest nonlinear response to orbital forcing (see also Fig. 3.3.6), but annual mean sea-ice concentration is much less sensitive. Negative synergies are observed at the Arctic sea-ice edge for Pre-industrial and Tortonian at 278 ppmv CO_2. At higher levels of CO_2, Arctic summer sea-ice, and thus its synergy, is absent, pointing to decreased climate sensitivity (Haywood et al., 2002; Colman and McAvaney, 2009). Available GCMs seem to underestimate important feedback mechanisms including sea-ice and vegetation (Jackson and Broccoli, 2003; Knorr et al., 2011), e.g. the warming and the sea-ice retreat in the Arctic (Boé et al., 2009), or GCMs seem to lack important processes (ice-sheet dynamics, dust forcing, soil genesis; see Chap. 4) (Valdes, 2011).

3.4.2 Orbital forcing at differential CO_2 levels for the Tortonian

In general, Tortonian climate at 278 ppmv CO_2 is similarly sensitive to orbital forcing (Fig. 3.3.2) as the pre-industrial model runs (Fig. 3.3.1). Arctic warming due to sea-ice feedback is not only limited to the Barents/Labrador Sea, but also expands into the Arctic Ocean and the circum-Arctic continents. Tortonian boundary conditions (tectonic settings) moderately increase global mean SAT by +0.7°C compared to Pre-industrial (Knorr et al., 2011). This temperature offset enhances climate sensitivity to orbital forcing (obliquity and precession) due to decreasing Arctic sea-ice cover especially during summer with additional warming of Arctic surface waters (Fig. 3.3.4a, c and b, d). Knorr et al. (2011) argue, that the anomaly of Tortonian and pre-industrial climate at pre-industrial CO_2 levels (278 ppmv)

is more sensitive than the anomaly of Tortonian and pre-industrial climate at modern CO_2 levels (360 ppmv) (Micheels et al., 2011). The reason is a larger potential for sea-ice changes and associated feedbacks in a colder climate state. Holland and Bitz (2003) confirm that polar amplification is largely depending on the sea-ice state in the reference model run. Further, they relate strongest polar amplification to relative thin Arctic sea-ice in the control climate.

Nevertheless, if we compare the sensitivity of orbital forcing in the Arctic for a Tortonian setup (278 ppmv CO_2) to a simulation with elevated CO_2 levels (450 ppmv CO_2), the mean SAT warming signal is strongly dampened (Fig. 3.3.2). This is consistent with a warmer, CO_2 forced climate and weakened albedo feedback, which decreases climate sensitivity (Colman and McAvaney, 2009). At high summer insolation the nonlinear effect of summer sea-ice disappears, which effectively dampens the mean SAT anomaly for obliquity and precession forcing in the Arctic. Since obliquity preferentially affects polar regions >60° latitude (Raymo and Huybers, 2008), the imprint of obliquity on the global mean temperature rarely shows nonlinearity (as for Pre-industrial) whereas precession still has some global temperature imprint (Table 3.1). In Arctic marine sediments from the Eocene Pälike et al. (2008) and Sangiorgi et al. (2008) confirm that obliquity and precession forcing is similar in magnitude and dominates in the central Arctic Ocean. Sangiorgi et al. (2008) point out that, consistent to our studies and others (Gallimore and Kutzbach, 1995; Jackson and Broccoli, 2003; Tuenter et al., 2005), sea-ice mediates the effect of orbital forcing to climate.

In the study of Jackson and Broccoli (2003), who utilize an atmosphere-slab ocean model with a dynamic/thermodynamic sea-ice component for Pre-industrial, sea-ice increases due to a reduced tilt of the Earth‘s axis of rotation and the occurrence of the aphelion in late spring, which increases snowfall.Dominantly the Arctic sea-ice increase in late autumn, which enhances the meridional temperature gradient, and thus storm activity, which fosters increased snowfall. At these orbital settings, potential snow ablation is reduced due to increased snowfall and terrestrial ice-volume is primarily determined by local changes in insolation (Jackson and Broccoli, 2003). Here, the model studies with combined obliquity and precession setting show major SAT changes around Greenland caused by changes of sea-ice cover, especially for the model studies with low atmospheric CO_2 (278 ppmv).

3.4.3 The Arctic sea-ice as a mediator from obliquity forcing into a climate signal

How does Arctic sea-ice (seasonal and perennial) mediate obliquity forcing into a climate signal? In order to achieve a better mechanistic understanding, the results presented in Sect. 3.3.5 are plotted in a simplified sketch (Fig. 3.4.1).

Even at high atmospheric CO_2 values, winter Arctic sea-ice persists, regardless the strength of obliquity forcing. However, high obliquity increases summer insolation, warms the upper ocean layer and thus delays sea-ice formation through subsequent heat release during the autumn and winter season (warm signal especially in the winter period at 60–90°N latitude, Fig. 3.3.7). As a consequence, annual global SAT rises. At this stage, the direct influence of obliquity forcing on sea-ice does not include the nonlinearity of sea-ice albedo feedbacks. Hence, a high end member obliquity forcing experiment exhibits stronger than expected SAT response. Consistently, global warming due to CO_2 forcing generally decreases climate sensitivity due to the decrease of the strong albedo feedback (Colman and McAvaney, 2009).

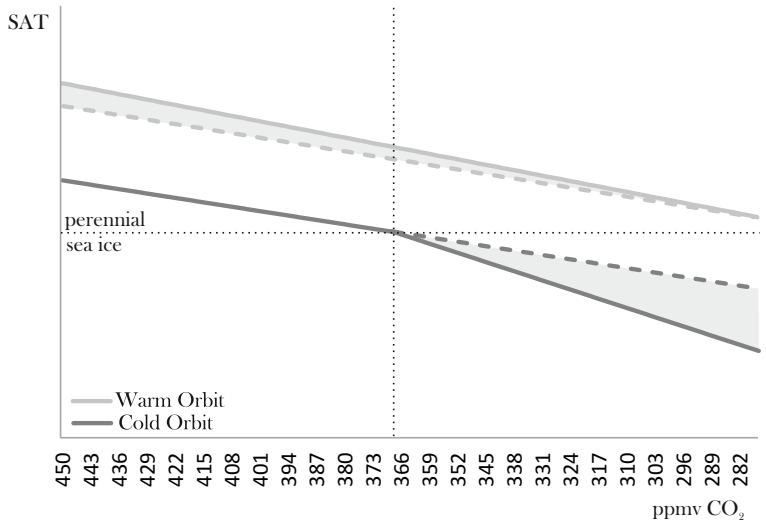

Figure 3.4.1: Nonlinear surface air temperature (SAT) response to orbital forcing at different CO_2 levels. The simplified sketch is based on results of Sect. 3.3.5. Dashed lines indicate a linear SAT response, solid lines represent the actual SAT response, and shaded areas indicate the nonlinear effect in the SAT signal.

Along with declining CO_2 values, low obliquity (cold orbit), rather than high obliquity (warm orbit) favors the transition from seasonal to perennial sea-ice cover. The fraction of sea-ice, that persists the summer season, expands and thickens in the subsequent winter period, equivalent to glacier formation. Hence, ice volume accumulates until a thermodynamical limit is reached (Fig. 3.3.6). The associated sea-ice albedo feedback causes additional cooling of the polar region, especially by delaying early spring surface warming and accelerating autumn cooling (Fig. 3.3.7, right panel). This finding is consistent with Jackson and Broccoli (2003). At this CO_2 regime, stronger summer insolation due to a high obliquity forcing is still sufficient to prevent the appearance of perennial sea-ice, which limits the impact of the albedo sea-ice feedback on SAT. Since sea-ice albedo directly influences summer insolation and energy budget, it poses a strong positive feedback. Hence, a low end member of obliquity exhibits a stronger than expected SAT response. In the context of our studies, the Tortonian setup at 278 ppmv CO_2 shows the strongest sensitivity to orbital forcing in a cold climate.

3.5 Conclusions

The model sensitivity studies presented here point out that the imprint of orbital forcing is highly depending on the actual background climate state which sets the climate sensitivity. At high levels of CO_2, the absence of summer sea-ice mainly cancels out the sea-ice albedo feedback and the associated synergy. Inversely, model studies with pre-industrial CO_2 values show a stronger sensitivity towards a colder climate.

Lisiecki and Raymo (2005) compiled a global $\delta^{18}O$ stack of benthic foraminifera comprising the last 5.3 myr. This proxy mainly records glacial/interglacial cycles via global ice volume.

During the initiation of Northern Hemisphere glaciation about 3 myr ago, glacial cycles had a 41-kyr periodicity (3.0–0.8 myr). This time period of the geological history is therefore referred to as the "41-kyr world", congruent with the obliquity period (Tiedemann et al., 1994).

The amplitude of pre-Pleistocene glacial cycles, recorded in the global $\delta^{18}O$ stack is about half compared to late Pleistocene glaciations, implying the presence of smaller ice-sheets. At orbital settings characterized by high summer insolation, the small ice-sheets melt before the succeeding glacial cycle incepts. Thus Northern Hemisphere glaciation was a rather gradual process (Mudelsee and Raymo, 2005), influenced by other climate parameters, like greenhouse gases.

Ganopolski and Calov (2011) perform climate simulations of varying CO_2 concentrations (200–260 ppmv CO_2) in an Earth system model of intermediate complexity (EMIC) with ice-sheet dynamics. They find that the glacial cycles of the last 1 myr (100 kyr period) can be reproduced. A higher atmospheric CO_2 concentration (280 ppmv CO_2) lowers the amplitude of glacial periods, and shifts the power in the frequency domain toward obliquity and precession. Studies with an ice-sheet model applied for the late Pliocene (3.3–3.0 myr) support the idea of milder and wetter orbital forced glacial cycles at 400 ppmv CO_2 (Dolan et al., 2011). Prior the onset of Northern Hemisphere glaciation, CO_2 levels were around 400 ppmv CO_2 (Raymo et al., 1996; Jansen et al., 2007), and dropped to less than 300 ppmv CO_2 until 2.1 myr ago (Hönisch et al., 2009). In the context of our transient CO_2 forcing (450→278 ppmv CO_2) without ice-sheet dynamics, climate shows a stronger sensitivity towards obliquity (Fig. 3.3.2, Table 3.1). This happens after crossing a critical threshold at ca. 365 ppmv CO_2, when a perennial sea-ice cover evolves (at settings of a "cold orbit", Fig. 3.3.6). In comparison with ice-sheet dynamics, the fast response of sea-ice (PALEOSENS Project Members; Rohling et al., 2012) might serve as a precursor for sustaining snow-fields in Greenland for ice-sheet build-up (Dong and Valdes, 1995; Jackson and Broccoli, 2003; Koenig et al., 2011). Ravelo et al. (2004) elucidate a rising impact of solar forcing on the benthic foraminifera $\delta^{18}O$ record between 4.0-2.0 myr ago. However, they relate stronger climate sensitivity within this period to an increase in the thermocline depth and upwelling in tropical and/or subtropical ocean regions, that established/enhanced the Walker circulation (Ravelo et al., 2004).

A remarkable sediment borehole record, retrieved from the central Arctic Ocean (ACEX), strongly indicates a permanent Arctic sea-ice cover for the last ca. 14 myr (Moran et al., 2006; Darby and Zimmerman, 2008; Haley et al., 2008; Krylov et al., 2008; St. John, 2008) consistent with prevalent cool climate conditions during this period (Shevenell et al., 2004). However, within the Neogene, warm climate excursions potentially favored the establishment of a seasonally ice-free Arctic ocean, as indicated by SST reconstructions of the late Pliocene (Dowsett et al., 2009).

Chapter 4

Dynamic soil feedbacks on the climate of the mid-Holocene and the Last Glacial Maximum

4.1 Soil interaction—A missing feedback in climate models?

As yet, climate sensitivity on long timescales is still underestimated by GCMs (e.g. Pagani et al., 2010; Valdes, 2011). Proxy records from the "hothouse" tectonic past (late Cretaceous, Cenozoic) indicate a decreased meridional global temperature gradient with amplified warming in polar regions, known as "equable climate" (Jenkyns et al., 2004; Moran et al., 2006; Huber and Caballero, 2011; Salzmann et al., in revision). Additionally to elevated atmospheric CO_2 levels, plausible mechanisms that reconcile modeling results and proxy data have been proposed (polar stratospheric clouds, vegetation dynamics, oceanic heat transport, orbital parameters; Sloan et al., 1995; Otto-Bliesner and Upchurch, 1997; Sloan and Morrill, 1998; Sloan and Pollard, 1998; Kump and Pollard, 2008; Willeit et al., 2013). Another potential mechanism, which has not yet been accounted for in Earth system models with land surface dynamics, is pedogenesis. In general, soil genesis is controlled by time, parent material, topography, climate, vegetation (and humankind) (Jenny, 1941). So far general circulation models (GCMs), trained to simulate present and thus future climate scenarios for the next ca. 100–300 yr (Meinshausen et al., 2011), do not account for soil development. The typical timescale of pedogenesis is in the order of 100–1000 yr and more (Jenny, 1941), but degradation of soils by erosion due to land cover change, e.g. deforestation, can occur on much shorter timescales. It has been speculated for instance, that intensive land use, and thus the exposure of bright underlying soils in the Sahel zone triggered the inter-decadal drought event ca. 1969 (Nicholson et al., 1998). In analogy to modern climate, the Sahel also has undergone dramatic desertification during the mid-Holocene about 5500 yr ago (Foley et al., 2003). A rather immediate change from humid mid-Holocene conditions to desertification of the Sahel due to a gradual change of orbital parameters suggests the presence of strong nonlinearities in the

climate system of that region. Many modeling studies have investigated the intensification of Holocene wind systems in North Africa (e.g. Kutzbach and Otto-Bliesner, 1982; Kutzbach and Street-Perrott, 1985; Kutzbach and Guetter, 1986; deMenocal and Rind, 1993) resulting in decreased Sahara desert area and a northward shift of the Sahel. Such evidence has been retrieved from various proxy records, e.g. abundant pollen data in marine (Dupont, 2011) and terrestrial archives (Prentice et al., 2000; Bartlein et al., 2011), the presence of paleolakes (Petit-Maire and Riser, 1981; Hoelzmann et al., 1998, 2000), traces of human migration and inhabitation (Petit-Maire, 1989), skeletal remnants of herbivores (Petit-Maire and Riser, 1981; Petit-Maire, 1989) and rock engravings (McIntosh and McIntosh, 1983). The cause of intensified Holocene wind systems in North Africa is supposed to be increased seasonal contrast of solar radiation (and higher insolation in the northern high latitudes, Berger, 1978), since atmospheric greenhouse gases at that time were close to pre-industrial values (Petit et al., 1999). Basically the concept of fast land surface heating, compared to the inertia of ocean heating during the spring to summer transition, results in inland moisture convergence and strong precipitation events. Based on the theory of land to ocean temperature contrast (Charney, 1975; Charney et al., 1977), model studies with modifications in the Earth's orbital parameters gradually investigated the impact of increased Atlantic SSTs (e.g. Kutzbach et al., 1996; Texier et al., 2000; Zhao et al., 2005), feedbacks by vegetation migration (Kutzbach et al., 1996; Texier et al., 1997; Claussen and Gayler, 1997; Claussen, 1997; Braconnot et al., 1999; Texier et al., 2000; Braconnot et al., 2007), enhanced land evapotranspiration through higher abundance of lakes and wetlands (Coe and Bonan, 1997; Broström et al., 1998; Carrington et al., 2001; Krinner et al., 2012), and increased water holding field capacities in soils (Levis et al., 2004) and a decrease in land surface albedo (Bonfils et al., 2001; Levis et al., 2004; Knorr and Schnitzler, 2006; Schurgers et al., 2007; Vamborg et al., 2011) on the moisture content transported with the African wind system. Actually, numerical models that take into account integrated atmosphere-ocean-vegetation feedbacks are evaluated to represent the mid-Holocene African monsoon more realistically (Braconnot et al., 2007). Several studies highlight the role of pedogenesis in influencing the land surface energy balance, water recycling and thus vegetation impact, which might be crucial for Holocene climate simulations, future climate scenarios, or the investigation of climate on tectonic timescales (Kutzbach et al., 1996; Doherty et al., 2000; Levis et al., 2004; Knorr and Schnitzler, 2006; Shellito and Sloan, 2006; Wanner et al., 2008; Brovkin et al., 2009; Micheels et al., 2009; Knorr et al., 2011; Krapp and Jungclaus, 2011; Vamborg et al., 2011). Furthermore, model studies that test the sensitivity of land surface albedo highlight the importance to achieve for a realistic representation of background albedo (Kutzbach et al., 1996; Levis et al., 2004; Knorr and Schnitzler, 2006; Jiang, 2008). Recently, Vamborg et al. (2011) dynamically computed foliage litter in a GCM with dynamical vegetation. The result is a reduction of land surface albedo due to soil darkening that leads to a strengthening of the mid-Holocene African wind system. Apart from that, present-day studies highlight the importance of soil moisture as a feedback on precipitation (e.g. Bergengren et al., 2001; Douville et al., 2001, 2007) and for modulating local seasonal precipitation (e.g. Seneviratne et al., 2006, 2010). In an atmospheric GCM study, Wang (1999) associated the adjuncts of finer soil texture and darker soils with vegetation reconstructions of the mid-Holocene. This results in intensified East Asian rainfall and improved quantitative agreement to proxy records. As another important mechanism, Levis et al. (2004) isolate the effect of modified soil texture from desert sand to loam which increases soil water retention. They find a weak

but widespread increase of evapotranspiration at the Sahara, but the North African rain belt is dominated by modified land albedo. Continuatively Jiang (2008) investigated the role of physical soil characteristics (soil color, soil texture) for the LGM by using an atmospheric GCM that has been asynchronously coupled to a terrestrial biosphere model. Jiang (2008) iteratively adapted soil characteristics where the absolute simulated vegetation in a grid cell has changed. The integrated vegetation-soil feedback reinforced glacial cooling to some extent (Jiang, 2008).

The advent of coupling vegetation with climate models was initiated by Henderson-Sellers (1993) and Claussen (1994). As a starting point, Henderson-Sellers (1993) used a version of the Holdridge (1947) life zone classification, condensed into ten different continental vegetation classes. This approximation was necessary to translate the classification to ecotypes of the Biosphere-Atmosphere Transfer Scheme, that was coupled to the atmospheric model CCM1 (Williamson et al., 1987). In a parallel approach Claussen (1994) used the equilibrium vegetation model BIOME1 by Prentice et al. (1992) and applied an asynchronous coupling technique with the AGCM ECHAM3 (Roeckner et al., 1992). Therein, ECHAM3 computes climate data fields in a first step, that are passed in a second step to BIOME1 to calculate an equilibrium plant distribution. Subsequently the physical parameters of simulated vegetation types are used to reinitialize the boundary conditions of the atmosphere model. This procedure is iteratively repeated until vegetation and climate model are equilibrated (Claussen, 1994). After recognizing their importance, dynamical vegetation models became fully integrated into GCMs (e.g. Foley et al., 1994, 2000). Here, we introduce a simple equilibrium soil scheme, asynchronously coupled to COSMOS-ASO, that has been inspired by the procedure of Claussen (1994). The purpose of this scheme (COSMOS-ASO$_{\mathrm{sol}}$) is to capture biogeophysical feedbacks between soil genesis/degradation and climate as proposed by Levis et al. (2004). The effect of the soil feedback is tested in climate simulations that represent a warm (mid-Holocene) and cold (LGM) climate relative to Pre-industrial, and the results are compared to geological data in order to set a range of potential soil impact on global climate for glacial and interglacial periods of the Quaternary.

4.2 Results

4.2.1 Pre-industrial simulation

In Fig. 4.2.1 global surface air temperature, precipitation and evaporation anomalies of PI_sol-PI_ctl are shown. At high northern latitudes surface air temperatures are locally increased by about 1°C at the Canadian Archipelago and Baffin Bay affected by reduced sea-ice cover in consequence of a change in soil characteristics. In general reduced sea-ice cover is observed in areas around the coasts encapsulating the Arctic Ocean and Barents Sea as well as the Antarctic continent. The Arabian Peninsula/Sahara desert parametrization exhibits anomalies in the surface radiation balance which are related to deviations in land albedo compared to the original input-file of PI_ctl. The soil albedo directly reflects a temperature signal because of the absence of vegetation cover in this area. Regional temperature anomalies vary from -3.2°C (desert regions in South Asia) to +2.3°C (Sahara desert) where the land albedo is over- (+0.14) or underestimated (-0.08), respectively. The surface of the Southern Ocean is warming due to reduced sea-ice cover and a decrease in strength of the Atlantic Meridional Overturning Circulation (AMOC) which is accompanied by a lesser heat advection

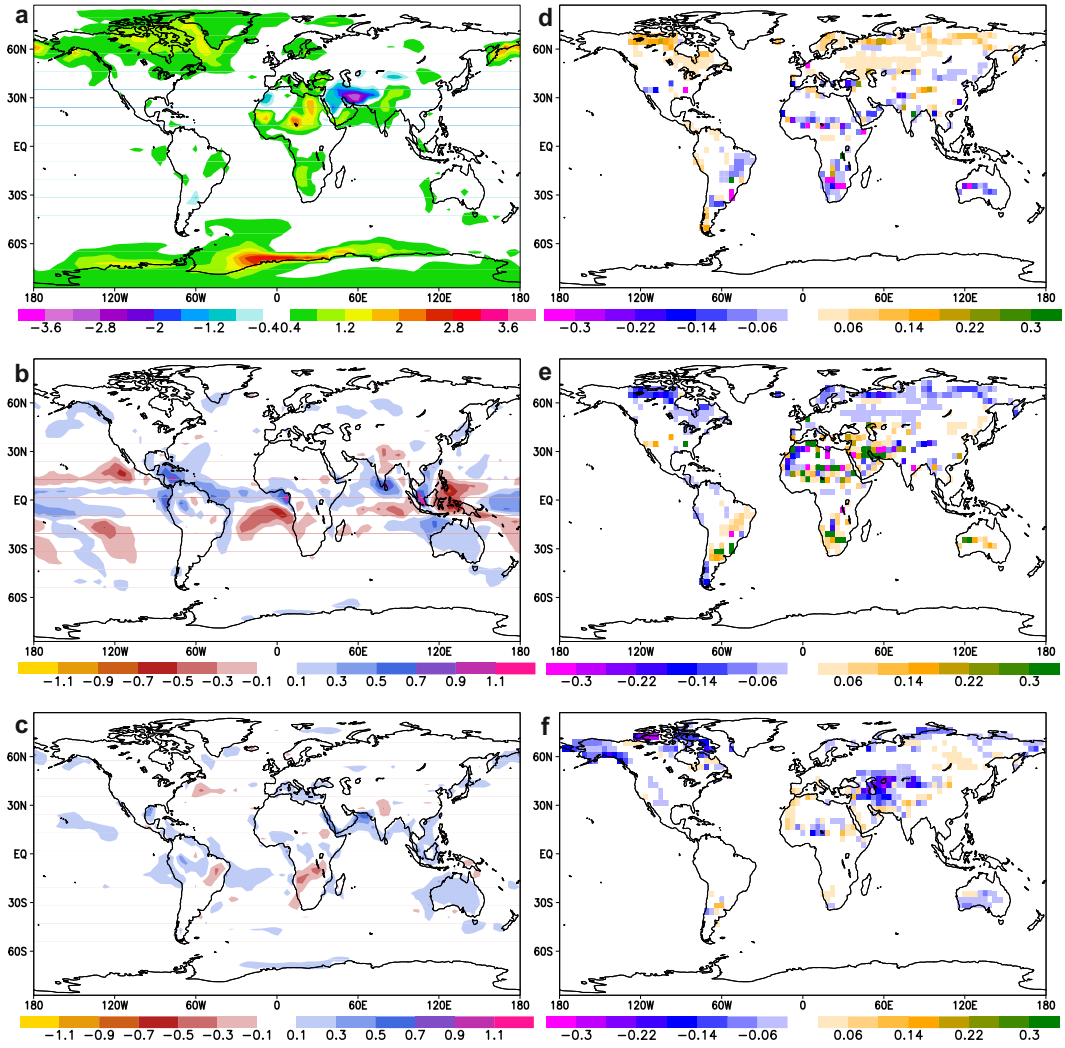

Figure 4.2.1: Differences in 100 yr mean of the pre-industrial climate state with included soil dynamics and fixed soil characteristics (PI_sol-PI_ctl) for (a) surface air temperature in °C, (b) total precipitation in mm day^{-1}, (c) evaporation in kg m^{-2} day^{-1}, (d) forest fraction, (e) grass fraction and (f) desert fraction.

from the South. Here the AMOC is reduced by 1 Sv (1 Sv = $1\times10^6 m^3 s^{-1}$) compared to the pre-industrial run (16 Sv). In Fig. 4.2.1b total precipitation shows some regional anomaly patterns in lower latitudes, i.e. an anomalous northward shift of the Indonesian rainfall, and increased precipitation in tropical rainforests. A similar pattern is observed in the evaporation anomaly (Fig. 4.2.1c). In general the global pattern of water holding field capacities is reasonably captured by our simulation (not shown), thus underestimating maximum values in the tropics and east of China by our soil lookup-table (Table 2.2). The soil scheme overestimates field water capacities in North Europe and North America where soil progression is lagged by deglacial ice sheet retreat. Since there is no time-dependent function of soil evolution in our soil scheme, our model exhibits an equilibrated final state of the physical soil characteristics in these regions. Globally the water holding field capacity of soil becomes higher (+0.06 m) than PI_ctl (0.63 m) but the global inventory of soil water is slightly reduced (-0.008 m). Further, evaporative processes over land increase (0.012 mm day^{-1}) and land surface runoff and drainage is increased (+0.014 mm day^{-1}) but compensated by the atmospheric exchange of fluxes via total precipitation over land (+0.027 mm day^{-1}). The global mean of surface air temperature is increased by +0.27°C. In PI_sol the simulated forest cover slightly increases in high latitudes and decreases in subtropical regions where it is replaced by grass cover (Fig. 4.2.1d, e). The inclusion of the soil scheme particularly favors the expansion of forests by reduced temperatures of the coldest month especially in the northeast of Canada, the Canadian Archipelago (2-5°C) and North Siberia (ca. 1°C). In the subtropical areas grass cover increases to the expense of forest cover mainly due to an underestimation of the calculated water field capacity of soils in the soil scheme.

4.2.2 Mid-Holocene climate

The mid-Holocene simulation HOL_sol is characterized by a redistribution of solar radiation caused by modified settings of the orbital parameters and a reduced level of methane content in the atmosphere (650 parts per billion) compared to CTL_sol which leads to an overall warming of +0.34°C. Most of the warming anomaly can be found in high northern latitudes especially in the Barents Sea (>7°C), where sea-ice retreats (Fig. 4.2.2). A moderate warming of ca. 1°C is observed in the tropics as well as some local areas of the Sahara and the Arabian Peninsula. Regional cooling from -1 to -3°C is located in typical monsoon regions like Sahel and India. The precipitation anomaly (Fig. 4.2.3) confirms that land surface cooling occurs in areas of high precipitation and evaporation (Fig. 4.2.4) consistent with increased latent heat fluxes. The northward shift of the precipitation anomaly causes reduced rainout above Brazil, South Africa and Australia, thus causes decreasing tropical forest cover there (Fig. 4.2.5). Therefore reduced evapotranspiration in the tropics results in a warming anomaly in consequence of less latent heat transfer. The mid-Holocene land surface is described by higher occurrence of forests (+2.6%) in expense of grassland and a decline in the desert fraction (-4.4%). In more detail trees are more abundant in North Canada and North Siberia as well as the Sahara/Sahel boundary, but reduced in some other regions, in Europe for instance. Nevertheless grass cover increases in total (+0.8%) especially in the Sahara, whereas desert reduces at the southern boundary of the Sahara and in high northern latitudes. Since terrestrial vegetation beyond Sahara/Sahel does not exceed 50%, adaption of soil characteristics is not applied (see Sect. 2.1.2).

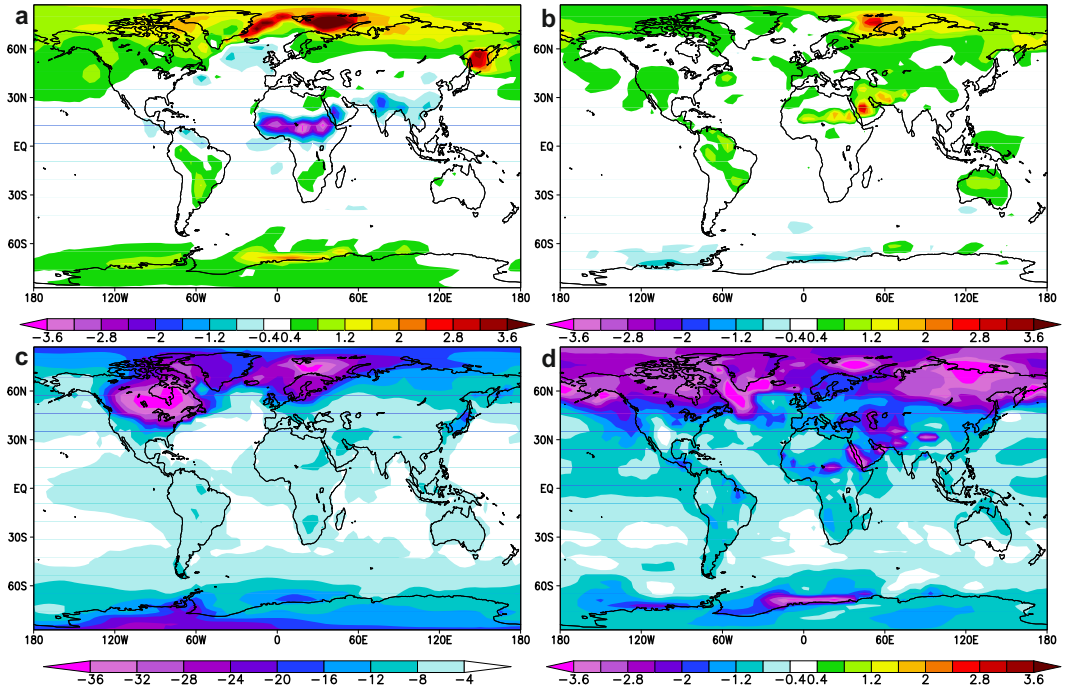

Figure 4.2.2: Surface air temperature (°C) anomalies of a 100 yr mean climate state with respect to Pre-industrial for (a) mid-Holocene (HOL_sol-PI_sol), (b) mid-Holocene soil feedback ( ), (c) Last Glacial Maximum (LGM_sol-PI_sol), (d) Last Glacial Maximum soil feedback ($\hat{f}_{LGM,sol}$).

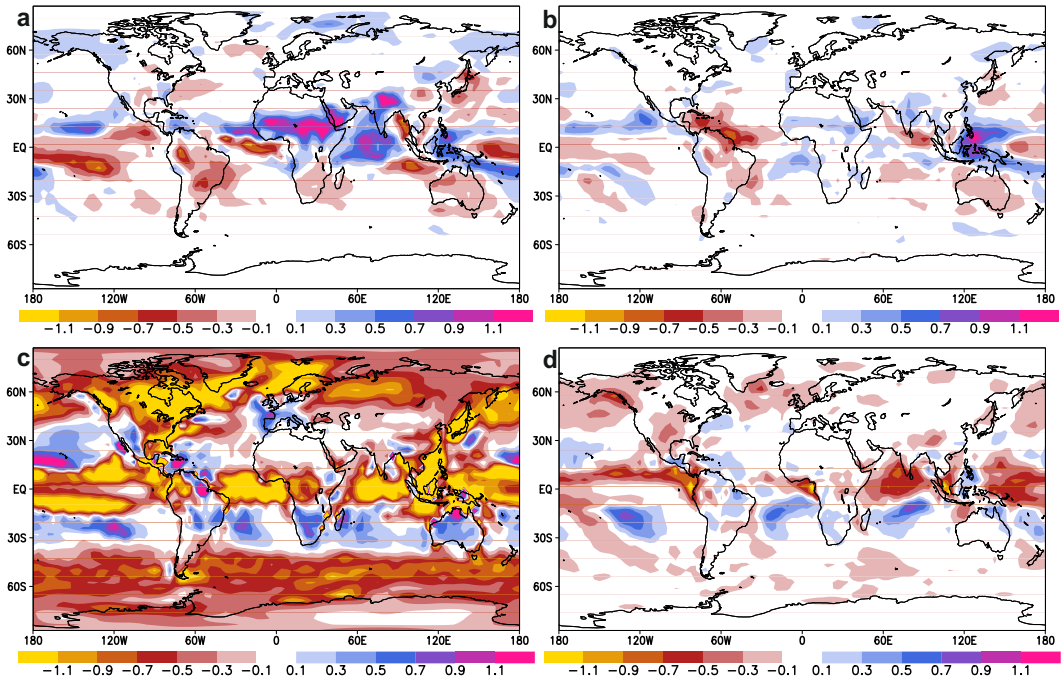

Figure 4.2.3: Total precipitation (mm day^{-1}) anomalies of a 100 yr mean climate state with respect to Pre-industrial for (a) mid-Holocene (HOL_sol-PI_sol), (b) mid-Holocene soil feedback ($\hat{f}_{HOL,sol}$), (c) Last Glacial Maximum (LGM_sol-PI_sol), (d) Last Glacial Maximum soil feedback ($\hat{f}_{LGM,sol}$).

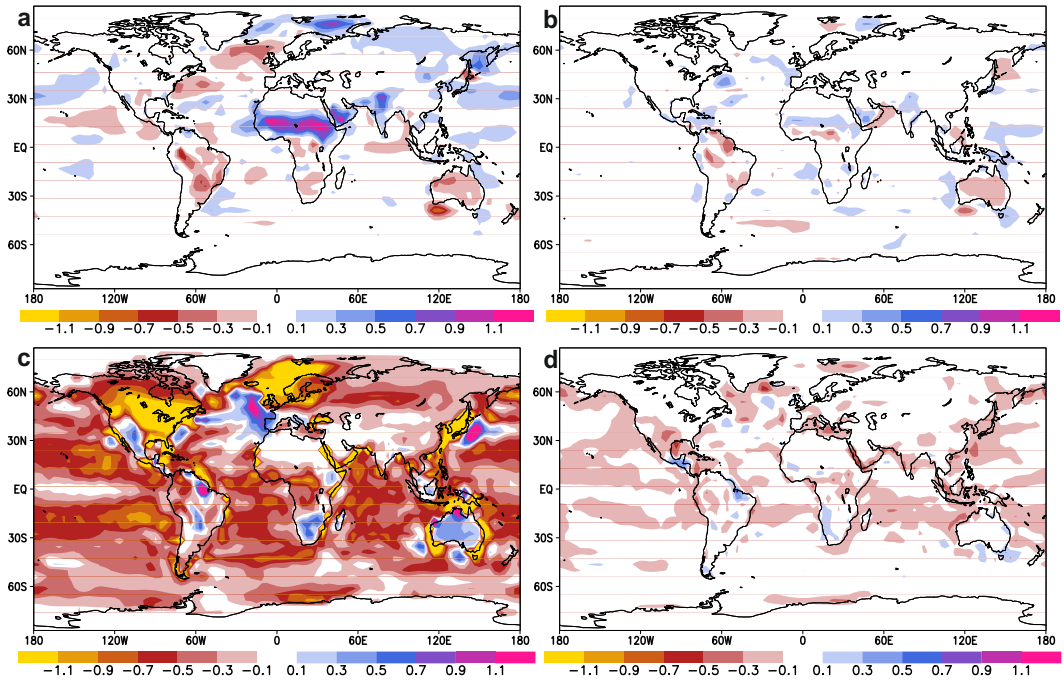

Figure 4.2.4: Evaporation ($\mathrm{kg\,m^{-2}\,day^{-1}}$) anomalies of a 100 yr mean climate state with respect to Pre-industrial for (a) mid-Holocene (HOL_sol-PI_sol), (b) mid-Holocene soil feedback ($\hat{f}_{HOL,sol}$), (c) Last Glacial Maximum (LGM_sol-PI_sol), (d) Last Glacial Maximum soil feedback ($\hat{f}_{LGM,sol}$).

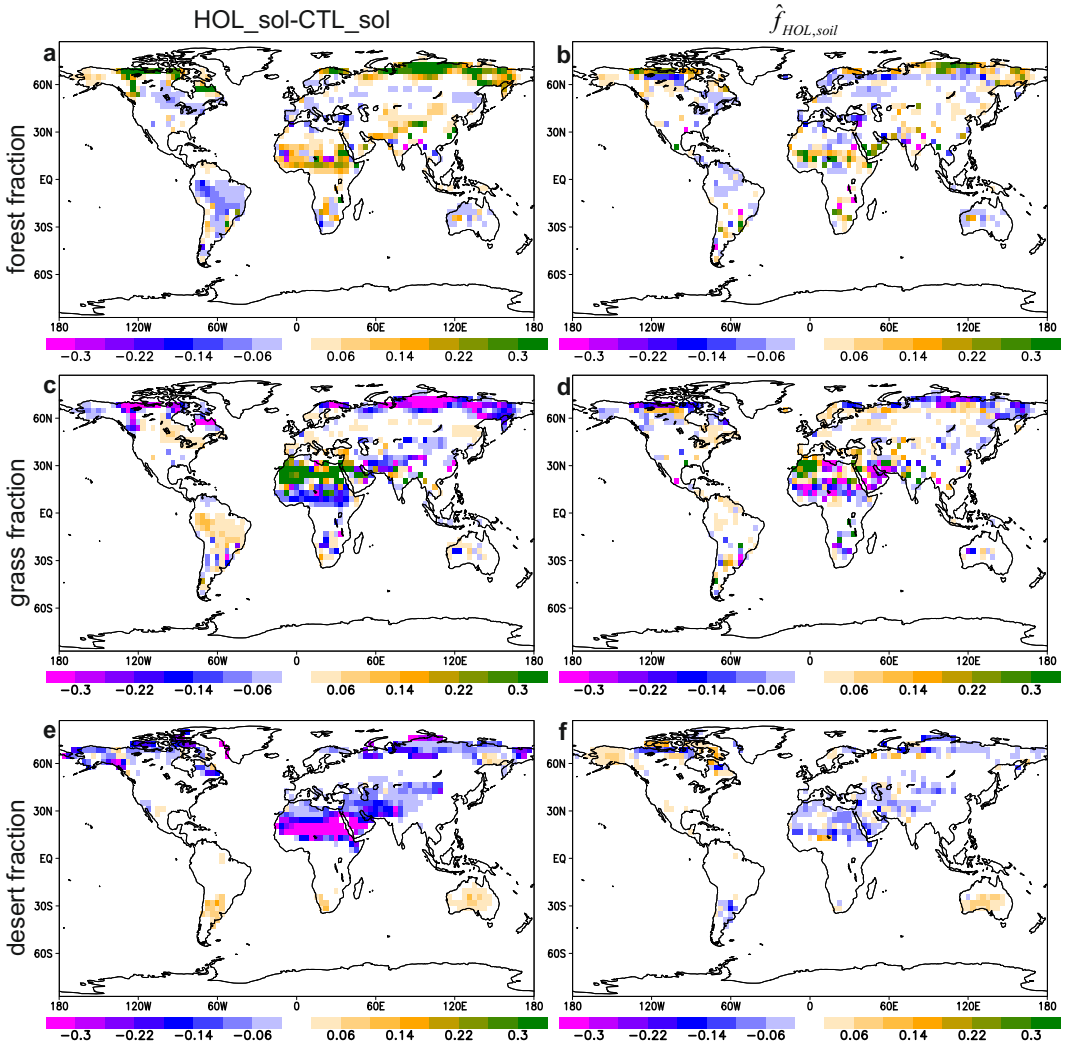

Figure 4.2.5: Vegetation differences in 100 yr mean of the mid-Holocene and pre-industrial climate state with included soil dynamics (HOL_sol-PI_sol) and enclosed soil feedback ($\hat{f}_{HOL,sol}$), for (a) forest fraction and (b) soil impact on forest fraction, (c) grass fraction and (d) soil impact on grass fraction, (e) desert fraction and (f) soil impact on desert fraction.

4.2.3 LGM climate

A modified configuration of the Earth orbit, adapted greenhouse gas concentrations in the atmosphere, expansion of the LGM ice sheets in height and surface area as well as a sea level drop, following the protocol of PMIP3, lead to a subsequent global surface cooling of -7.03°C. The strongest cooling is located at the peak of ice sheets and Nordic Seas, where a perennial sea-ice cover evolves (Fig. 4.2.2). The impact of the introduced soil scheme results in an additional cooling of -1.07°C with highest anomalies in high northern latitudes and some regional cooling anomalies at subtropical land surface spots. In the atmosphere the absolute air humidity is strongly reduced which dampens precipitation (Fig. 4.2.3) and evaporation (Fig. 4.2.4) in a glacial climate. The total precipitation decreases at the equator in the inner tropical convergence zone and latitudes >40° in global mean by -0.42 mm day^{-1}. The expansion of sea-ice cover towards the equator reduces water vapor transport to the poles, forcing a rainout along the horse latitudes (ca. 30°N, S) where total precipitation is increased (Fig. 4.2.3). The terrestrial vegetation shows a decrease of forest cover (-14.9%) compensated by grass cover (+10%) and expansion of polar and Sahara desert area (+12.7%). Taken into account the additional area of exposed shelf seas, trees (+6% in global mean) and grasses (+7%) can evolve there. A major retreat in boreal forest cover arises in Eurasia in a zonal belt between 50-65°N and at the proximity of the Scandinavian and Laurentide ice-sheets (Fig. 4.2.6). Interestingly, the forest cover slightly increases along the horse latitudes in response to higher precipitation there. The tropical forest cover is dramatically reduced by -59% compared to PI_sol. In most areas grass cover compensates for forest regression. Nevertheless, in areas affected by desert expansion, e.g. Arabian Peninsula, Sahara/Sahel borderline and North Siberia, grassland disappears and bare soil remains.

4.2.4 Dynamic physical soil characteristics and their impact on mid-Holocene and LGM climate

Computed changes of soil albedo and water holding field capacities by the soil scheme under different climate states are shown in Fig. 4.2.7. The soil scheme discriminates soil texture (five types, ranging from clay to sand) only into two types, loam-and-clay under prevailing tropical broadleaved evergreen forest and loam for the residual land surface. For a warmer than pre-industrial climate the global mean field capacity of soil increases by +0.024 m over land surfaces (without ice sheet) especially at the Sahel, transition zone of desert and savannah. Consequently, the global soil water body increases by +0.019 m compared to PI_sol (Fig. 4.2.8). The synergistic term of soils and mid-Holocene climate exhibits an increase of soil wetness of +0.013 m in global mean (Table 4.1).

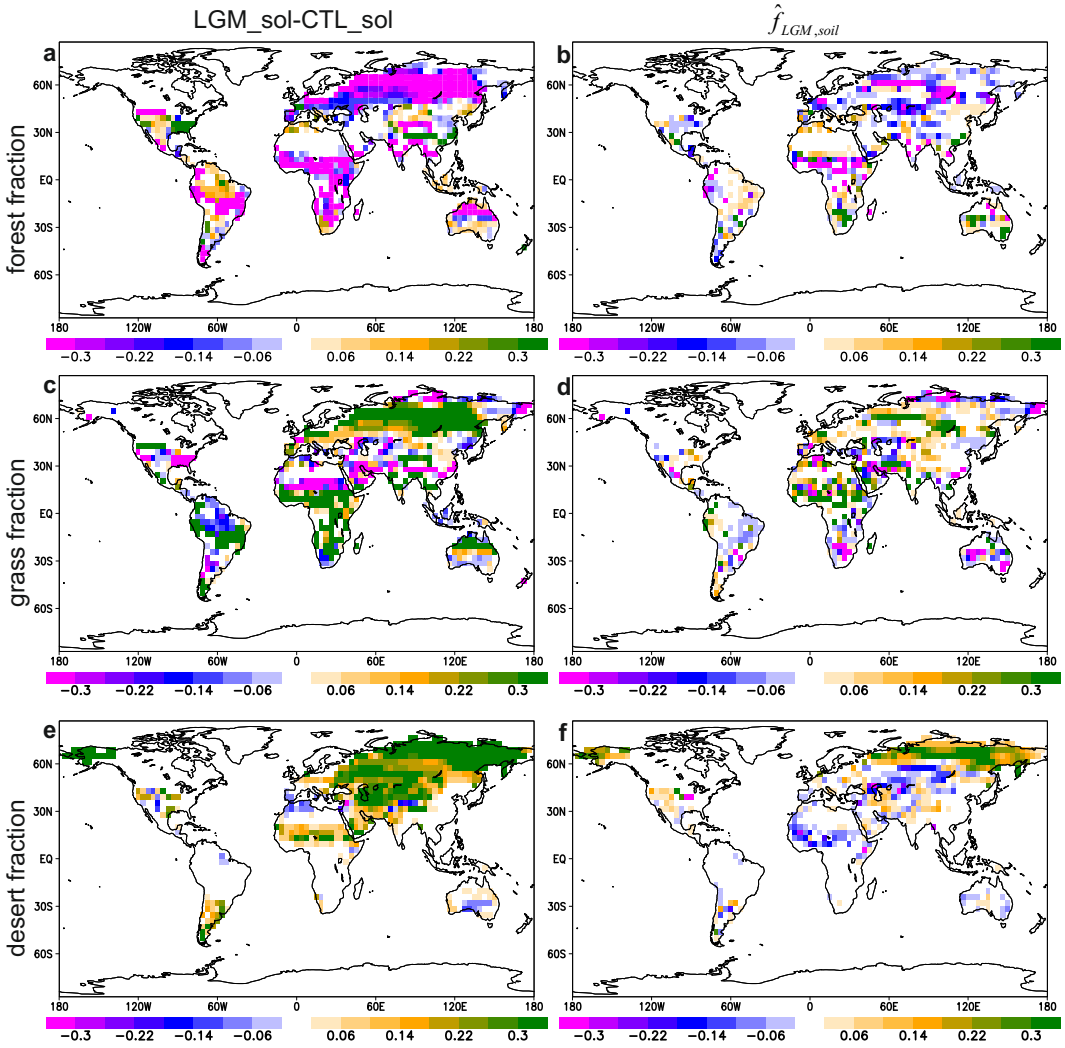

Figure 4.2.6: Vegetation differences in 100 yr mean of the Last Glacial Maximum and pre-industrial climate state with included soil dynamics (LGM_sol-PI_sol) and enclosed soil feedback ($\hat{f}_{LGM,sol}$), for (a) forest fraction and (b) soil impact on forest fraction, (c) grass fraction and (d) soil impact on grass fraction, (e) desert fraction and (f) soil impact on desert fraction.

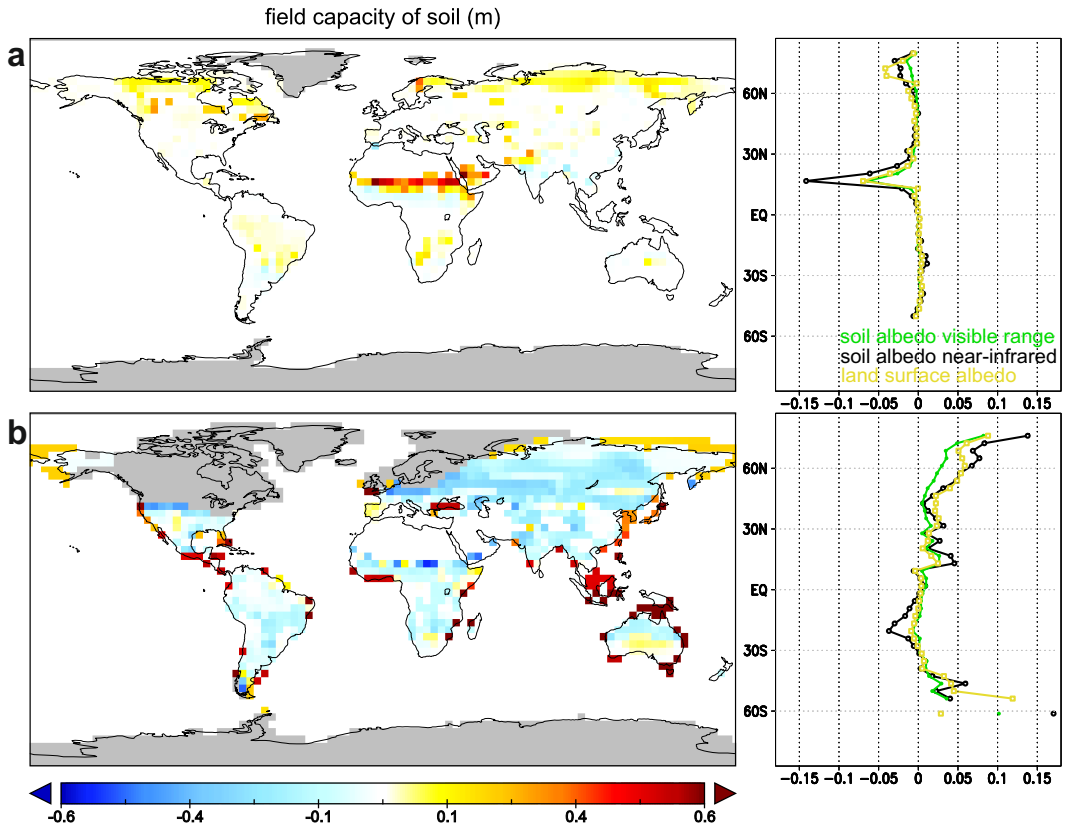

Figure 4.2.7: Changes in water holding field capacities (m) in soils and zonally integrated land surface and soil albedo for (a) mid-Holocene (HOL_sol-PI_sol) and (b) Last Glacial Maximum (LGM_sol-PI_sol).

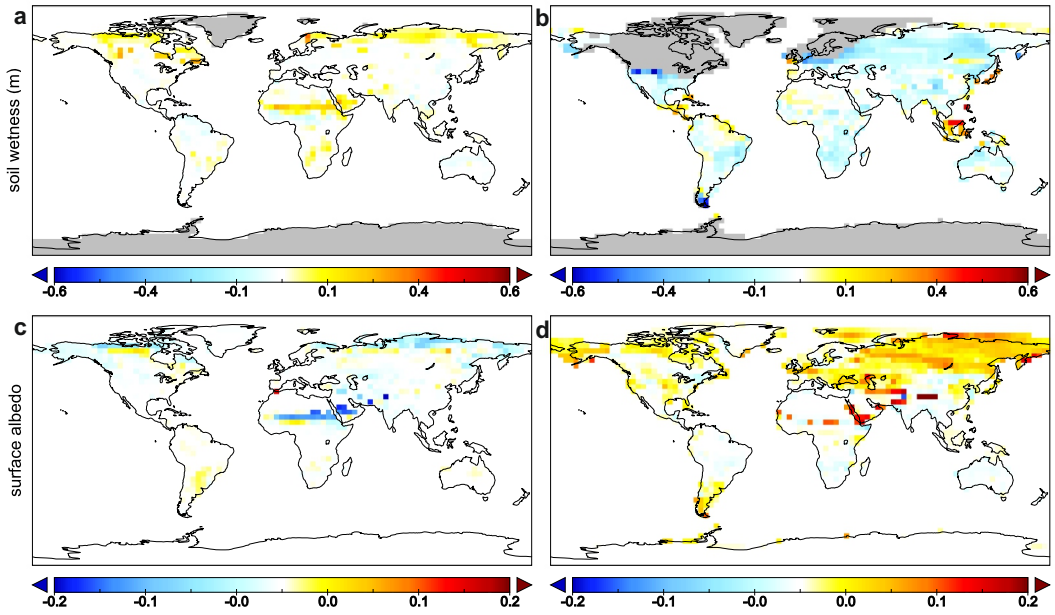

Figure 4.2.8: Soil wetness (m) anomalies of a 100 yr mean climate state with respect to Pre-industrial for (a) mid-Holocene (HOL_sol-PI_sol), (b) and Last Glacial Maximum (LGM_sol-PI_sol) and changes in surface albedo for (c) mid-Holocene and (d) Last Glacial Maximum.

Table 4.1: Global anomalies of land surface characteristics and the contribution of soil feedback for mid-Holocene and Last Glacial Maximum model studies.

	HOL_sol-CTL_sol (syn)	LGM_sol-CTL_sol (syn)	LGM_sol-CTL_sol without exposed shelves (syn)
soil wetness (cm)	1.85 (+1.26)	3.03 (-4.5)	-3.66 (-5.69)
snow depth (in mm water equivalent)	-0.21 (-0.36)	31.6 (-39.3)	9.08 (+8.28)
snow fall ($kg\,m^{-2}\,yr^{-1}$)	-1.03 (-1.25)	-16.9 (+4.26)	16.37 (+3.85)
surface runoff and drainage ($kg\,m^{-2}\,yr^{-1}$)	6.72 (+3.35)	-23.8 (+2.62)	-4.89 (+3.69)
land evaporation ($kg\,m^{-2}\,yr^{-1}$)	26.04 (+5.78)	-139 (-17.3)	-44.2 (-12.8)
skin reservoir content (mm)	0.008 (+0.001)	0.005 (-0.002)	-0.016 (-0.003)
snow accumulation over land ($kg\,m^{-2}\,yr^{-1}$)	0.053 (+0.013)	0.192 (+0.255)	0.027 (+0.13)
maximum field capacity of soil (cm)	2.38 (+2.38)	1.89 (-7.05)	-8.76 (-8.34)
total precipitation over land ($kg\,m^{-2}\,yr^{-1}$)	32.5 (+6.9)	142 (-15)	-46.7 (-9.47)
Po-Eo ($kg\,m^{-2}\,yr^{-1}$)	-2.28 (-1.29)	1.03 (-0.12)	0.68 (-0.35)

Further, an increase of landward water transport (1.29 $kg\,m^{-2}\,yr^{-1}$) from the ocean, land surface runoff and drainage (3.35 $kg\,m^{-2}\,yr^{-1}$) is affected by changes of physical soil properties. The global mean of land surface albedo decreases by -0.011, with maximum anomalies >0.19 at the Sahel region caused by vegetation migration towards the Sahara where it shades the modified soil albedo (Fig. 4.2.2). The integrated zonal mean of high northern latitude land albedo decreases due to a darkening of the soil (Fig. 4.2.7) accompanied by an increased forest cover (Fig. 4.2.5) and less snow cover (Fig. 4.2.9). The forest cover replaces C3 grass cover and thus modifies the soil characteristics: A higher abundance of boreal evergreen forest in the high latitudes leads to a lowering of the soil albedo and higher maximum water holding field capacities compared to soils associated to C3 grasses. Darker soils are generated leading to a change in the local energy budget and higher surface air temperatures adjust which in turn lead to an amplified decrease of polar desert cover, again reinforcing soil genesis (see Sect. 4.2.4). The computed soil characteristics of the LGM model simulation show a global decrease in water holding field capacities (Fig. 4.2.7b), which is overcompensated by soil formation at exposed shelf seas, added to land surface grid cells (Table 4.1). This variable

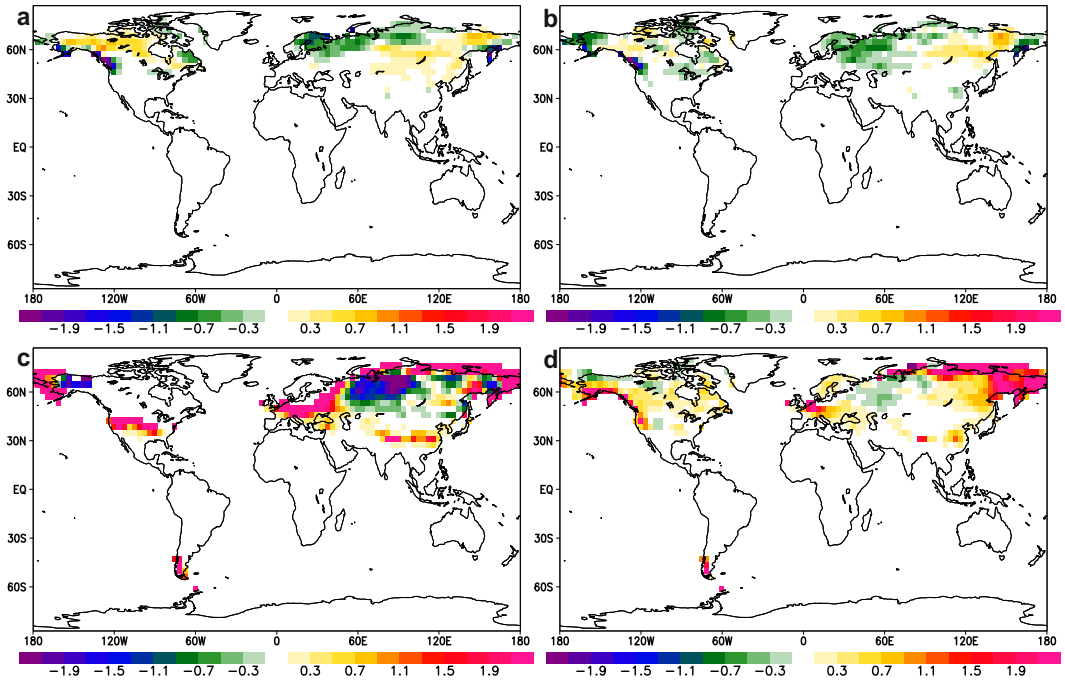

Figure 4.2.9: Snow depth (water equivalent in mm) anomalies of a 100 yr mean climate state with respect to Pre-industrial for (a) mid-Holocene (HOL_sol-PI_sol), (b) mid-Holocene soil feedback ($\hat{f}_{HOL,sol}$), (c) Last Glacial Maximum (LGM_sol-PI_sol), (d) Last Glacial Maximum soil feedback ($\hat{f}_{LGM,sol}$).

strongly modulates soil wetness (Fig. 4.2.8b). Along a zonal mean the soil albedo increases, especially in high latitudes (Fig. 4.2.7b). In consequence, calculated land surface albedo also increases, especially in Asia and in the vicinity of expanding desert areas (Fig. 4.2.8d) due to the expense of grass and forest cover there (Fig. 4.2.6).

Hydrological cycle

A change in physical soil characteristics like water field capacity in soils potentially impacts the hydrological cycle over land. The mid-Holocene model simulation with dynamic geophysical soil characteristics shows increased evaporation over land surface areas contributed by additional moisture flux from the ocean towards land (Table 4.1). Higher land evaporation is supported by an increase in temperature and transpiration of forest (+2.6%) and grass cover (+0.8%) change. Consequently, elevated land precipitation and soil moisture result in increased drainage and land surface runoff. The soil scheme amplifies each of the described processes in the water cycle, but favors forest cover (+0.9%) instead of grassland (-0.6%) (Fig. 4.2.5). For the mid-Holocene, the configuration of orbital parameters results in stronger seasonal amplitudes of solar radiation. After winter periods, when solar radiation increases, a land to ocean temperature contrast evolves, caused by the thermal inertia of the ocean relative to the land surface. The land/ocean temperature gradient favors moisture transport towards inland, as seen in the African monsoon for instance. This mechanism is intensified by the setting of mid-Holocene orbital parameters, i.e. when summer solstice was closer to perihelion of the Earth orbit. In general this can be seen in a net water vapor transport from ocean towards land compared to ctl_sol (Table 4.1). An intensification of the African wind system leads to increased precipitation in the Sahel zone favoring the establishment of forest cover. Also in high northern latitudes, where sea-ice cover is reduced due to warmer temperatures, increased open waters contribute to raised evaporation over the ocean (e.g. Barents Sea). Therefore, the global forest cover can increase and expand in areas formerly characterized by tundra (C3 grasses and cold shrubs) or desert. The resulted change of terrestrial vegetation cover leads to higher water storage capacities in soils (Table 4.1), typically found under forests and C4 grasses and thus, as a result, soils moisten. In consequence of extended forest cover and higher temperatures, which is amplified by the effect of higher water storage in soils (Table 4.1), the land evaporation (and transpiration) and precipitation increases significantly. In HOL_sol the additional atmospheric water transport from ocean to land together with land precipitation is not fully compensated by evaporation, closing the hydrological cycle via elevated drainage and land surface runoff towards the ocean (Table 4.1).

In a glacial climate regime like LGM, with significantly colder surface temperatures than Pre-industrial (-7.03 C), land evaporation and net water transport from ocean towards land is reduced. All forest PFTs and C4 grasses retreat due to unfavorable climate conditions and are replaced by shrubs and grassland reducing evapotranspiration. The synergistic effect of a cold, dry climate and subsequent soil degradation leads to lower soil water storage capacities (-7.05 cm) resulting in decreased soil wetness (-4.5 cm) and increased surface runoff ($+2.62\ \mathrm{kg\,m^{-2}\,yr^{-1}}$). However, LGM_sol is characterized by higher soil water storage capacity and soil water content compared to PI_sol. This can be explained by the sea-level drop, which exposes ocean to land surface grid points, especially in shelf areas of the Arctic Ocean and the Indonesian Archipelago. Climate conditions and additional vegetation cover in low latitudes favor soil formation processes in the exposed ocean grid points, therefore anomalies of

maximum field water capacities (Fig. 4.2.7) in the tropics exhibit highest anomalies compared to high latitude grid cells (Fig. 4.2.8). In consequence the overall decrease of maximum water storage capacities in soils (-8.76 cm) is overcompensated by the additional land surface grid points leading to wetter soils (+3.03 cm).

Heat balance and surface air temperatures

The global mean of total incoming radiation for the mid-Holocene simulation is slightly reduced compared to the pre-industrial control run (-0.14 $W\,m^{-2}$). The configuration of orbital parameters results in a shift of incoming solar radiation from the tropics towards high latitudes. In consequence of nonlinearities in the climate system, feedback mechanisms acting especially in high latitudes, HOL_sol gets comparably warmer (+0.34°C) than CTL_sol. More shortwave radiation (-2.88 $W\,m^{-2}$) at the surface is transferred to longwave radiation (+2.49 $W\,m^{-2}$) by a darkening in land surface albedo, without consideration of the ice-sheets of Greenland and Antarctica, which results in a warming of the mid-Holocene simulation. This is partly compensated by the transfer of sensible energy into latent energy via latent heat flux (+2.06 $W\,m^{-2}$) which can lead to regional cooling, where the latent heat flux exceeds the sensible heat flux, e.g. in the southern Sahel region. The synergistic effect of physical soil properties and climate amplifies the warming during the mid-Holocene Epoch of about 70% (+0.24°C) in our model simulations especially at the land surface (+0.44°C). The increased soil water storage capacities at the Sahel region and high northern latitudes increase the soil water content, fostering evaporation (see Sect. 4.2.4) and cooling due to stronger latent heat transfer (+0.29 $W\,m^{-2}$). Nevertheless, the sensible heat flux shows a higher transfer of energy (+0.71 $W\,m^{-2}$) to temperature via changes of soil albedo which overcompensate latent heat transfer. Affected regions can be found in transitional climate regimes characterized by positive changes in vegetation cover with bare soil (Fig. 4.2.5) like Northern Siberia and the northern Sahel zone. In the north-polar region an increase in forest cover as seen in the anomaly plot (Fig. 4.2.5a) and the synergy of soil processes (Fig. 4.2.5b) leads to a shading of the snow cover beneath the forest canopy, a darkening of the albedo resulting in higher sensible heat flux at the surface. Including physical soil properties tend to amplify this process by earlier spring snow melt due to the surrounding of darker soils with an anomalous increase in spring temperatures as a consequence. This mechanism acts in concert with a delayed expansion of sea-ice cover during autumn (initiated by the stronger insolation at the poles and enlarged seasonal insolation contrast of orbital parameter setting) which further decreases the planetary albedo. With the retreat of sea-ice cover the insulation effect between atmosphere and ocean disappears and the heat flux increases. Both mechanisms tend to enlarge the growing season of terrestrial vegetation. The model simulation of the Last Glacial Maximum (LGM_sol) is characterized by an increased snow cover, a retreat of tropical forest cover (-59% compared to PI_sol) and an expansion of the Sahara desert, a southward shift of the boreal tree line to ca. 58°N and a replacement from tundra to polar desert in North Siberia (Fig. 4.2.6) which raise land surface albedo. The synergistic effect of a glacial climate and adaptable geophysical soil parameters exhibit an amplified decrease in forest cover (-2.6%) substituted by grassland (+2.7%) and expansion of desert regions (+1.4%). This leads to a brightening of the land surface (Fig. 4.2.7b) and increased backscattering of shortwave radiation (+7.09 $W\,m^{-2}$) supported by changes of geophysical soil properties (+2.52 $W\,m^{-2}$). In consequence of the cooling and the decrease of terrestrial

vegetation, evapotranspiration is reduced. Therefore, the latent heat flux is strongly reduced (-4.15 $W\,m^{-2}$) corroborated by the effect of degraded water holding field capacities in soils (-1 $W\,m^{-2}$). In a zonal belt between 50-65°N over Asia, the water holding field capacities in soils and tree cover are strongly decreased. The migration of forests exposes brighter and more degraded soils compared to PI_ctl and thus the sensible heat flux is reduced. If the increase of land surface area due to the drop of sea-level is taken into account, the effect of latent and sensible heat transfer is attenuated or even reversed (+4.4 $W\,m^{-2}$). However, compared to evaporation over substituted open ocean waters (-656 $kg\,m^{-2}\,yr^{-1}$), this effect is negligible.

4.3 Discussion

4.3.1 Dynamic soil feedback for mid-Holocene climate

Considering the dynamic adaptation of physical soil characteristics, our results indicate a warmer mid-Holocene climate than shown in most previous modeling studies with dynamic vegetation (Gallimore et al., 2005; Braconnot et al., 2007; Otto et al., 2009a,b). The increase of global surface air temperature of +0.34°C in our simulation is comparable with a mean warming of +0.36°C in the study of O'ishi and Abe-Ouchi (2011) using a GCM with slab ocean-atmosphere-vegetation dynamics. They state that most of the modeled global warming is derived from vegetation dynamics (+0.23°C), whereas warming in our simulations is derived from soil mechanisms with feedbacks to vegetation, sea-ice and atmosphere (+0.24°C), compared to our standard simulations without soil scheme (HOL_CTL-PI_CTL: +0.10°C). The change in solar forcing results in a warming of the high northern latitudes amplified through the interaction of the sea-ice albedo feedback (late autumn which continues into winter time), snow-vegetation feedback (winter period) and vegetation-soil feedback (throughout the year). Especially the start of snow-melt happens earlier on soils with lower albedo, which compensates for the effect of low spring insolation during mid-Holocene. For the mean mid-Holocene climate north of 60°N, Sundqvist et al. (2010a,b) reconstruct 2°C warmer temperatures than Pre-industrial, with seasonal variations of +1°C in summer and +1.7°C in winter. They conclude that year-round warming in the high northern latitudes is mainly due to warmer spring and/or autumn temperatures. Our model studies show amplified temperature changes in high latitudes (>60°N), which leads to +1.15°C warming without—and to +1.83°C with the soil scheme. The highest seasonal warming happens in winter (+2.37°C) and autumn (+2.35°C) consistent with increased solar radiation but not in agreement with +1°C winter warming as stated by Sundqvist et al. (2010a,b). However, the multi-proxy approach might be biased by an uneven clumping of proxy data in north Scandinavia and disproportionately high amount of terrestrial records compared to marine proxy archives (Sundqvist et al., 2010a,b; Otto et al., 2011) . Nevertheless, winter warming in high latitudes seems to be essential for northward migration of trees and expansion of temperate deciduous forests in Europe by reducing severity of coldest month temperature (Prentice et al., 2000). Otto et al. (2011) faced the problem of early spring warming with an atmosphere-vegetation model study, in which they tested the climate sensitivity of increased snow masking by forest canopy. The atmosphere-vegetation feedback alone revealed a spring warming of 0.34°C by an expansion in forest cover of 13%, which is still not sufficient to explain the mismatch between model and proxy data (Otto et al., 2011). Although insolation during spring was reduced, HOL_sol

warms about +0.98°C, strongly pushed by the integrated soil feedback (+0.72°C), which also contributes to warming through all seasons. Our model study simulates significant increase of forest cover of +11% in high latitudes (60-90°N) and stable forest cover (+0.7%) in mid-latitudes (35-60°N) which is in line with pollen records published by Prentice et al. (2000). Both, Wohlfahrt et al. (2004) and Gallimore et al. (2005) find an increase in modeled grassland at mid-latitudes, once associated with spring warming (Wohlfahrt et al., 2004) and once with spring cooling (Gallimore et al., 2005). Mid-latitude anomalies of total water holding field capacities of soils and soil wetness are moderately increased. Although spring insolation is low, temperatures during spring are close to PI_sol (-0.07°C). The soil and vegetation feedback (Wohlfahrt et al., 2004) potentially provides a mechanism for anomalous spring warming (+0.4°C), closing the gap of model-data mismatch (Sundqvist et al., 2010a,b; Otto et al., 2011). In Europe, an increased temperature anomaly, with warming in Scandinavia and cooling in the Mediterranean region is suggested by the pollen record (Prentice et al., 2000; Bartlein et al., 2011). As a consequence of mild winters in North Europe, temperate deciduous forests expand in expense of boreal conifers (Prentice et al., 2000). Our model simulates mid-Holocene warming in North Europe, which is amplified through changes in soil albedo and interaction with sea-ice retreat in the Barents Sea. However, the model simulation does not constitute an improvement compared to other simulations which fail to simulate the cooling in the circum-Mediterranean region (Braconnot et al., 2007; Bartlein et al., 2011). A mid-Holocene cooling in the eastern Mediterranean region as e.g. seen in proxy data (Rimbu et al., 2003, and references therein), is captured in some models showing a tendency for a positive phase of AO/NAO during this time (Lorenz and Lohmann, 2004; Felis et al., 2004). In the African continent the pollen data suggests an intrusion of xerophytic scrubs and a northward shift of the Savannah into the Sahara (ca. 20°N, Prentice et al., 2000) enabled by increased precipitation (+200-500 mm yr^{-1}, Bartlein et al., 2011). Due to the Sahara desert soil parametrization pedogenesis does not happen further north than 20°N and 24°N latitude at the Arabian Peninsula, respectively. The strongest change of soils characteristics is localized along a zonal band ca. 13–17°N where precipitation increases by ca. 200–600 mm yr^{-1}. Due to changes in physical soil characteristics, precipitation anomalies additionally rise about 10–30% in the Sahel, and even >40% at the Arabian Peninsula. However, this is still not sufficient to feed the catchment area of paleolakes in south east Africa ca. 20°N (Hoelzmann et al., 2000; Vamborg et al., 2011). Apart from local water recycling and delayed water retention of soil processes the inclusion of wetlands and increased lake surface area might increase convective precipitation (Broström et al., 1998; Krinner et al., 2012). Further north the model climate simulation shows the evolution of grassland parallel to reduced desert appearance congruent to the records of Prentice et al. (2000). The soil moisture feedback in monsoonal regions can be twofold. On one hand high soil moisture and thus large evaporation enhance precipitation and local water recycling. On the other hand, evaporative cooling reduces the land/ocean thermal gradient dampening moisture convergence over land. Douville et al. (2001), for instance, conducted soil moisture sensitivity studies in an AGCM for the Asian and African monsoon regions. In their studies of locally increased soil moisture, the evaporative cooling effect dominates in the Indian continent resulting in a weaker monsoonal wind flow, whereas soil moisture influences precipitation in sub-Saharan Africa (Douville et al., 2001), generating a positive feedback mechanism. As shown in the present work, mid-Holocene precipitation anomalies in typical monsoon areas are increased. In our approach, soil moisture and water holding field capacity of soils in these

regions increase, parallel with a darkening of soils which compensate for potential negative feedbacks of decreased moisture convergence. In the context of Holocene African wind system evolution, several mechanisms have been proposed for a zonal northward shift of the African rain belt and Indian monsoon (Wanner et al., 2008). Here, we can confirm that the soil feedback induces more forest cover and reduces desert appearance. As a consequence of the soil treatment, water holding field capacity and thus soil moisture increases in the Sahel zone reinforcing evaporation, precipitation and cloud cover. At 13°N latitude (and north India) lowered land albedo strengthens sensible heat flux in concurrence with increased soil water storage capacity leading to higher evapotranspiration, cloud cover and precipitation (soil moisture precipitation feedback) resulting insignificant surface temperature anomaly. Further north, at 17°N latitude the darkening of land surface by soil albedo change dominates the anomalous warming in south Sahara resulting in an elevated latitudinal temperature gradient. In model simulations of the Eemian, Herold and Lohmann (2009) reveal a mechanism in which the latitudinal temperature difference above North Africa favors a stronger zonal pressure gradient. Along the gradient, zonal wind fields establish carrying Atlantic moisture inland. In agreement with simulations of the mid-Holocene (Braconnot et al., 2007), Herold and Lohmann (2009) conclude that this mechanism dominate during interglacials, when the Earth's orbit favors increased seasonality and Northern Hemisphere insolation. In response to migration of vegetation, soil development might support this mechanism, advecting more Atlantic moisture towards the African continent. Kutzbach et al. (1996) prescribe effects of vegetation expansion, change in soil color and texture for mid-Holocene in an AGCM. Their results show a strong positive feedback of soil characteristics reinforcing the monsoon, higher than changes in vegetation. Levis et al. (2004) utilize an AOGCM with dynamic vegetation and apply changes in soil albedo and soil texture. They conclude that the West African monsoon is more sensitive to changes in land surface albedo rather than to changes of evapotranspiration. However, in their model approach a wettening of soils leads to halve of the respective albedo exhibiting a strong feedback in their model approach. In a study using a vegetation module asynchronously coupled to a GCM, Gallimore et al. (2005) find a strong anomalous shift in forest cover increasing (+18%) between 60-90°N and decreasing (-12%) between 35-60°N. The expansion of grassland at the expense of forest mainly occurs in Eurasia which is affected by aridity (less precipitation and increased evapotranspiration) and lowered soil water content driven by enhanced summer solar radiation (Gallimore et al., 2005).

4.3.2 Dynamic soil feedback for the Last Glacial Maximum

The general picture of the model-data comparison fits for the glacial climate as it reflects year-round cooling and continental drying with reduced precipitation (Bartlein et al., 2011). The soils reduce their ability to hold water against gravity, which decreases retention time and evaporation, and the land surface appear brighter due to elevated soil albedo. In comparison to coupled atmosphere-ocean GCM studies of PMIP2, the global cooling of surface air temperatures shown here (-7,03°C MAT) exceeds the cooling range of former studies (-3 to -6°C, Braconnot et al., 2007, 2012) and cooling estimates based on proxy data (-4°C; Annan and Hargreaves, 2013). As an example, modeled cooling in the tropical ocean is overestimated compared to the MARGO sea surface temperature compilation (MARGO Project members, Waelbroeck et al., 2009). However, PMIP2 studies do not take into account further negative

radiative forcings (e.g. dust content; Jansen et al., 2007) which potentially amplify glacial cooling. Braconnot et al. (2012) associate part of the spread of cooling among the models with changes in surface albedo, for instance. In future climate scenarios, Hall et al. (2008) show that high values of prescribed snow albedo reduce the accumulation of snow during winter resulting in lower soil moisture in the subsequent summer, which reduces evaporation rates and hence latent heat transfer. Further, Otto et al. (2011) test the sensitivity of modifying land surface albedo by varying the parametrized shading of forest canopy on snow. An increase of masking snow on the ground by forest canopy significantly increases spring warming (+0.34°C north of 60°N latitude) in mid-Holocene simulations (Otto et al., 2011). Further, values of snow albedo in models of PMIP2 deviate and show different magnitude of cooling clearly seen above prescribed LGM ice sheets (Braconnot et al., 2012). Braconnot et al. (2012) conclude that the insufficient representation of paleo monsoon in models questions the performance of present state of the art land surface schemes with dynamic vegetation integrated in AOGCMs in representing future land cover change. As the pedosphere is closely connected to terrestrial vegetation, e.g. plant available moisture, prescribed soil characteristics might impede vegetation to migrate across present-day climate zones. The soil-feedback leads to further decreasing of precipitation, evaporation and surface temperatures in global mean. This leads to a broad expansion of desert areas in Eurasia, North Africa and north Polar Regions to the expense of grass cover. The expansion of polar desert in the Siberian sector in expense of C3-grasses leads to degradation and brightening of soils reinforcing cooling which shifts the northern tree line further south, which is in agreement with reconstructions (Prentice et al., 2000). In North America forests in close vicinity to the Laurentide ice sheet disappear in response to the regional cooling effect. South east North America exhibits exceptional high precipitation caused by a southward deflection of the jet stream around the ice sheet which fosters tree growth there consistent with the terrestrial pollen record (Bartlein et al., 2011). For Europe models basically fail to reproduce extreme cooling of ca. 20°C in coldest month which was reconstructed by pollen data (Bartlein et al., 2011; Braconnot et al., 2012). In Western Europe, the model produces a cooling of about 18°C, which declines towards Africa. The model with interactive soil scheme accounts for a surplus of cooling during the coldest month, which is in the range of global mean cooling due to the soil treatment (-1°C). Kageyama et al. (2006) find an increased standard variation of coldest-month temperature in the PMIP2 models for Western Europe, up to three times higher than the control run. They argue that higher inter-annual variability of extreme cold events during the LGM might have biased the proxy record towards colder winter temperature reconstructions. Our model approach shows a similar increase of coldest-month temperature variability like in the PMIP2 models, only with minor changes due to the soil treatment. Most of the variability in our model as well as in the PMIP2 models is derived from changes in sea-ice cover in the North Atlantic impacting European climate (Kageyama et al., 2006). In low latitudes, tropical rainforest exhibits a strong contraction (-59% in our simulation) caused by diminished evaporation, reduced water storage capacities in the atmosphere and hence less advective ocean to land moisture transport. Here, the water holding field capacities and soil moisture are decreased, which in consequence fasten water retention time and impede the uptake of plant available water. This is consistent with reconstructions of the rainforest, based on pollen, geochemical, and stable oxygen isotope data, indicating that Brazil rainforest decreased by 54% and in Africa tropical rainforest decreased by about 84%, limited to viable conditions in the Congo Basin (Anhuf et al., 2006). In the Southern Hemisphere sea-ice expansion towards

the equator leads to cooling and dry conditions as shown in the precipitation anomalies (Fig. 4.2.3). The latitudinal boundary at ca. 45°S exhibits a transition from relative wet to dry conditions towards the Antarctica, as indicated by PMIP2 model simulations, which might have isolated the southern circumpolar region (Rojas et al., 2009). The general cooling in the tropical latitudes weakens the Hadley-cells and trade winds expressed by reduced convection, evaporation and precipitation in the Innertropical Convergence Zone (ITCZ) and less advective moisture transport by the weakened subtropical anticyclones. This results in an increased precipitation anomaly at the horse latitudes, with higher moisture transport towards land. The soil feedback leads to an additional cooling and weakening of the Haley cells, as seen in positive precipitation anomalies caused by weakened South Indian, South Atlantic and South Pacific anticyclones. Evidence for colder and wetter conditions along the Southern Westerlies have been found in marine sediment cores close to the western margin of south-western Africa and subtropical South America (e.g. Stuut and Lamy, 2004) and ancient lake level stands in Bolivia (e.g. Baker et al., 2001). In general grain size distributions in both sediment cores of Stuut and Lamy (2004) reflect a trend towards lower humidity from the last glacial towards Holocene, which is in agreement with both of our time-slice experiments. The modeled vegetation responds to the positive glacial precipitation anomaly with higher occurrence of boreal forest. This is fostered by local water recycling associated with increased water storage capacities of soils in South Africa and South Australia. As a result the soil impact supports the development of boreal forests. Further the compilation of terrestrial pollen records of Bartlein et al. (2011) confirms increased plant available moisture for the South African region. Jiang (2008) utilized an atmospheric GCM asynchronously coupled to the BIOME3 terrestrial vegetation equilibrium model and changed soil characteristics iteratively, similar to our approach. However, only if the dominant vegetation type in a grid cell has changed after iteration, soil characteristics were adapted as well. Instead we use the integrative mean of soil characteristics weighted on plant functional types per grid cell. Forced by LGM boundary conditions, the model of Jiang (2008) shows an additional decrease of surface air temperature of -0.05°C globally, and high latitude (60-90°N) cooling over ice-free continental areas of -0.42°C. The additional cooling presented in Jiang (2008) is in agreement with our studies, but it does not represent the magnitude of our findings. Some discrepancies might arise from differences in the setup of glacial boundary conditions (fixed SST fields as per CLIMAP, 1981; atmospheric CO_2 concentration of 200 ppmv versus 185 ppmv as used in our approach) or differences of prescribed soil characteristics attributed to vegetation types. Further, Jiang (2008) applies an atmospheric GCM which cannot consider potential ocean-atmosphere-sea interactions with terrestrial vegetation and soil.

4.4 Conclusions

In this study, we developed a basic soil scheme which considers changes in physical soil characteristics with respect to computed canopy. Therefore changes of soil properties are tightly linked to vegetation dynamics and thus climate. Currently, some aspects of soil characteristics have been considered in GCMs, dynamically computed albedo of foliage for instance (Vamborg et al., 2011), but hitherto the integrated impact of soil formation with respect to soil albedo and water holding field capacities is untouched. The scheme is asynchronously coupled to an AOGCM with dynamical vegetation and tested for time slices of the Last Glacial Maximum and mid-Holocene. We show that the soil impact amplifies the

climate signal for both, warmer and colder than pre-industrial simulations towards stronger extremes on a regional scale with global consequences. The warm mid-Holocene climate is predominantly forced by a redistribution of solar radiation without changes in the total energy budget of incoming radiation, which claims a strong feedback mechanism in the climate system. So far, most of the GCMs cannot reproduce the amplitude of warming as suggested by the geological remnants, raising the question of lacking or impeded feedbacks in present state of the art GCMs (O'ishi and Abe-Ouchi, 2011; Hargreaves et al., 2013; Lohmann et al., 2012). The soil feedback shown in the mid-Holocene simulation might serve as part of an explanation for these discrepancies. In contrast the simulation with interactive soil treatment of the Last Glacial Maximum exhibits a global cooling beyond the range of the PMIP2 model simulations (Braconnot et al., 2007, 2012). On a regional scale the soil feedback improves the model performance getting closer to terrestrial proxies (increase in the Sahara and polar desert area; decrease of tropical forests; extra cooling in north Siberia; increase in boreal forests along 30°S latitude; southward shift of the northern taiga/tundra transition; Prentice et al., 2000; Anhuf et al., 2006; Bartlein et al., 2011) or does not significantly contribute to a climate shift (e.g. Europe; Kageyama et al., 2006). So far we have not focused on vegetation and soil dynamics with respect to the global carbon budget. Apart from prescribed boundary conditions, the soil impact (e.g. water holding field capacity) might influence the uptake of CO_2 through coupled stomata transpiration by shifting the water stress regime. Further changes in water resources and soil temperature (through changes in soil albedo and water holding field capacities) might alter carbon sequestration and formation of soil carbon stocks, as happened throughout the last deglaciation (Adams et al., 1990; Brovkin et al., 2002; Ciais et al., 2012). The nature of the soil scheme, similar to equilibrium terrestrial vegetation models (e.g. Prentice et al., 1992), does not account for soil evolution over time. Therefore it simulates a final solution of physical soil characteristics in equilibrium with vegetation and climate. For instance, the final state of the soil in the pre-industrial control run and mid-Holocene simulation leads to an anomalous warming, forest increase and desert decline in north eastern Canada, where the Laurentide ice-sheet retreat exposes juvenile soils during the last deglaciation, starting carbon sequestration, which is still an ongoing process of present soil formation (Harden et al., 1992). However, time-slice experiments in general are designed to show an equilibrated climate state in the GCMs. Nevertheless future transient GCM studies utilizing dynamic soil schemes have to implement a time dependent function for nonlinear progressive and regressive soil development, acting on broad timescales (Johnson et al., 1990; Hoosbeek and Bryant, 1992). As shown in Claussen et al. (2006), only the fully integrated interaction of atmosphere, ocean and vegetation dynamics provided the strongest amplitude of climate variation by precession forcing. In addition and analogy to vegetation dynamics (Claussen, 2009), we also show that the vegetation-soil feedback might reinforce the climate response to orbital forcing during the late Quaternary. On tectonic timescales the model reproduction of a reduced meridional global temperature gradient with temperate climate in high latitudes has been identified as a key issue (e.g. Jenkyns et al., 2004; Moran et al., 2006; Huber and Caballero, 2011; Hubberten et al., 2004; Knorr et al., 2011; Krapp and Jungclaus, 2011; Salzmann et al., in revision). The introduction of dynamic soil feedbacks in climate models might be a pivotal aspect of climate sensitivity and potentially provides a solution for the equable climate enigma.

Chapter 5

Glacial shortcut of Arctic sea-ice transport

5.1 The isolated glacial Arctic Ocean

The nature of the Arctic sea-ice cover during late Pleistocene glaciations is still debated, ranging from a perennial sea-ice cover to that of a near kilometer thick ice shelf covering the entire basin that would essentially halt ice drift (e.g. Jakobsson et al., 2010, and publications referenced therein; Grosswald and Hughes, 2008). Recently published stratigraphic data at the Northwind Ridge close to Chukchi margin (Polyak et al., 2007) show some evidence for ice-grounding shallower than 1000 m water depth during the Last Glacial Maximum (LGM) 23–19 thousand years before present (kyr BP). Most of geophysical and geological evidence is thought to have formed in Marine Isotope Stage (MIS) 6 (ca. 185–132 kyr BP) and was retrieved from various sites, including ice streamlines at Yermak Plateau near Fram Strait, Morris Jessup Rise north of Greenland, at the Lomonosov Ridge close to the North Pole, Mendeleev Ridge, Northwind Ridge and Chukchi Plateau and Alaska Beaufort Margin. These streamlines do not support the idea of a shelf ice cover of Antarctic type during the LGM (Jakobsson et al., 2010). However, there are still extremes of postulated glacial sea-ice drift, varying from no substantial change from today (Phillips and Grantz, 2001) to a resting ice massif with only occasional break-up north of Fram Strait (Nørgaard-Pedersen et al., 2003; Bradley and England, 2008).

In the central Arctic Ocean, LGM climate reconstructions are limited and challenging due to low sedimentation rates and bioproduction (Stein et al., 1994; Nørgaard-Pedersen et al., 1998; Stein, 2008). Polyak et al. (2004) present a sedimentary record of the Mendeleev Ridge confirming that LGM sediments poorly conserve biological remains (benthic and planktonic foraminifera) favoring the interpretation of a thick lid of pack ice or even an ice-shelf covering the western Arctic Ocean.

Along the continental margin at Fram Strait where modern North Atlantic waters are penetrating the Arctic Ocean. Nørgaard-Pedersen et al. (2003) suggest seasonal open water conditions and north of Fram Strait a glacial perennial ice cover. Bradley and England (2008) conclude that seasonal open water conditions along the coast from the northern edge of the

Barents Sea ice-sheet to the Laptev Sea shelf edge existed caused by narrow coastal boundary currents or offshore katabatic winds (Knies et al., 2000; Vogt et al., 2001). Contrary to these findings, Müller et al. (2009) propose a permanent LGM sea-ice cover based on Biomarker data at the northern Fram Strait location (Core PS2837-5; Lat 81°13'N, Lon 02°22'E).

A milestone in illuminating the LGM and providing data for numerical modeling was the first comprehensive reconstruction of global surface conditions provided by the Climate: Long range Investigation, Mapping, And Prediction (CLIMAP, 1981) project, including seasonal sea surface temperatures (SST) and extent of sea-ice. CLIMAP (1981) proposed perennial ice cover in the central Arctic Ocean and Nordic Seas implying a shutdown of the northern North Atlantic inflow and seasonal sea-ice cover in the North Atlantic down to 50°N latitude. These findings have been revised and expanded by SST reconstructions in the Atlantic sector of the GLAMAP Group (Pflaumann et al., 2003) that show a discrepancy of 8°C warmer summer temperatures in the Nordic Seas. Along the Faroe Shetland Passage, Hebbeln et al. (1994) also observed limited sea-ice expansion with seasonally open, warmer waters in the Greenland and Norwegian Seas. However, quantitative reconstructions of SST in Nordic Seas based on different proxies diverge by more than 10°C (de Vernal et al., 2006). They relate potential discrepancies among the proxies to diverse salinity tolerance, trophic levels, taphonomy and lateral advection. For example, Mg/Ca ratios indicate surface temperatures up to 10°C (Meland et al., 2005), whereas $\delta^{18}O$ values suggest less than 4°C both derived from shells of *N. pachyderma* assemblages at Nordic Seas (de Vernal et al., 2006). In light of the proxy uncertainties and different hypotheses of late Pleistocene glaciations in the Arctic, we address the glacial sea-ice and ocean circulation by a numerical model instead. For this purpose, we deploy a regional ocean/sea-ice model that has been used in recent studies (e.g. Kauker et al., 2003) and operational sea-ice cover predictions (Kauker et al., 2009), and equip it with boundary conditions that are representative of the LGM. We use this regional ocean/sea-ice model to investigate the glacial Arctic sea-ice system and propose a model- and proxy-based ice drift reconstruction for the LGM.

5.2 Geological data

The sedimentary record shown in Fig. 5.2.1 is derived from AMS^{14}C-dated box core PS1230 (Lat 78°51'N, Lon 04°46'W; 1235 m below sea level; Darby et al., 2002; Darby and Zimmerman, 2008), which is located at the center of modern sea-ice export through Fram Strait (Vinje et al., 1998).

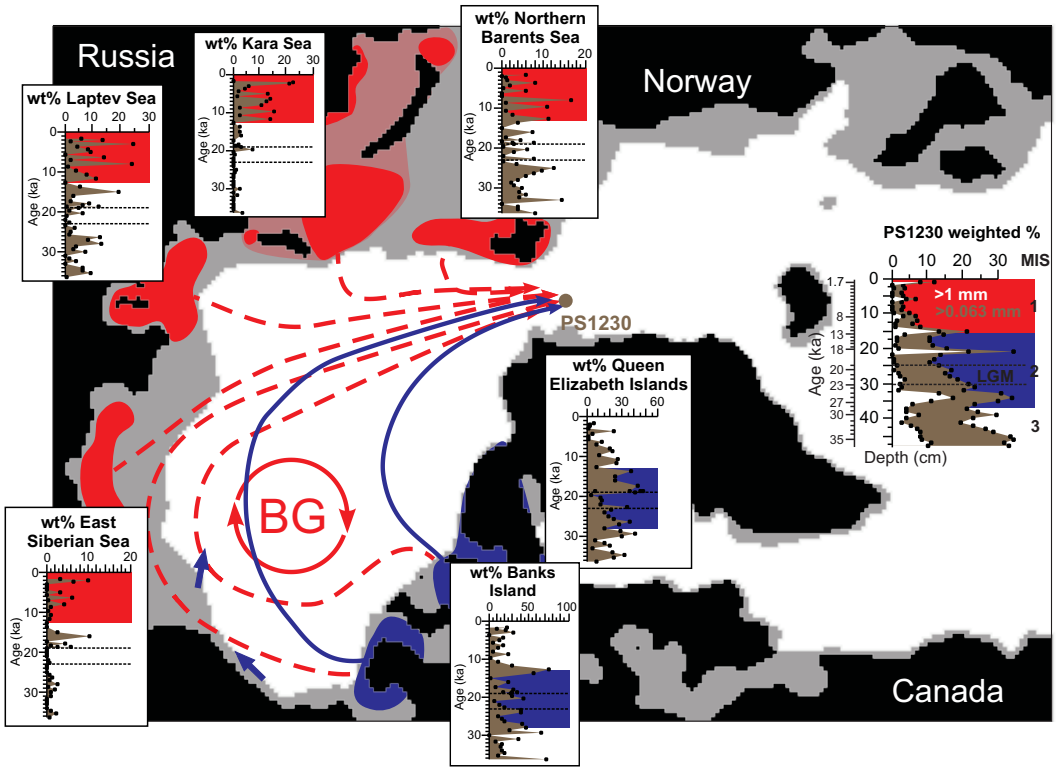

Figure 5.2.1: Reconstruction of last glacial/interglacial ice drift in the Arctic Ocean. Black land/sea-mask marks the modern and gray, the glacial boundaries of the model. Weighted proportion (wt%) of the iron oxide grains from core PS1230 (Lat 78°51'N, Long 04°46'W; 1235 m water depth) (Darby et al., 2002; Darby and Zimmerman, 2008), assigned to the individual regions of origin (blue and red areas). Solid blue lines indicate glacial, dashed red lines are interglacial ice drift (Bischof and Darby, 1997). Blue arrows indicate ice plough marks, dated to the LGM (Engels et al., 2008; Polyak et al., 2001, 2007).

Using a geochemical fingerprinting method, Darby et al. (2002) and Darby and Zimmerman (2008) are able to identify the source of individual detrital iron oxide minerals (in the 45–250 µm fraction) transported by sea-ice and/or icebergs. Geographically distinct sources of sea-ice formation and/or iceberg calving are identified by >2000 circum-Arctic compositional groups applying statistical analysis (clustering and discriminant function analysis; Darby et al., 2002). The statistical approach typically matches 50–60% of the analyzed grains per sample (ca. 100 grains), therefore a weighted percentage (wt%) is used to avoid anomalously large percentages when grain numbers are low (Darby and Zimmerman, 2008). In general, the sedimentary record shows an elevated level of coarse IRD during late MIS3 (ca. 60–27 kyr BP) and MIS2 (ca. 27–12 kyr BP) including the LGM (Fig. 5.2.1, marked in blue), whereas the Holocene signal (12–0 kyr) is dominated by fine-grained sediment (<10% coarse fraction; marked in red). The fine-grained nature of this Holocene sediment suggests sea-ice rafted debris (Pfirman et al., 1989; Reimnitz et al., 1998; Nürnberg et al., 1994; Darby et al., 2011).

For the reconstruction of glacial/interglacial ice-drift pattern (Fig. 5.2.1, solid blue and dashed red lines) the same method was applied to a transect of sediment cores bisecting the central Arctic Ocean(Bischof and Darby, 1997).

Furthermore geophysical evidence of the sea-floor along the Alaska-Beaufort margin (Engels et al., 2008) and Chukchi-Borderland (Polyak et al., 2001, 2007) show glaciogenic iceberg scours, which indicate grounding of large ice masses and the direction of ice drift that are used for model comparison (Fig. 5.2.1).

5.3 Results

5.3.1 Simulation of Arctic sea-ice dynamics and thermodynamics

For CTRL, mean westerlies are >4.5 $m\,s^{-1}$ in the northern North Atlantic sector and katabatic winds are localized above the Greenland ice sheet (Fig. 5.3.1). The Nordic Seas of LGMC are enclosed by katabatic winds off the eastern flank of Greenland ice sheet and the western flank of the Barents Sea ice sheet, whereas the speed of westerlies is reduced compared to CTRL. The wind speeds in LGMG compared to LGMC are larger in general and form an anomalous Icelandic Low (Fig. 5.3.1c).

In the central Arctic Ocean, a closed perennial sea-ice cover with mean thickness of 3 m is found (Fig. 5.3.2a).

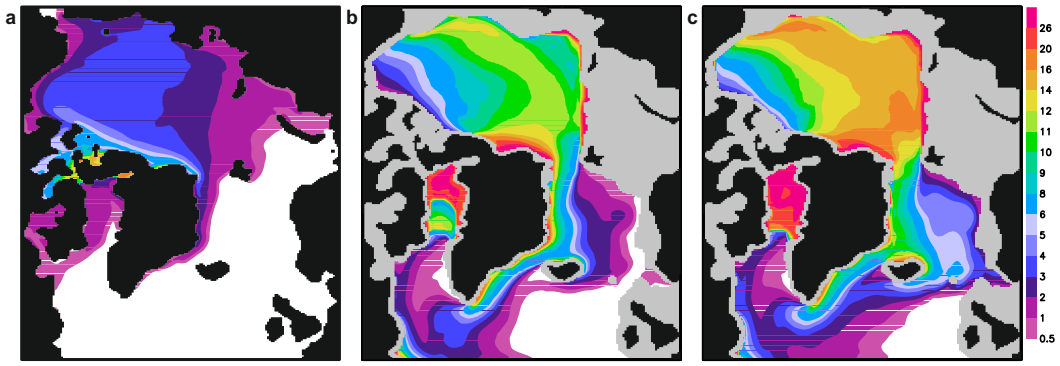

Figure 5.3.2: Mean sea-ice thickness (m) for modern and glacial conditions. (a) Present-day control run (CTRL). (b) LGMG. (c) LGMC.

Perennial ice, >8 m thick, is observed primarily in parts of the northern coast of the Canadian Archipelago and the coast of northern Greenland (Fig. 5.3.2a). The sea-ice drift follows the Beaufort Gyre and Transpolar Drift (Fig. 5.3.3a) exiting the Arctic Ocean through Fram Strait. Today's single year sea-ice, represented by present-day control run (CTRL), evolves and melts in the circum-Arctic shelf-seas and further south especially in Baffin Bay and along the East Greenland Current within a year (Fig. 5.3.4a, d). The minimum of modern sea-ice export across Fram Strait is directly linked to the minimum sea-ice extent in late summer (Fig. 5.3.4 and Fig. 5.3.5) with a dramatic drop of sea-ice velocities starting in May (9.4 $cm\,s^{-1}$) and reaching its minimum in September (2.3 $cm\,s^{-1}$) before recovering (Fig. 5.3.6).

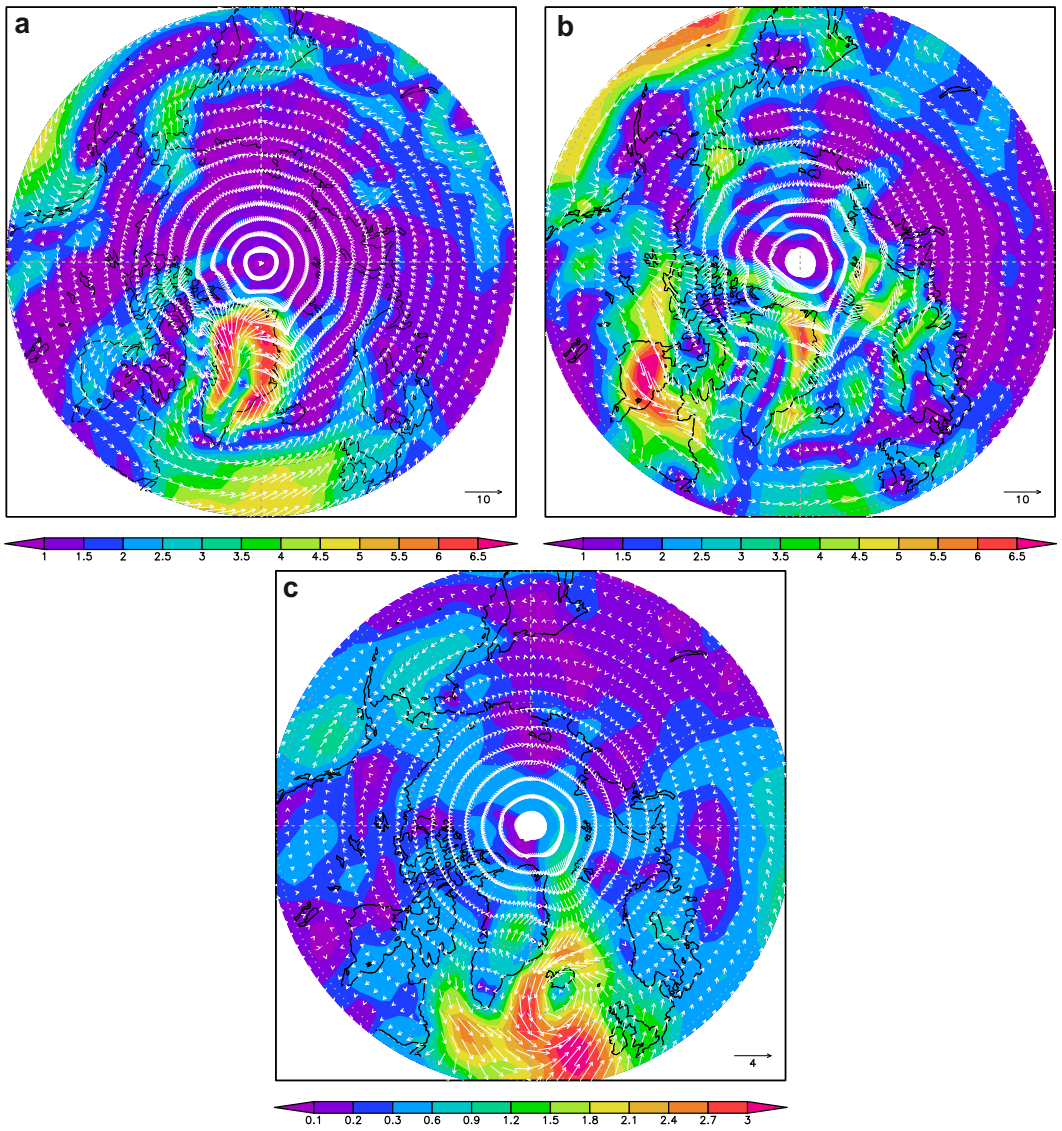

Figure 5.3.1: Atmospheric boundary forcing of wind fields 10 m above surface ($m\,s^{-1}$) for the respective model studies. (a) 30-year mean (years 1977–2007) of wind fields derived from NCAR/NCEP reanalysis data (Kalnay et al., 1996) to force present-day model run (CTRL). (b) 15-year mean of wind field data referring to the cold glacial experiment LGMC. (c) Anomaly plot of 15-year mean of wind field forcing data LGMG-LGMC.

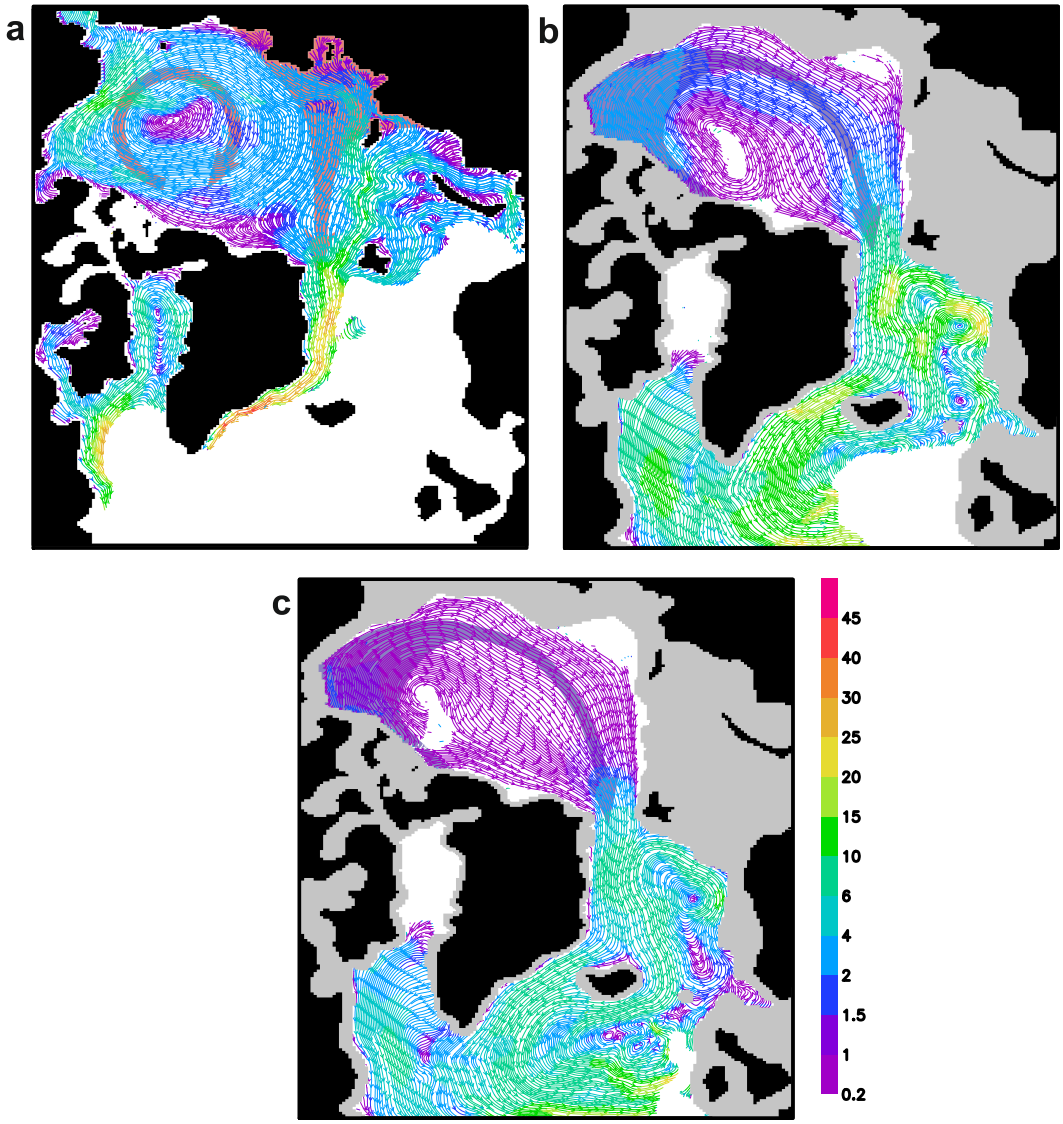

Figure 5.3.3: Streamlines of 30-yr mean sea-ice drift ($cm\,s^{-1}$) for modern and glacial conditions. (a) Model study CTRL. (b) LGMG. (c) LGMC. Not shown: sea-ice drift with a mean sea-ice concentration of $<10\%$ (in general northern North Atlantic; see Fig. 5.3.4) and a velocity of $<0.2\ cm\,s^{-1}$ (e.g. Canadian Archipelago, Baffin Bay).

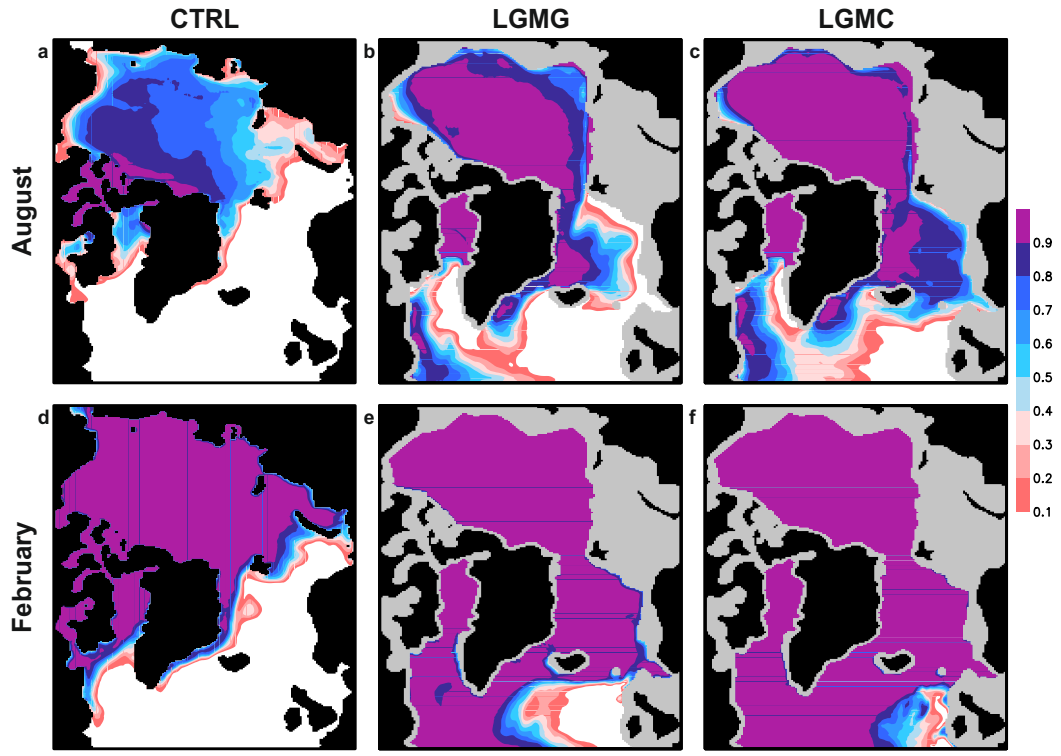

Figure 5.3.4: Mean sea-ice concentration (100%) for summer (August) in the upper row and winter (February) conditions in the lower row are displayed. (a), (d) Present-day control run CTRL. (b), (e) LGMG. (c), (f) LGMC.

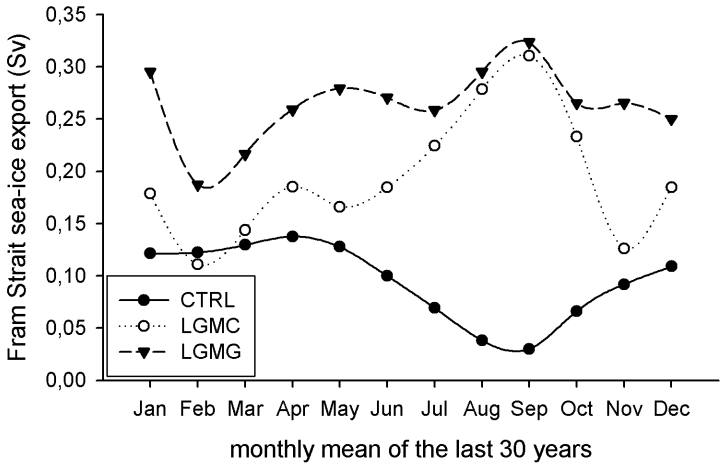

Figure 5.3.5: Seasonal cycle of mean sea-ice export (Sv = $10^6 m^3 s^{-1}$) across the Fram Strait for CTRL, LGMG and LGMC.

Present locations of sea-ice formation include the entire circum-Arctic shelves, especially the expansive, shallow marine shelf areas of the Laptev, Kara and East Siberian Seas (not shown).

In contrast, the central glacial Arctic Ocean in LGMG and LGMC is almost completely isolated from the atmosphere by a perennial sea-ice cover throughout the year (Fig. 5.3.4). Only in the Beaufort Sea, along the shelf edge of the Canadian Archipelago is sea-ice produced within open water areas (polynyas) (Fig. 5.3.4). The northern branch of Pacific westerlies, which are split by the Laurentide ice-sheet is directed towards the Beaufort Sea and Canadian Archipelago (Fig. 5.3.1). There, early stage sea-ice is pushed offshore into the Beaufort Sea and open water surfaces are conserved along the coast (Fig. 5.3.4 and Fig. 5.3.2). At the northern Barents, Kara, and Laptev Sea shelf edge enclosing the Eurasian Basin, sea-ice is stuck ($<$0.2 $cm\,s^{-1}$ sea-ice drift) along the rim and reaches the upper limit of prescribed ice thickness (Fig. 5.3.2b, c). Further north of the rim and along the Siberian shelf edge August sea-ice cover declines to $<$50% in LGMG and $<$60% in LGMC (Fig. 5.3.4b, c). This is mainly caused by ice dynamics, since surface air temperatures during summer rarely reach positive values and surface ocean waters are close to the freezing point (not shown).

A general zonal gradient of sea-ice thickness in the Nordic Seas (Fig. 5.3.2) is maintained by two flow patterns: The northward inflow of warm, salty North Atlantic waters along the Norwegian and West Spitsbergen Current in addition to katabatic winds offshore of the Barents Sea ice sheet (Fig. 5.3.1) limit sea-ice cover there (Fig. 5.3.2). The southward East Greenland Current (EGC) carries cold, relatively fresh water and sea-ice from the Arctic. Along the EGC, a permanent sea-ice cover arises and extends to the oceanic polar front, which separates polar and Arctic water masses (Fig. 5.3.4). In contrast, seasonal sea-ice production occurs in the Arctic and Atlantic waters of the Nordic Seas. In LGMG less sea-ice concentration than LGMC with seasonally open water conditions along a more pronounced North Atlantic inflow is shown in the Nordic Seas (Fig. 5.3.4b, e and Fig. 5.3.2b). Baffin

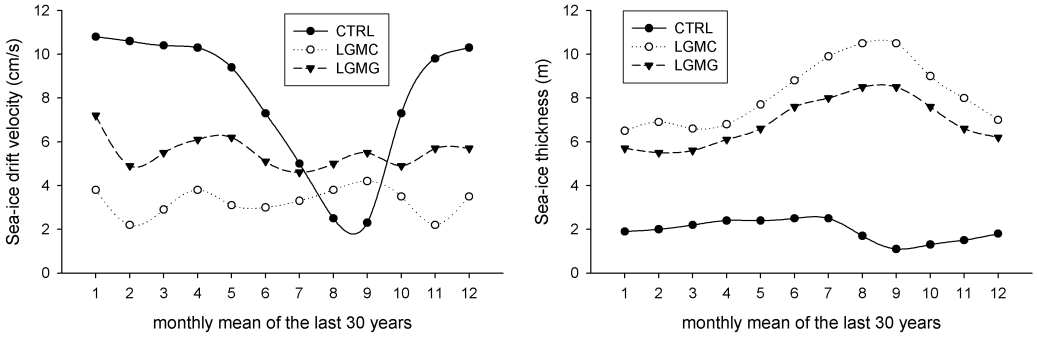

Figure 5.3.6: Monthly mean sea-ice drift velocity ($cm\,s^{-1}$; left panel) and thickness (m; right panel) across Fram Strait of CTRL, LGMC and LGMG.

Bay is characterized by a permanent, static sea-ice cover and sea-ice thickness close to the artificial limit of 30 m (Fig. 5.3.4 and Fig. 5.3.2b, c). In the southern region of Baffin Bay, the sea-ice cover destabilizes (Fig. 5.3.2b, c), and inter-annual ice-free areas emerge at the West Greenland coast of the Labrador Sea, where sea-ice is formed again. The juvenile sea-ice in the Beaufort Sea moves anti-cyclonically across the Canadian Basin and merges with a transpolar drift towards Fram Strait (Fig. 5.3.3b, c). In the glacial scenarios, the gyre of sea-ice drift is centered in the Amerasian Basin further towards the Ellesmere Island compared to CTRL. Generally the colder glacial climate scenario based on CLIMAP data shows a slow linear stream flow pattern directly towards Fram Strait. North of Ellesmere Island glacial sea-ice either gets entrapped in the anticyclonic gyre (LGMG) or takes a direct pathway along the coast of Greenland to Fram Strait (LGMC). In contrast to present-day sea-ice export, the Laptev Sea and Kara Sea shelf edge barely show offshore transport of ice. Along the Barents and Kara Sea shelf edge, sea-ice drift is comparably faster in LGMG than in LGMC (Fig. 5.3.3b, c).

5.3.2 Water mass characteristics at Fram Strait and in the central Arctic Ocean

The sea-ice drift in the glacial Arctic Basin is a result of a balance between wind stress and ocean drag (and internal ice stress). In order to understand the contribution of ocean drag, it is necessary to analyze the vertical structure of water masses. For present-day (CTRL) the mean sea surface salinity fields of the central Arctic domain are ca. 31 psu and 33 psu for LGMG and LGMC, respectively (Fig. 5.3.7a–c). The halocline in the central Arctic Ocean is situated at ca. 200 m for CTRL and ca. 80 m for the glacial sensitivity studies and a barotropic mode prevails (LGMG, LGMC, Fig. 5.3.7d–f). All presented glacial simulations show enhanced Arctic inflow of Atlantic bottom waters (ca. -3.5 $m\,s^{-1}$), colder (<-1.8°C) and saltier (>36 psu) than present-day, and the outflow of fresh Arctic waters at the water surface. At the present location of the West Spitsbergen Current glacial model studies exhibit a similar to present-day maximum speed (ca. 1 $m\,s^{-1}$) of waters entering the Arctic. Along the East Greenland Current the outflow is centered at around 200 m water depth through Fram

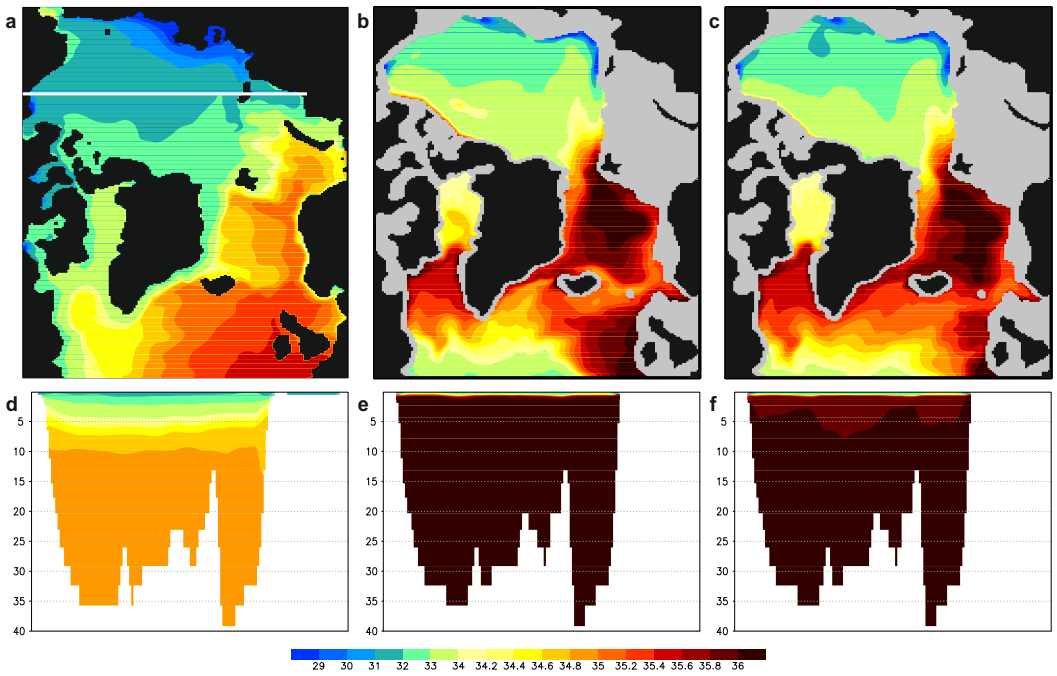

Figure 5.3.7: 30-yr mean of ocean salinity (psu) at the surface (0–20 m below sea level) and along a vertical cross section (for location see white line in a; depth in 10^2 m below sea level) for modern and glacial conditions. (a), (d) Salinity in CTRL. (b), (e) Salinity in LGMG. (c), (f) Salinity in LGMC.

Strait. Since the present-day Atlantic water inflow is shifted towards the bottom, an Arctic boundary current west of Svalbard exhale through Fram Strait (Fig. 5.3.8b–f and Fig. 5.3.9).

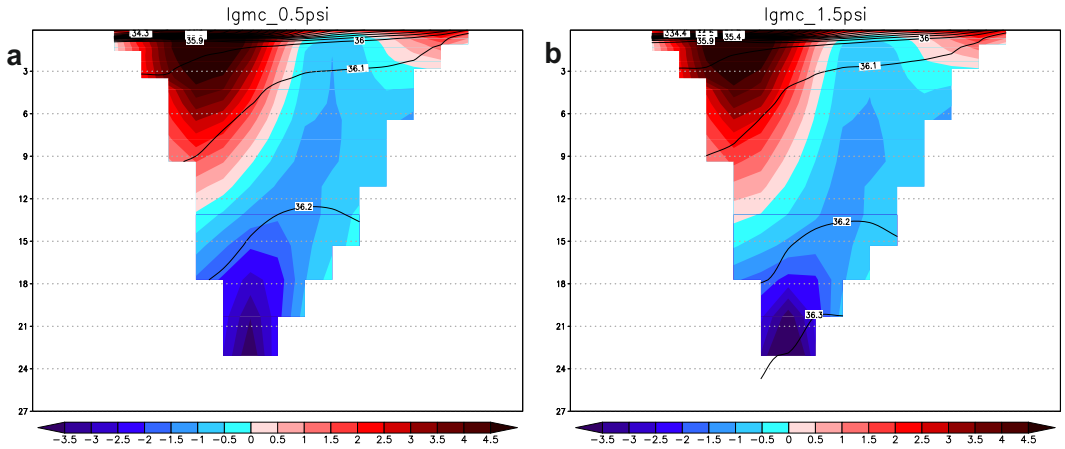

Figure 5.3.9: Ocean water characteristics of Fram Strait section (depth in units 100 m) for different model studies. Contour lines display salinity (psu), positive values colored in red show velocity ($cm\,s^{-1}$) of water outflow, negative values coloured in blue denote water flow into the Arctic Ocean. (a) lgmc_0.5psi: Glacial model setup with atmospheric boundary forcing based on CLIMAP and decrease of the barotropic streamfunction of 50% at the North Atlantic inflow of the model domain. (b) lgmc_1.5psi: Glacial model setup with atmospheric boundary forcing based on CLIMAP and decrease of the barotropic streamfunction of 150% at the North Atlantic inflow of the model domain.

The boundary current is consistent with the general ocean circulation in the central Arctic Ocean of the glacial model scenarios (not shown). For the glacial model studies the water passage through the Barents Sea is blocked by an ice sheet which potentially redirects a branch of the North Atlantic Current towards Fram Strait leading to increased water mass exchange at this location. Modulations of the Atlantic water stream function at the southern boundary of the model do not affect water properties at Fram Strait (Fig. 5.3.9). A similar effect has been reported by Kauker et al. (2005) for present-day conditions. It should be noted that deeper levels of the ocean model are not in full equilibrium. Based on LGMC we set up a sensitivity study for the surface salinity restoring term using surface salinity fields derived from the NCAR-CCSM output (Shin et al., 2003b,a). For the glacial Arctic Ocean the surface salinity anomaly of the new restoring term is higher than LGMC, but the overall large-scale effect is almost additive (Fig. 5.3.10a). The absence of relative fresh Pacific waters in the Beaufort Sea is mimicked by the surface salinity restoring term with maximum surface salinity anomalies of ca. 4 psu (Fig. 5.3.10a). An increase of salinity in the Arctic surface waters (Fig. 5.3.10a) deepens the halocline as indicated at the Fram Strait section (Fig. 5.3.8d). The exchange of water masses at Fram Strait is decreased and similar in pattern compared to other glacial model studies, but still higher than present-day. Higher surface salinity can also impact the formation of sea-ice and the quantity of sea-ice transport through Fram Strait but does not affect the overall results presented in this study (Fig. 5.3.10b, c).

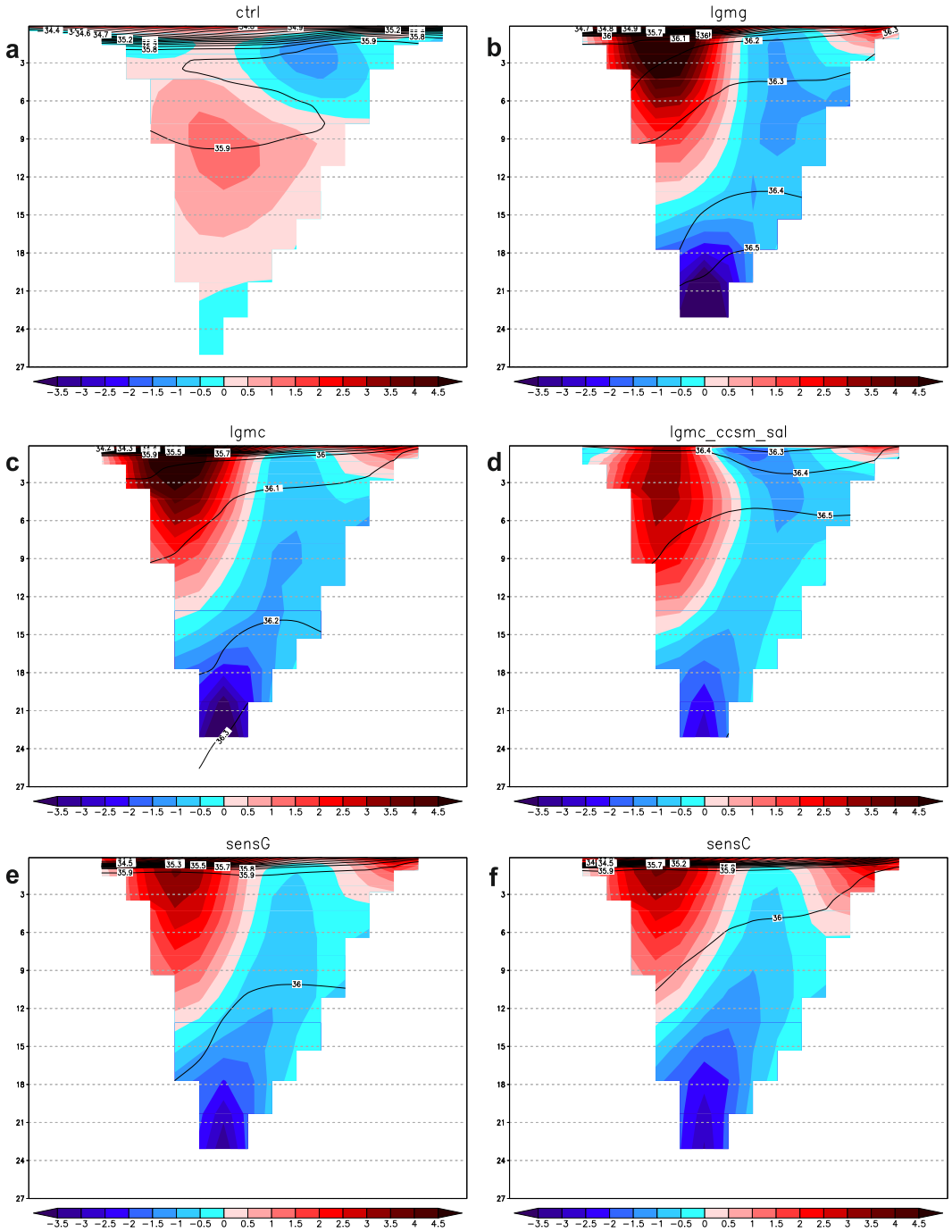

Figure 5.3.8: Ocean water characteristics of Fram Strait section (depth in units 100 m) for different model studies. Contour lines display salinity (psu), positive values colored in red show velocity (cm s^{-1}) of water outflow, negative values coloured in blue denote water flow into the Arctic Ocean. (a) ctrl: Present-day model setup. (b) lgmg: Glacial model setup with atmospheric boundary forcing based on GLAMAP. (c) lgmc: Glacial model setup with atmospheric boundary forcing based on CLIMAP. (d) lgmc_ccsm_sal: Glacial model setup with atmospheric boundary forcing based on CLIMAP with a deep halocline in the Arctic Ocean (surface salinity restoring based on Shin et al., 2003b,a). (e) sensG: Glacial model setup with atmospheric boundary forcing based on GLAMAP using present-day wind fields. (f) sensC: Glacial model setup with atmospheric boundary forcing based on CLIMAP using present-day wind fields.

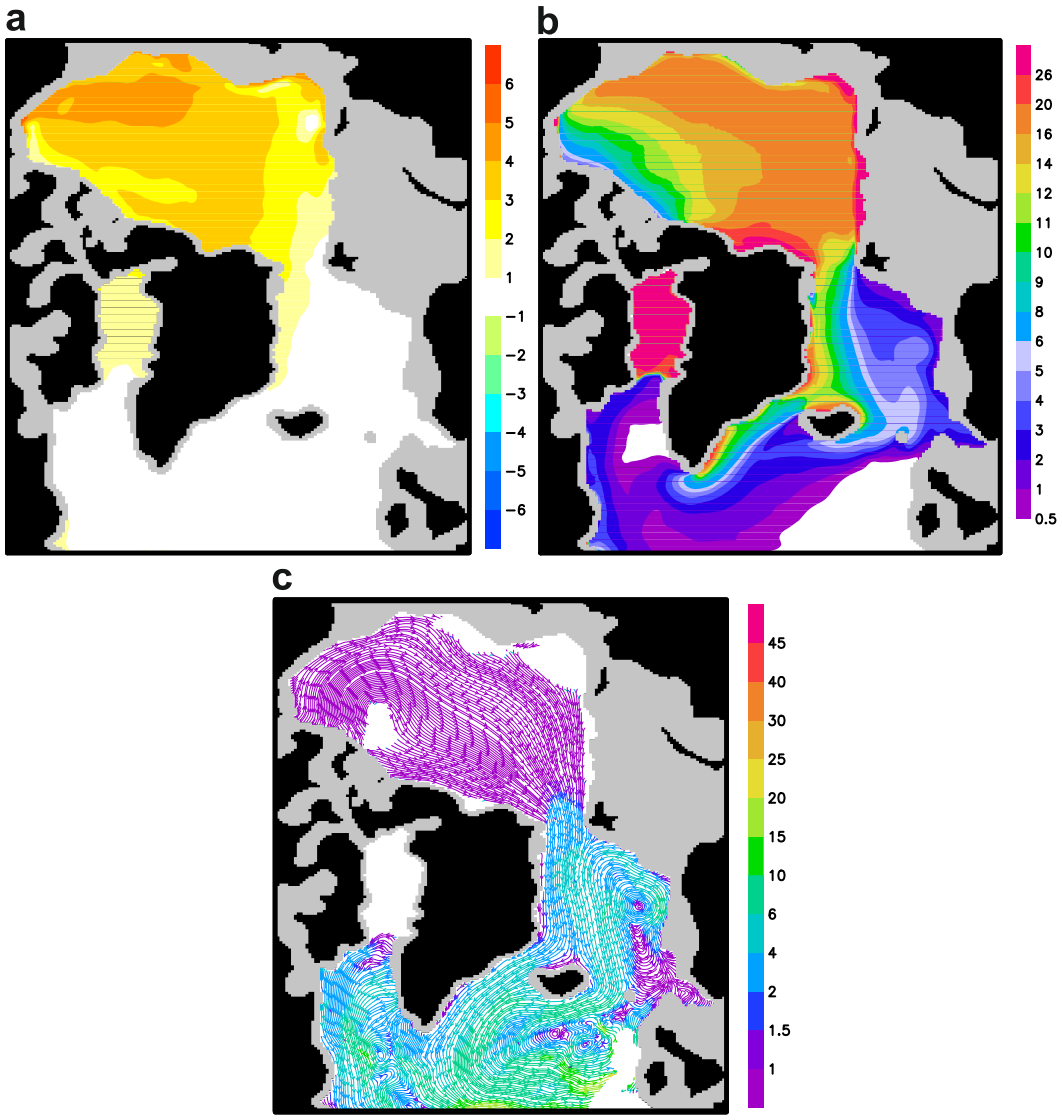

Figure 5.3.10: Sensitivity study (LGMC_sal) based on LGMC with surface salinity restoring referring to CCSM-NCAR output (Shin et al., 2003b,a). (a) Surface (0–20 m below sea level) salinity (psu) anomaly (LGMC_sal-LGMC). (b) sea-ice thickness (m) in LGMC_sal. (c) Streamlines of mean sea-ice drift ($cm\,s^{-1}$) for LGMC_sal.

5.3.3 Arctic sea-ice thickness and its export to Nordic and Labrador Seas

Along the transport path in the direction of Fram Strait, sea-ice (mostly driven by dynamical ice growth) increases its thickness between 11 and 20 m (Fig. 5.3.2b, c). At this location, temperature and wind stress of the respective model run (LGMC, LGMG) as well as ice resistance, determine the velocity of the ice drift and the sea-ice thickness. As ice drift rates in LGMC are by up to 2 $cm\,s^{-1}$ lower than in LGMG (Fig. 5.3.3b, c and Fig. 5.3.6), the residence time of Arctic sea-ice is prolonged, and up to 20 m ice thickness evolves just north of Fram Strait (Fig. 5.3.2c). The simulated sea-ice export rate through Fram Strait ($(95\pm21) \times 10^3$ $m^3\,s^{-1}$; Table 5.1) in CTRL is consistent with estimates based on observation values of a 50-yr period (1950–2000: $(91.9\pm21.1) \times 10^3$ $m^3\,s^{-1}$; Vinje, 2001). The minimum of present-day sea-ice transport during late summer (Fig. 5.3.5) is associated with a dramatic decline in summer ice-drift velocities (Fig. 5.3.6). Also present-day sea-ice thickness across Fram Strait decreases in September and recovers during winter months (Fig. 5.3.6). Seasonal sea-ice export in CTRL is dominated by changes in ice drift velocities (2.3–10.8 $cm\,s^{-1}$, Fig. 5.3.6). The sea-ice melts along the East Greenland Current and rarely reaches the Denmark Strait ($(30\pm10) \times 10^3$ $m^3\,s^{-1}$ of sea-ice export). However, up to three times more sea-ice quantity exiting through Fram Strait in the glacial model runs LGMG and LGMC (Table 5.1) is transported into the Nordic Seas (Fig. 5.3.5). The elevated glacial sea-ice flux into the Nordic Seas is caused by thicker sea-ice exiting the Fram Strait (Fig. 5.3.6). During summer the glacial ice cover destabilizes north of Fram Strait and thick sea-ice, up to 10.5 m in LGMC and 8.5 m in LGMG, is crossing the gateway (Fig. 5.3.6), causing maximum sea-ice export in September (Fig. 5.3.5). During the rest of the year glacial sea-ice export is predominantly influenced by variation of ice drift velocity (Fig. 5.3.6). The ice drifts via the East Greenland Current southwards into the ablation areas of the Labrador Sea and into the region south of Iceland (Fig. 5.3.3b, c). Here, it becomes apparent that the sea-ice export through the Denmark Strait (LGMG: $(348\pm17) \times 10^3$ $m^3\,s^{-1}$; LGMC: $(163\pm30) \times 10^3$ $m^3\,s^{-1}$; Table 5.1) reacts to changes in wind fields. Additional sea-ice, formed in the Nordic Seas, is transported in LGMG via the Denmark Strait in the direction of the Labrador Sea. This is due to enhanced cyclonic circulation over Iceland (Fig. 5.3.1c).

In LGMC_PDw and LGMG_PDw, the ocean model is forced with present-day wind fields: Sea-ice export through Fram Strait is significantly reduced (Fig. 5.3.11), the gradient of sea-ice thickness (Fig. 5.3.12a, b), and local areas of sea-ice formation in the Arctic Ocean change. Without katabatic winds off the western flank of the Fenno-Scandinavian Ice-Sheet and stronger westerlies than during LGM (Fig. 5.3.1) the zonal gradient of sea-ice cover is not simulated (Fig. 5.3.12a, b). From late summer until late spring (August until March) the southward transport of sea-ice through Faroe Shetland Passage and across Iceland Faroe Ridge is reversed (not shown). Therefore, the standard deviation, shown in Table 5.1 exceeds the mean of sea-ice export through both gateways.

Table 5.1: Mean sea-ice transport and standard deviation (10^3 $m^3 s^{-1}$) through ocean gates of the North Polar Seas and budget of the Nordic Seas are shown for each model study. Positive (negative) values denote sea-ice import (export) to Nordic Seas.

	Fram Strait	Denmark Strait	Iceland Feroe Ridge	Feroe-Shetland Passage	Δ Nordic Seas sea-ice transport
CTRL	95 ± 21	- 30 ± 10	0	0	65
LGMG	264 ± 32	- 348 ± 17	- 60 ± 14	- 3 ± 2	- 147
LGMC	194 ± 40	- 163 ± 30	- 139 ± 26	- 8 ± 9	- 116
LGMG_PDw	115 ± 38	- 153 ± 41	- 1 ± 25	6 ± 6	- 33
LGMC_PDw	88 ± 33	- 146 ± 39	- 1 ± 51	27 ± 36	- 32

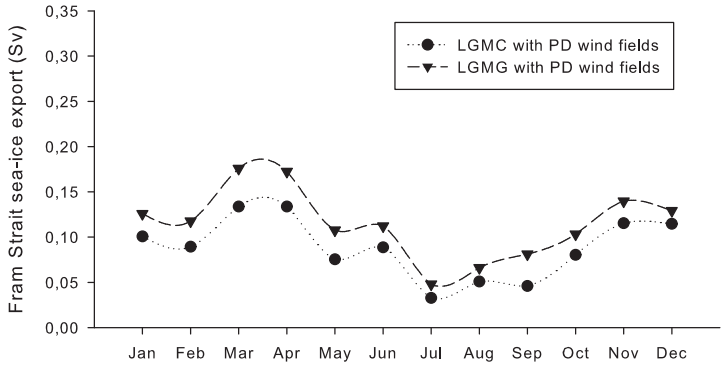

Figure 5.3.11: Monthly mean sea-ice export (Sv) across Fram Strait of LGMG and LGMC forced by present-day wind fields (Lohmann and Lorenz, 2000).

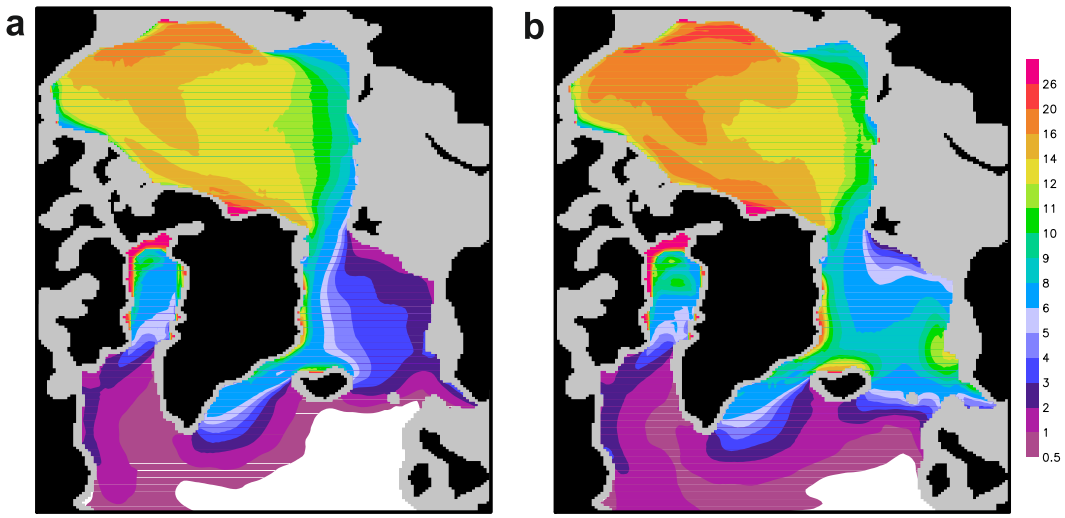

Figure 5.3.12: Sea-ice thickness (m) of glacial sensitivity studies forced by present-day wind fields. (a) Sea-ice thickness of LGMG forced by present-day wind fields (LGMG_PDw). (b) Sea-ice thickness of LGMC forced by present-day wind fields (LGMC_PDw).

5.4 Discussion

5.4.1 Model performance under glacial conditions

The ice strength parameter, formulating the rheology of sea-ice models, is tuned to fit present-day observational values. It describes the softness/hardness of sea-ice relevant for deformation processes and build-up of pressure ridges and is typically adapted to the timestep of the atmospheric forcing. The actual ice thickness is directly affected by this parameter and exhibits a linear relationship to ice strength. For sea-ice thicknesses >3 m, where sea-ice growth is primarily driven by ridging and rafting, the ice strength might be underestimated (nonlinear) leading to anomalous high pressure ridges as shown in the present-day simulation at the Canadian Arctic Archipelago (CAA) and northern Greenland (Fig. 5.3.2a). The compressive strength of sea-ice sheets increases as the ice thickens due to the fact that thick sea-ice is generally less saline as shown by material measurements (Timco and Frederking, 1990). But still, material properties of old multiyear sea-ice are poorly observed (Timco and Weeks, 2010). Consequently the glacial model simulations would suggest a rather extreme case of sea-ice thickness in the central Arctic Ocean. For elaborating the effect of ice strength parametrization sensitivity studies of varying ice strength parameter values could be setup and a regime shift in case of extreme ice thicknesses might be implemented in the model. Since these problems are beyond the scope of our work, follow-up studies of the glacial Arctic marine cryosphere and tuning of the present-day model configuration can focus on these questions.

It should be noted, that our model approach lacks potential atmosphere-ocean feedbacks (Bengtsson et al., 2004; Semenov et al., 2009), especially in the hydrological cycle and Bering Strait through flow by the restoring term (see Sect. 2.2.1). The freshwater budget and surface runoff affecting the stratification in the Arctic Ocean during LGM remains unclear and has to be defined in more detail, since our studies suggest that stratification is dominated by salinity.

Jakobsson et al. (2010) test the freshwater balance of a conceptual two-layer model of the Arctic Ocean. A decrease in freshwater supply of the upper Arctic halocline layer (as expected by a decrease in the hydrological cycle of a cold climate, see Sect. 2.2.1) results in an increase of Atlantic water influx through Fram Strait (Jakobsson et al., 2010). However, interpreted neodymium isotope data from the ACEX sediment core location, Lomonosov Ridge, suggest a longer residence time of bottom water masses during glacial intervals (Haley et al., 2008). Here we reconcile glacial water mass exchange through Fram Strait by a three dimensional ocean simulation. The glacial model scenarios show a consistent, stronger than present-day water mass exchange across Fram Strait (Fig. 5.3.8). Modifications of the Arctic freshwater balance and thus surface halocline waters do not effectively change the through flow of Fram Strait waters (Fig. 5.3.8) favoring inflow of North Atlantic waters as an operator. Experiments testing the prescribed southern boundary barotropic stream function with a glacial model setup have only minor effects on the Arctic Ocean (Fig. 5.3.9). However, Kauker et al. (2005) have shown that changes in the baroclinicity of southern boundary characteristics of the model with a present-day setup can progress into the Arctic within two years. Indeed model-data comparisons actually favor a shoaling and weakening of the glacial Atlantic Meridional Overturning Circulation (Hesse et al., 2011, and references therein), which suggests stronger baroclinicity in the North Atlantic sector.

Earlier experiments with NAOSIM show a strong effect of continental freshwater and

Pacific water through Bering Strait on the Arctic circulation (Prange and Lohmann, 2003; Lohmann et al., 2005). For the early Holocene, the model studies suggest that a gradual increase in the flux of Pacific water through Bering Strait slowly affects the polar climate by melting ice, increasing stratification, and causing an enhanced anticyclonic pattern over the Canadian Basin and the East Siberian Sea (Lohmann et al., 2005; Dyck et al., 2010). As a logical step, the effect of Arctic freshwater on the Arctic circulation during the termination of the LGM will be elaborated next.

5.4.2 Atmospheric circulation of the glacial Nordic Seas

Our results are also interesting for the validation of paleoclimate reconstructions. In the Nordic Seas, the prescribed atmospheric boundary conditions are not consistent with the simulated sea-ice cover. Neither a perennial ice cover proposed by CLIMAP (1981) nor a seasonal ice cover (GLAMAP; Pflaumann et al., 2003) is captured by our studies, indicating a general mismatch of ocean/sea-ice dynamics and SST-reconstruction. This emphasizes the importance of ice sheets and SST reconstruction in the Atlantic sector modifying the atmospheric circulation (Byrkjedal et al., 2006) and therefore sea-ice cover.

The annual mean sea-ice export from the Arctic (0.19–0.26 Sv) continues south via the EGC and is modified by sea-ice melting along the way, being deflected or reinforced by seasonal ice, which mainly evolved in the Norwegian Sea (not shown). Due to zonal drift patterns, a gradient of sea-ice thickness becomes apparent in the Nordic Seas (Fig. 5.3.2b, c). Meland et al. (2005) also find the pattern of that gradient in their SST reconstruction. In the absence of katabatic winds off the western flank of the Fenno-Scandinavian Ice-Sheet, the zonal pattern cannot be obtained (Fig. 5.3.12). Byrkjedal et al. (2006) have shown that the presence of sea-ice in the northern North Atlantic sector diminishes the Icelandic Low in contrast to less sea-ice in the northern North Atlantic Ocean which favors the formation of a cyclonic pattern. In turn LGMG suggests that a moderate cyclonic circulation over Iceland contributes to enhanced sea-ice export across Denmark Strait. The sea-ice transport from the Arctic Ocean and the Nordic Sea across the Denmark Strait (0.16–0.32 Sv) contributes to the freshwater budget in the northern North Atlantic.

5.4.3 Hypotheses of the glacial marine cryosphere in the central Arctic Ocean

The solid lines shown in Fig. 5.2.11 indicate the glacial ice drift proposed by Bischof and Darby (1997), compared to the recent patterns (dashed lines). Present sea-ice formation and sediment entrainment take place primarily in shallow water ($<$50 m water depth) of the Siberian Shelf. The Laptev Sea and the Kara Sea are important regions for sediment-laden sea-ice along today‘s Transpolar Drift (Nürnberg et al., 1994). This signal is reflected for the last 8 ka in the fine-grained sediment composition, an indicator for sea-ice rafted debris (Pfirman et al., 1989; Reimnitz et al., 1998; Nürnberg et al., 1994). The provenance of Fram Strait sediment was determined by matching the chemical signature of detrital iron oxide grains to $>$2000 potential circum-Arctic source compositions (Darby et al., 2002; Darby and Zimmerman, 2008). The sediments of the last ice age in the Fram Strait sediment core PS1230 are primarily from the Canadian Arctic Archipelago (Banks Island, Queen Elizabeth Island), which was covered by the Laurentide and Innuitian ice sheets at that time (Ehlers

and Gibbard, 2007). Calving Laurentide ice into the Arctic Ocean at this time occurred along the Amundsen Trough (Stokes et al., 2006) and the M'Clure Strait (Stokes et al., 2005). It has not yet been clarified whether these calving events led to an ice shelf in the Arctic Ocean or whether perennial sea-ice with icebergs of Antarctic dimension prevailed (Jakobsson et al., 2010). The Eurasian shelf seas were either covered by the Fenno-Scandinavian ice sheet (Ehlers and Gibbard, 2007) or exposed.

We propose that icebergs, which are also an important transport medium for sediments especially during the transition from glacial maxima to deglacial intervals, moved in the Arctic Ocean synchronously with sea-ice. While the iceberg drift is usually directed by several forces (water drag, wind stress, Coriolis force, inclination of the sea surface and interaction with sea-ice cover), iceberg drift buoys in the Weddell Sea (Antarctic) confirm that there is a coherent sea-ice/iceberg movement at ca. 90% sea-ice concentration (Schodlok et al., 2006). Low sedimentation rates, the absence of microorganisms, or even a hiatus in the sediment record, actually imply a thicker than today perennial ice cover with little melting in the central Arctic Ocean (Nørgaard-Pedersen et al., 1998; Polyak et al., 2004; Stein et al., 1994; Stein, 2008). The model studies show a gradient of sea-ice thickness across the Arctic Ocean that is different from today. Due to the convergence of drift, sea-ice is compressed to thicknesses of 11–20 m just north of Greenland and the advection area of Fram Strait, comparable to the recent pressure ridges of up to 20–30 m thickness in this area (e.g. Polyak et al., 2010). Whereas halted sea-ice would accumulate snowfall which slowly converts snow to firn and glacier ice up to 40 m height as seen from landfast-ice remnants of the little ice-age (Bradley and England, 2008). In this case variations of ice thickness in the central Arctic Ocean would be dependent on the surface mass balance and thermodynamic processes. Bradley and England (2008) argue that limited atmospheric circulation in the glacial Arctic Ocean favor this process and propose a mean ice thickness of 50 m in the Arctic Ocean. In the atmospheric forcing of our model studies, the North Pacific westerlies at the Laurentide ice sheet diverge forming a southern and northern branch. Winds of the northern branch are redirected across CAA intruding to the Arctic interior where sea-ice along the coast of CAA is pushed offshore to the central Arctic Ocean. Sea-ice is converging and pressure ridges of exceptional height evolve along its way towards Fram Strait forming a trans-arctic gradient of sea-ice thickness controlled by sea-ice dynamics.

5.4.4 Comparison of simulated and reconstructed glacial ice drift

Pleistocene ice drift reconstruction is illustrated by Phillips and Grantz (2001) utilizing the average MIS2 composition and distribution of erratics in Arctic Ocean sediments. They propose that the main Arctic circulation patterns, the Beaufort Gyre and Transpolar Drift operated, on average, during late Pleistocene glacial episodes. Further they associate westward migration of eolian sand dunes across northern Alaska (e.g. Dinter et al., 1990) with wind patterns driving the Beaufort Gyre at least since the LGM. In general these findings agree with the applied wind forcing fields of our model studies (Fig. 5.3.1b, c) as well as the anticyclonic sea-ice rotation in the Amerasian Basin (Fig. 5.3.3b, c).

Furthermore, ice plough marks (Fig. 5.2.1, blue arrows) along the Alaskan Beaufort Sea shelf edge and the border area of the Chukchi Sea, dated to the LGM, imply the orientation of ice drift (Engels et al., 2008; Polyak et al., 2001, 2007), which is consistent with the clockwise circulation in our model studies (Fig. 5.3.3b, c). Based on the IRD and DFA analysis Bischof

and Darby (1997) reconstruct iceberg trajectories originating from northwest Canada and the western Canadian Arctic Archipelago (Amundson Trough) traversing the Northwind Ridge and Chukchi Plateau before reaching Fram Strait. Icebergs sourcing from the Queen Elizabeth Islands primarily take a more direct route across central and southeastern Alpha Ridge (Bischof and Darby, 1997). They state that icebergs from the Innuitian and Laurentide ice-sheet take a direct pathway out of the Arctic Ocean without multiple anticyclonic rotations in the Amerasian Basin (Fig. 5.2.1, blue lines). Our glacial model studies still observe a downscaled anticyclonic gyre of ice drift in the Western Arctic whose center of rotation is shifted towards CAA compared to the present-day. This actually allows ice of the northern edge of the Laurentide ice-sheet to traverse the central Arctic Ocean in an arched pattern along the western Arctic shelf margin without multiple rotation in the glacial gyre (Fig. 5.3.3b, c) as proposed by Bischof and Darby (1997). During at least two glacial maxima, diamicton was deposited by grounding ice at the Chukchi Borderland (Polyak et al., 2007), which would divert sea-ice drift further northwards. Ice at the rim of the Innuitian ice sheet either takes the same arched pattern (LGMG, Fig. 5.3.3b) or slowly moves parallel to the coast of northern Greenland towards Fram Strait (LGMC, Fig. 5.3.3c). Differences in the atmospheric circulation (Fig. 5.3.1c) and pressure fields in the Arctic cause deviations in size and location of the anticyclonic ice drift pattern of LGMC and LGMG (Fig. 5.3.3). Further the reduced speed of sea-ice drift of our glacial model studies is directly affected by increased internal ice stress due to elevated ice thickness (not shown). Between Ellesmere Island and North Greenland (Lincoln Sea) Larsen et al. (2010) mapped glacial landforms and sediments and found evidence of shelf-based ice during the early stages of the last glacial ca. 30 kyr ago, which is not in the scope of the ocean/sea-ice model. For the formation of an ice shelf, thick multiyear sea-ice is required in order to disable shelf-ice calving into the ocean (Jakobsson et al., 2010; Larsen et al., 2010). The initialization started with outlet glacier streams that were deflected by the eastward sea-ice movement and final coalescence into an ice-shelf (Larsen et al., 2010). In our model studies, the Lincoln Sea is occupied by perennial sea-ice of maximum thickness (Fig. 5.3.2b, c) and virtually no ice-drift (Fig. 5.3.3b, c), which are favorable conditions for sustaining an ice-shelf. Further north, multi-year ice is drifting at 0.2–1 $\mathrm{cm\,s^{-1}}$ eastwards in agreement with the scenario of Larsen et al. (2010).

5.5 Conclusions

The panarctic ice-shelf cover postulated by Grosswald and Hughes (2008) provides an extreme case of glaciation with virtually no ice drift, which is not supported by our model simulations as well as more recent reconstructions (Jakobsson et al., 2010) nor the IRD record in Fram Strait (Darby and Zimmerman, 2008). Phillips and Grantz (2001) point out that the Beaufort Gyre and Transpolar Drift have been stable during late Pleistocene forced by wind fields consistent with proxy evidence from North Alaska. In contrast, our model studies still show an anti-cyclonic rotation in the Canadian Basin, which is shifted compared to the present-day pattern and a Transpolar Drift which is deflected or not present during LGM. Applying modern wind fields to the glacial model setup result in a general mismatch of simulated ice drift, ice cover and proxy data. As a consequence glacial wind stress is interpreted as the dominant operator of sea-ice drift. The arched pattern of simulated sea-ice drift results in a gradient of sea-ice thickness in the Arctic Ocean that is predominantly forced by glacial wind fields. The sources of MIS2 IRD in Fram Strait and other parts of the Arctic (Darby et al.,

2002; Darby and Zimmerman, 2008) and the orientation of dated ice plough marks (Engels et al., 2008; Polyak et al., 2001, 2007) substantiate our results.

Our approach overcomes the drawbacks of global climate models in representing circulation changes on a regional scale. The validation of our high-resolution regional Arctic ocean/sea-ice model, which has been used for hindcast and sea-ice prediction so far (Kauker et al., 2009) against the Last Glacial Maximum is crucial to understand physical processes concerning other climate regimes than today.

Chapter 6

Conclusions and perspectives

The general conclusions of the precedent three topics are summarized herein and each is appended by further perspectives. The research questions raised in the introduction are captured within the consequent summary.

The suite of orbital sensitivity studies in conjunction with altered CO_2 levels targets to analyze climate sensitivity at differential background climate states (Pre-industrial versus Tortonian, Chap. 3). It has been attested that climate sensitivity with respect to orbital parameters for the Pre-industrial is dissimilar from the Tortonian—therefore the null-hypothesis assumed in the introduction is rejected, leading to following questions: **How strong can CO_2 modulate the imprint of the orbital signal into climate? Can atmospheric CO_2 changes mimic a temperature anomaly, which is originally caused by changes of orbital parameters?** The choice of CO_2 levels strongly modulate climate sensitivity: Pre-industrial CO_2 at Tortonian climate allows for a stronger temperature response to external solar forcing whereas a high end member of CO_2 exhibits a muted temperature signal in the Arctic with respect to the Pre-industrial. The sea-ice feedback has been identified as a crucial nonlinear term in these studies, therefore atmospheric CO_2 and the orbital signal are not permutable in general. Further, at favorable CO_2 settings, the sea-ice feedback might have been crucial to amplify the orbital forcing for Northern Hemisphere glaciation, as indicated in previous modeling studies (Gallimore and Kutzbach, 1995; Jackson and Broccoli, 2003; Tuenter et al., 2005).

However, there are indications that generally speaking GCMs lack in spatial resolution quality (Chap. 5) and are potentially not sensitive enough (Valdes, 2011), e.g. sea-ice changes are reproduced too conservative (Jackson and Broccoli, 2003) for simulating recent warming trends (Boé et al., 2009). A further advance in understanding the physics of the nonlinear behavior of sea-ice (e.g. Coon et al., 1974; Timco and Frederking, 1990; Steiner et al., 1999; Timco and Weeks, 2010) is elementary.

Testing hypotheses of glacial inception from a modeling perspective (DeConto and Pollard, 2003; DeConto et al., 2008; Lunt et al., 2008) requires the inclusion of ice-sheet dynamics into GCMs. Potential feedbacks between ice-sheet, sea-ice, ocean, atmosphere and land surface dynamics have been proposed (DeConto and Pollard, 2003; DeConto et al., 2008; Lunt et al., 2008; Koenig et al., 2011). Therefore, the development of a full comprehensive Earth system model including ice-sheet dynamics is an urgent need. However, the absence of ice-sheet

model studies within the last IPCC (2007) report pointed out their inability of realistic simulation. So both, the fully integrative coupling towards GCMs as well as ice-sheet model development are necessary.

In Chap. 4 a soil scheme is created and coupled towards the existing GCM COSMOS. The dynamic feedback of soils is tested and investigated by means of mid-Holocene and Last Glacial Maximum climate. Questions raised in the context are as follows: **Do soil characteristics evolve linearly in a warmer and in a colder than pre-industrial scenario? Which regions are most sensitive to soil changes and via which mechanisms of the climate system do they interact with?** The integrated soil feedback leads to amplified global climate anomalies: About 70% (+0.24°C) of change in surface air temperatures for mid-Holocene and ca. 15% (-1.07°C) for LGM can be attributed to the integrated effect of soil dynamics. Especially regions like the transition zone of desert/savannah and taiga/tundra which are characterized by strong gradients of vegetation cover, exhibit an increased response as a result of the modified soil treatment. In comparison to former studies, the inclusion of the soil feedback pushes our model simulations towards the warmer end in the range of mid-Holocene studies (O'ishi and Abe-Ouchi, 2011) and beyond current estimates of global cooling during the Last Glacial Maximum based on PMIP2 (Paleoclimate Modeling Intercomparison Project 2) studies (Braconnot et al., 2007, 2012). The main impact of the interactive soil scheme on the climate response is governed by positive feedbacks, including dynamics of vegetation, snow, sea-ice and local water recycling.

As an outlook, GCM studies with the expedient of a dynamic soil model investigating times of the Cenozoic (e.g. Tortonian) may shed some light onto the equable climate enigma (Ruddiman, 2010). The additional mid-Holocene warming, caused by the soil feedback, already indicated a direction of the trend. Therefore, ongoing studies with the soil scheme for pre-Quaternary setups appear promising. However, dynamic vegetation models at their current state need improvement to achieve a more realistic simulation of global vegetation distribution under different climate scenarios (e.g. Knorr et al., 2011). This drawback is transmitted to the soil impact, since vegetation and soil scheme are closely interacting (Sect. 2.1.2).

Further, pedogenesis might play some role in altering gross terrestrial primary productivity. Still it is under debate, which CO_2 reservoirs mobilized atmospheric CO_2 of ca. 100 ppmv during late Pleistocene glacial/interglacial transitions (Petit et al., 1999; Ciais et al., 2012).

Current state-of-the-art GCMs are lacking feedback mechanisms (dust/aerosol, land ice-sheets, carbon cycle), which are important to address Earth system sensitivity (PALEOSENS Project Members; Rohling et al., 2012). As shown by Claussen et al. (2006), transient model simulations with vegetation dynamics show a reinforced response to precession forcing. Additionally, the soil feedback might raise Earth system sensitivity on different timescales. Therefore, the present equilibrium soil scheme needs further development for a synchronous coupling with COSMOS and the inclusion of a time dependent function in order to account for nonlinear soil gradation (Johnson et al., 1990; Hoosbeek and Bryant, 1992; Lin, 2011).

Pedogenesis is only one point on the agenda of model development in regard to dynamic land surface processes. More sophisticated treatment is needed for the hydrological cycle on land (bucket versus multilayer model) and the simulation of permafrost thawing and subsequent methane emissions.

A special focus on the glacial Arctic Ocean requires a (regional ocean/sea-ice) model

(NAOSIM) with spatial adequate resolution of its dynamics (Stärz et al., 2012). Within Chap. 5, the following research questions are addressed: **How dynamic are the marine and cryospheric components of the glacial Arctic Ocean? Is there interaction via the single glacial Arctic Ocean gateway, the Fram Strait, for Northern North Atlantic waters and vice versa?** The model studies are in congruence with geological data that present an extreme shortcut of glacial ice drift. In more detail, the results show a clockwise sea-ice drift in the western Arctic Basin that merges into a direct trans-Arctic path towards Fram Strait. This is consistent with dated ice plough marks on the seafloor, which show the orientation of iceberg drift in this direction. Furthermore, ice-transported iron-oxide grains deposited in Fram Strait, can be matched by their chemical composition to similar grains found in potential sources from the entire circum-Arctic. In our model the volume flux of Northern North Atlantic waters across Fram Strait, which is, however, still a matter of debate (Haley et al., 2008; Jakobsson et al., 2010; Cronin et al., 2012), increased and changed its water mass characteristics. The model results indicate that the patterns of Arctic sea-ice drift during the LGM are established by wind fields, and seem to be a general feature of the glacial ocean. The model results do not indicate a cessation in ice drift during the LGM.

Our results need further validation by ongoing model studies. If the glacial Arctic marine cryosphere is not as static as previously thought, how does its mobility impact the global climate and how does it change its dynamics through deglaciation? Bengtsson et al. (2004) and Semenov et al. (2009) show that changes in sea-ice cover can positively feed back on atmosphere and ocean dynamics. As a next step, modeling the last glacial termination in order to investigate the impact of the Arctic Ocean from a global perspective, need models with high spatial and temporal resolution . The improve modeling approach should be accompanied by a coring campaign to retrieve more proxy data to provide precise background boundary conditions for model setups.

Bibliography

Aagaard, K., Carmack, E. C., 1989. The Role of Sea Ice and Other Fresh Water in the Arctic Circulation. Journal of Geophysical Research 94 (C10), 14485–14498.

Adams, J. M., Faure, H., Fauredenard, L., McGlade, J. M., Woodward, F. I., 1990. Increases in terrestrial carbon storage from the Last Glacial Maximum to the present. Nature 348 (6303), 711–714.

Alkama, R., Kageyama, M., Ramstein, G., Marti, O., Ribstein, P., Swingedouw, D., 2008. Impact of a realistic river routing in coupled ocean–atmosphere simulations of the Last Glacial Maximum climate. Climate Dynamics 30 (7), 855–869.

Anhuf, D., Ledru, M.-P., Behling, H., Da Cruz, F. W. J., Cordeiro, R. C., van der Hammen, T., Karmann, I., Marengo, J. A., Oliveira, P. E. d., Pessenda, L., Siffedine, A., Albuquerque, A. L., Da Silva Dias, P. L., 2006. Paleo-environmental change in Amazonian and African rainforest during the LGM. Palaeogeography, Palaeoclimatology, Palaeoecology 239 (3–4), 510–527.

Annan, J. D., Hargreaves, J. C., 2013. A new global reconstruction of temperature changes at the Last Glacial Maximum. Climate of the Past 9 (1), 367–376.

Arkhipov, S. A., Isayeva, L. L., Bespaly, V. G., Glushkova, O., 1986. Glaciation of Siberia and north-east USSR. Quaternary Science Reviews 5 (0), 463–474.

Baker, P. A., Rigsby, C. A., Seltzer, G. O., Fritz, S. C., Lowenstein, T. K., Bacher, N. P., Veliz, C., 2001. Tropical climate changes at millennial and orbital timescales on the Bolivian Altiplano. Nature 409 (6821), 698–701.

Bartlein, P. J., Harrison, S. P., Brewer, S., Connor, S., Davis, B. A. S., Gajewski, K., Guiot, J., Harrison-Prentice, T. I., Henderson, A., Peyron, O., Prentice, I. C., Scholze, M., Seppä, H., Shuman, B., Sugita, S., Thompson, R. S., Viau, A. E., Williams, J., Wu, H., 2011. Pollen-based continental climate reconstructions at 6 and 21 ka: a global synthesis. Climate Dynamics 37 (3–4), 775–802.

Bengtsson, L., Semenov, V. A., Johannessen, O. M., 2004. The Early Twentieth-Century Warming in the Arctic–A Possible Mechanism. Journal of Climate 17 (20), 4045–4057.

Bergengren, J. C., Thompson, S. L., Pollard, D., DeConto, R. M., 2001. Modeling Global Climate—Vegetation Interactions in a Doubled CO_2 World. Climatic Change 50 (1–2), 31–75.

Berger, A. L., 1978. Long-Term Variations of Daily Insolation and Quaternary Climatic Changes. Journal of the Atmospheric Sciences 35 (12), 2362–2367.

Bischof, J. F., Darby, D. A., 1997. Mid- to Late Pleistocene Ice Drift in the Western Arctic Ocean: Evidence for a Different Circulation in the Past. Science 277 (5322), 74–78.

Boé, J., Hall, A., Qu, X., 2009. September sea-ice cover in the Arctic Ocean projected to vanish by 2100. Nature Geoscience 2 (5), 341–343.

Bonfils, C., de Noblet-Ducoudré, N., Braconnot, P., Joussaume, S., 2001. Hot desert albedo and climate change: Mid-Holocene monsoon in North Africa. Journal of Climate 14 (17), 3724–3737.

Braconnot, P., Harrison, S. P., Kageyama, M., Bartlein, P. J., Masson-Delmotte, V., Abe-Ouchi, A., Otto-Bliesner, B., Zhao, Y., 2012. Evaluation of climate models using palaeoclimatic data. Nature Climate Change 2 (6), 417–424.

Braconnot, P., Joussaume, S., Marti, O., de Noblet, N., 1999. Synergistic feedbacks from ocean and vegetation on the African monsoon response to mid-Holocene insolation. Geophysical Research Letters 26 (16), 2481–2484.

Braconnot, P., Otto-Bliesner, B., Harrison, S., Joussaume, S., Peterchmitt, J.-Y., Abe-Ouchi, A., Crucifix, M., Driesschaert, E., Fichefet, T., Hewitt, C. D., Kageyama, M., Kitoh, A., Loutre, M.-F., Marti, O., Merkel, U., Ramstein, G., Valdes, P., Weber, L., Yu, Y., Zhao, Y., 2007. Results of PMIP2 coupled simulations of the Mid-Holocene and Last Glacial Maximum - Part 2: feedbacks with emphasis on the location of the ITCZ and mid- and high latitudes heat budget. Climate of the Past 3 (2), 279–296.

Bradley, R. S., England, J. H., 2008. The Younger Dryas and the Sea of Ancient Ice. Quaternary Research 70 (1), 1–10.

Broström, A., oe, M., Harrison, S. P., Gallimore, R., Kutzbach, J. E., Foley, J., Prentice, I. C., Behling, P., 1998. Land surface feedbacks and palaeomonsoons in northern Africa. Geophysical Research Letters 25 (19), 3615–3618.

Brovkin, V., Bendtsen, J., Claussen, M., Ganopolski, A., Kubatzki, C., Petoukhov, V., Andreev, A., 2002. Carbon cycle, vegetation, and climate dynamics in the Holocene: Experiments with the CLIMBER-2 model. Global Biogeochemical Cycles 16 (4), 1139.

Brovkin, V., Raddatz, T., Reick, C. H., Claussen, M., Gayler, V., 2009. Global biogeophysical interactions between forest and climate. Geophysical Research Letters 36, L07405.

Butzin, M., Prange, M., Lohmann, G., 2005. Radiocarbon simulations for the glacial ocean: The effects of wind stress, Southern Ocean sea ice and Heinrich events. Earth and Planetary Science Letters 235 (1-2), 45–61.

Byrkjedal, Ø., Kvamstø, N., Meland, M., Jansen, E., 2006. Sensitivity of last glacial maximum climate to sea ice conditions in the Nordic Seas. Climate Dynamics 26 (5), 473–487.

Carrington, D. P., Gallimore, R. G., Kutzbach, J. E., 2001. Climate sensitivity to wetlands and wetland vegetation in mid-Holocene North Africa. Climate Dynamics 17 (2-3), 151–157.

Charney, J. G., 1975. Dynamics of deserts and drought in the Sahel. Quarterly Journal of the Royal Meteorological Society 101 (428), 193–202.

Charney, J. G., Quirk, W. J., Chow, S.-H., Kornfield, J., 1977. A Comparative Study of the Effects of Albedo Change on Drought in Semi–Arid Regions. Journal of Atmospheric Sciences 34 (9), 1366–1385.

Ciais, P., Tagliabue, A., Cuntz, M., Bopp, L., Scholze, M., Hoffmann, G., Lourantou, A., Harrison, S. P., Prentice, I. C., Kelley, D. I., Koven, C., Piao, S. L., 2012. Large inert carbon pool in the terrestrial biosphere during the Last Glacial Maximum. Nature Geoscience 5 (1), 74–79.

Clark, P. U., Alley, R. B., Pollard, D., 1999. Northern Hemisphere Ice-Sheet Influences on Global Climate Change. Science 286 (5442), 1104–1111.

Claussen, M., 1994. On coupling global biome models with climate models. Climate Research 4 (3), 203–221.

Claussen, M., 1997. Modeling bio-geophysical feedback in the African and Indian monsoon region. Climate Dynamics 13 (4), 247–257.

Claussen, M., 2009. Late Quaternary vegetation-climate feedbacks. Climate of the Past 5 (2), 203–216.

Claussen, M., Fohlmeister, J., Ganopolski, A., Brovkin, V., 2006. Vegetation dynamics amplifies precessional forcing. Geophysical Research Letters 33 (9), L09709.

Claussen, M., Gayler, V., 1997. The Greening of the Sahara during the Mid-Holocene: Results of an Interactive Atmosphere-Biome Model. Global Ecology and Biogeography Letters 6 (5), 369–377.

CLIMAP, 1981. Seasonal Reconstruction of the Earth's Surface at the Last Glacial Maximum. Geological Society of America Map and Chart Series MC-36. Geological Society of America, Boulder, Colorado.

Coe, M. T., Bonan, G. B., 1997. Feedbacks between climate and surface water in northern Africa during the middle Holocene. Journal of Geophysical Research: Atmospheres 102 (D10), 11087–11101.

Colman, R., McAvaney, B., 2009. Climate feedbacks under a very broad range of forcing. Geophysical Research Letters 36 (1), L01702.

Coon, M. D., Maykut, G. A., Pritchard, R. S., Rothrock, D. A., S., T. A., 1974. Modelling the pack ice as an elastic-plastic material. Aidjex Bulletin 24, 1–105.

Croll, J., 1875. Climate and time in their geological relations: a theory of secular changes of the earth's climate. D. Appleton & Co., New York.

Cronin, T. M., Dwyer, G. S., Farmer, J., Bauch, H. A., Spielhagen, R. F., Jakobsson, M., Nilsson, J., Briggs, W. M., Stepanova, A., 2012. Deep Arctic Ocean warming during the last glacial cycle. Nature Geoscience 5 (9), 631–634.

Darby, D. A., Bischof, J. F., Spielhagen, R. F., Marshall, S. A., Herman, S. W., 2002. Arctic ice export events and their potential impact on global climate during the late Pleistocene. Paleoceanography 17 (2).

Darby, D. A., Myers, W. B., Jakobsson, M., Rigor, I., 2011. Modern dirty sea ice characteristics and sources: The role of anchor ice. Journal of Geophysical Research: Oceans 116 (C9), C09008.

Darby, D. A., Zimmerman, P., 2008. Ice-rafted detritus events in the Arctic during the last glacial interval, and the timing of the Innuitian and Laurentide ice sheet calving events. Polar Research 27 (2), 114–127.

DeConto, R. M., Pollard, D., 2003. Rapid Cenozoic glaciation of Antarctica induced by declining atmospheric CO_2. Nature 421, 245– 249.

DeConto, R. M., Pollard, D., Wilson, P. A., Pälike, H., Lear, C. H., Pagani, M., 2008. Thresholds for Cenozoic bipolar glaciation. Nature 455, 652–656.

deMenocal, P. B., Rind, D., 1993. Sensitivity of Asian and African climate to variations in seasonal insolation, glacial ice cover, sea surface temperature, and Asian orography. Journal of Geophysical Research: Atmospheres 98 (D4), 7265–7287.

Dinter, D., Carter, L., Brigham-Grette, J., 1990. Late Cenozoic geologic evolution of the Alaskan North Slope and adjacent continental shelves. In: Grantz, A., Johnson, G., Sweeney, J. (Eds.), The Arctic Ocean region. The Geology of North America. Geological Society of America, Boulder, Colorado, pp. 459–490.

Dümenil, L., Todini, E., 1992. A rainfall-runoff scheme for use in the Hamburg climate model. In: O'Kane, J. P. (Ed.), Advances in theoretical hydrology–A tribute to James Dooge. Vol. 1 of European geophysical society series on hydrological sciences. Elsevier Science, Amsterdam, pp. 129–157.

Doherty, R., Kutzbach, J., Foley, J., Pollard, D., 2000. Fully coupled climate/dynamical vegetation model simulations over Northern Africa during the mid-Holocene. Climate Dynamics 16 (8), 561–573.

Dolan, A. M., Haywood, A. M., Hill, D. J., Dowsett, H. J., Hunter, S. J., Lunt, D. J., Pickering, S. J., 2011. Sensitivity of Pliocene ice sheets to orbital forcing. Palaeogeography, Palaeoclimatology, Palaeoecology 309 (1–2), 98–110, special Issue: Climate and seasonality in a Pliocene warm world.

Dong, B., Valdes, P. J., 1995. Sensitivity Studies of Northern Hemisphere Glaciation Using an Atmospheric General Circulation Model. Journal of Climate 8 (10), 2471–2496.

Douville, H., Chauvin, F., Broqua, H., 2001. Influence of Soil Moisture on the Asian and African Monsoons. Part I: Mean Monsoon and Daily Precipitation. Journal of Climate 14 (11), 2381–2403.

Douville, H., Conil, S., Tyteca, S., Voldoire, A., 2007. Soil moisture memory and West African monsoon predictability: artefact or reality? Climate Dynamics 28 (7-8), 723–742.

Dowsett, H. J., Robinson, M. M., Foley, K. M., 2009. Pliocene three-dimensional global ocean temperature reconstruction. Climate of the Past 5 (4), 769–783.

Dupont, L., 2011. Orbital scale vegetation change in Africa. Quaternary Science Reviews 30 (25–26), 3589–3602.

Dyck, S., Tremblay, L. B., Vernal, A. d., 2010. Arctic sea-ice cover from the early Holocene: the role of atmospheric circulation patterns: APEX: Arctic Palaeoclimate and its Extremes. Quaternary Science Reviews 29 (25–26), 3457–3467.

Ehlers, J., Gibbard, P. L., 2007. The extent and chronology of Cenozoic Global Glaciation: From the Swiss Alps to the Crimean Mountains - Alpine Quaternary stratigraphy in a European context. Quaternary International 164-165, 6–20.

Engels, J. L., Edwards, M. H., Polyak, L., Johnson, P. D., 2008. Seafloor evidence for ice shelf flow across the Alaska–Beaufort margin of the Arctic Ocean. Earth Surface Processes and Landforms 33 (7), 1047–1063.

Fairbanks, R. G., 1989. A 17,000-year glacio-eustatic sea level record: influence of glacial melting rates on the Younger Dryas event and deep-ocean circulation. Nature 342 (6250), 637–642.

Fedorov, A. V., Brierley, C. M., Lawrence, K. T., Liu, Z., Dekens, P. S., Ravelo, A. C., 2013. Patterns and mechanisms of early Pliocene warmth. Nature 496, 43–49.

Felis, T., Lohmann, G., Kuhnert, H., Lorenz, S. J., Scholz, D., Pätzold, J., Al-Rousan, S. A., Al-Moghrabi, S. M., 2004. Increased seasonality in Middle East temperatures during the last interglacial period. Nature 429 (6988), 164–168.

Foley, J. A., Coe, M. T., Scheffer, M., Wang, G., 2003. Regime Shifts in the Sahara and Sahel: Interactions between Ecological and Climatic Systems in Northern Africa. Ecosystems 6 (6), 524–532.

Foley, J. A., Kutzbach, J. E., Coe, M. T., Levis, S., 1994. Feedbacks between climate and boreal forests during the Holocene epoch. Nature 371 (6492), 52–54.

Foley, J. A., Levis, S., Costa, M. H., Cramer, W., Pollard, D., 2000. Incorporating dynamic vegetation cover within global climate models. Ecological Applications 10 (6), 1620–1632.

Gallimore, R., Jacob, R., Kutzbach, J., 2005. Coupled atmosphere-ocean-vegetation simulations for modern and mid-Holocene climates: role of extratropical vegetation cover feedbacks. Climate Dynamics 25 (7-8), 755–776.

Gallimore, R. G., Kutzbach, J. E., 1995. Snow cover and sea ice sensitivity to generic changes in Earth orbital parameters. Journal of Geophysical Research: Atmospheres 100 (D1), 1103–1120.

Ganopolski, A., Calov, R., 2011. The role of orbital forcing, carbon dioxide and regolith in 100 kyr glacial cycles. Climate of the Past 7 (4), 1415–1425.

Gong, X., Knorr, G., Lohmann, G., Zhang, X., 2013. Dependence of abrupt Atlantic meridional ocean circulation changes on climate background states. Geophysical Research Letters 40 (14), 3698–3704.

Grosswald, M., Hughes, T., 2008. The case for an ice shelf in the pleistocene Arctic Ocean. Polar Geography 31 (1), 69–98.

Hagemann, S., Botzet, M., Dümenil, L., Machenhauer, B., 1999. Derivation of global GCM boundary conditions from 1 km land use satellite data. Max- Planck-Institut für Meteorologie, Hamburg, Rep 289.

Haley, B. A., Frank, M., Spielhagen, R. F., Fietzke, J., 2008. Radiogenic isotope record of Arctic Ocean circulation and weathering inputs of the past 15 million years. Paleoceanography 23 (1), PA1S13.

Hall, A., Qu, X., Neelin, J. D., 2008. Improving predictions of summer climate change in the United States. Geophysical Research Letters 35 (1), L01702.

Harden, J. W., Sundquist, E. T., Stallard, R. F., Mark, R. K., 1992. Dynamics of soil carbon during deglaciation of the Laurentide ice-sheet. Science 258 (5090), 1921–1924.

Hargreaves, J. C., Annan, J. D., Ohgaito, R., Paul, A., Abe-Ouchi, A., 2013. Skill and reliability of climate model ensembles at the Last Glacial Maximum and mid-Holocene. Climate of the Past 9 (2), 811–823.

Haywood, A. M., Hill, D. J., Dolan, A. M., Otto-Bliesner, B. L., Bragg, F., Chan, W.-L., Chandler, M. A., Contoux, C., Dowsett, H. J., Jost, A., Kamae, Y., Lohmann, G., Lunt, D. J., Abe-Ouchi, A., Pickering, S. J., Ramstein, G., Rosenbloom, N. A., Salzmann, U., Sohl, L., Stepanek, C., Ueda, H., Yan, Q., Zhang, Z., 2013. Large-scale features of Pliocene climate: results from the Pliocene Model Intercomparison Project. Climate of the Past 9 (1), 191–209.

Haywood, A. M., Valdes, P. J., Sellwood, B. W., 2002. Magnitude of climate variability during middle Pliocene warmth: a palaeoclimate modelling study. Palaeogeography, Palaeoclimatology, Palaeoecology 188 (1–2), 1–24.

Hebbeln, D., Dokken, T., Andersen, E. S., Hald, M., Elverhøi, A., 1994. Moisture supply for northern ice-sheet growth during the Last Glacial Maximum. Nature 370 (6488), 357–360.

Henderson-Sellers, A., 1993. Continental vegetation as a dynamic component of a global climate model: a preliminary assessment. Climatic Change 23 (4), 337–377.

Henderson-Sellers, A., Wilson, M. F., Thomas, G., Dickinson, R. E., 1986. Current global land-surface data sets for use in climate-related studies. NCAR Technical Note 272, Boulder, Colorado.

Herold, M., Lohmann, G., 2009. Eemian tropical and subtropical African moisture transport: an isotope modelling study. Climate Dynamics 33 (7-8), 1075–1088.

Hesse, T., Butzin, M., Bickert, T., Lohmann, G., 2011. A model-data comparison of $\delta^{13}C$ in the glacial Atlantic Ocean. Paleoceanography 26 (3), PA3220.

Hibler, W. D., 1979. A Dynamic Thermodynamic Sea Ice Model. Journal of Physical Oceanography 9 (4), 815–846.

Hönisch, B., Hemming, N. G., Archer, D., Siddall, M., McManus, J. F., 2009. Atmospheric Carbon Dioxide Concentration Across the Mid-Pleistocene Transition. Science 324 (5934), 1551–1554.

Hoelzmann, P., Jolly, D., Harrison, S. P., Laarif, F., Bonnefille, R., Pachur, H.-J., 1998. Mid-Holocene land-surface conditions in northern Africa and the Arabian Peninsula: A data set for the analysis of biogeophysical feedbacks in the climate system. Global Biogeochemical Cycles 12 (1), 35–51.

Hoelzmann, P., Kruse, H.-J., Rottinger, F., 2000. Precipitation estimates for the eastern Saharan palaeomonsoon based on a water balance model of the West Nubian Palaeolake Basin. Global and Planetary Change 26 (1–3), 105–120.

Holdridge, L. R., 1947. Determination of World Plant Formations From Simple Climatic Data. Science 105 (2727), 367–368.

Holland, M., Bitz, C., 2003. Polar amplification of climate change in coupled models. Climate Dynamics 21 (3–4), 221–232.

Hoosbeek, M. R., Bryant, R. B., 1992. Towards the quantitative modeling of pedogenesis — a review. Geoderma 55 (3–4), 183–210.

Hubberten, H. W., Andreev, A., Astakhov, V. I., Demidov, I., Dowdeswell, J. A., Henriksen, M., Hjort, C., Houmark-Nielsen, M., Jakobsson, M., Kuzmina, S., Larsen, E., Lunkka, J. P., Lyså, A., Mangerud, J., Möller, P., Saarnisto, M., Schirrmeister, L., Sher, A. V., Siegert, C., Siegert, M. J., Svendsen, J. I., 2004. The periglacial climate and environment in northern Eurasia during the Last Glaciation: Quaternary Environments of the Eurasian North (QUEEN). Quaternary Science Reviews 23 (11–13), 1333–1357.

Huber, M., Caballero, R., 2011. The early Eocene equable climate problem revisited. Climate of the Past 7 (2), 603–633.

IPCC, 2007. Climate Change 2007: The Physical Science Basis. Contribution of Working Group I to the Fourth Assessment Report of the Intergovernmental Panel on Climate Change. Cambridge University Press, Cambridge, United Kingdom and New York, NY, USA.

Jackson, C., Broccoli, A., 2003. Orbital forcing of Arctic climate: mechanisms of climate response and implications for continental glaciation. Climate Dynamics 21 (7–8), 539–557.

Jakobsson, M., Nilsson, J., O'Regan, M., Backman, J., Löwemark, L., Dowdeswell, J. A., Mayer, L., Polyak, L., Colleoni, F., Anderson, L. G., Björk, G., Darby, D., Eriksson, B., Hanslik, D., Hell, B., Marcussen, C., Sellén, E., Wallin, Å., 2010. An Arctic Ocean ice shelf during MIS 6 constrained by new geophysical and geological data: APEX: Arctic Palaeoclimate and its Extremes. Quaternary Science Reviews 29 (25-26), 3505–3517.

Jansen, E., Overpeck, J., Briffa, K., Duplessy, J.-C., Joos, F., Masson-Delmotte, V., Olago, D., Otto-Bliesner, B., Peltier, W., Rahmstorf, S., Ramesh, R., Raynaud, D., Rind, D., Solomina, O., Villalba, R., Zhang, D., 2007. Palaeoclimate. In: Climate Change 2007: The Physical Science Basis. Contribution of Working Group I to the Fourth Assessment Report of the Intergovernmental Panel on Climate Change. Cambridge University Press, Cambridge, United Kingdom and New York, NY, USA, Ch. Palaeoclimate.

Jenkyns, H., Forster, A., Schouten, S., Damste, J., DEC 16 2004. High temperatures in the Late Cretaceous Arctic Ocean. Nature 432 (7019), 888–892.

Jenny, H., 1941. Factors of soil formation. McGraw-Hill Book Company, New York, London.

Jiang, D., 2008. Vegetation and soil feedbacks at the Last Glacial Maximum. Palaeogeography, Palaeoclimatology, Palaeoecology 268 (1–2), 39–46.

Johnson, D. L., Keller, E. A., Rockwell, T. K., 1990. Dynamic pedogenesis: New views on some key soil concepts, and a model for interpreting quaternary soils. Quaternary Research 33 (3), 306–319.

Jungclaus, J. H., Keenlyside, N., Botzet, M., Haak, H., Luo, J.-J., Latif, M., Marotzke, J., Mikolajewicz, U., Roeckner, E., 2006. Ocean circulation and tropical variability in the coupled model ECHAM5/MPI-OM. Journal of Climate 19 (16), 3952–3972.

Kageyama, M., Laîné, A., Abe-Ouchi, A., Braconnot, P., Cortijo, E., Crucifix, M., Vernal, A. d., Guiot, J., Hewitt, C. D., Kitoh, A., Kucera, M., Marti, O., Ohgaito, R., Otto-Bliesner, B., Peltier, W. R., Rosell-Melé, A., Vettoretti, G., Weber, S. L., Yu, Y., 2006. Last Glacial Maximum temperatures over the North Atlantic, Europe and western Siberia: a comparison between PMIP models, MARGO sea–surface temperatures and pollen-based reconstructions. Quaternary Science Reviews 25 (17–18), 2082–2102.

Kalnay, E., Kanamitsu, M., Kistler, R., Collins, W., Deaven, D., Gandin, L., Iredell, M., Saha, S., White, G., Woollen, J., Zhu, Y., Leetmaa, A., Reynolds, R., Chelliah, M., Ebisuzaki, W., Higgins, W., Janowiak, J., Mo, K. C., Ropelewski, C., Wang, J., Jenne, R., Joseph, D., 1996. The NCEP/NCAR 40-Year Reanalysis Project. Bulletin of the American Meteorological Society 77 (3), 437–471.

Karcher, M. J., Oberhuber, J. M., 2002. Pathways and modification of the upper and intermediate waters of the Arctic Ocean. Journal of Geophysical Research 107 (C6).

Kauker, F., Gerdes, R., Karcher, M., Köberle, C., 2005. Impact of North Atlantic Current changes on the Nordic Seas and the Arctic Ocean. Journal of Geophysical Research 110 (C12), C12002.

Kauker, F., Gerdes, R., Karcher, M., Köberle, C., Lieser, J. L., 2003. Variability of Arctic and North Atlantic sea ice: A combined analysis of model results and observations from 1978 to 2001. Journal of Geophysical Research 108 (C6).

Kauker, F., Kaminski, T., Karcher, M., Giering, R., Gerdes, R., Voßbeck, M., 2009. Adjoint analysis of the 2007 all time Arctic sea-ice minimum. Geophysical Research Letters 36 (3), L03707.

Knies, J., Nowaczyk, N., Müller, C., Vogt, C., Stein, R., 2000. A multiproxy approach to reconstruct the environmental changes along the Eurasian continental margin over the last 150 000 years. Marine Geology 163 (1–4), 317–344.

Knorr, G., Butzin, M., Micheels, A., Lohmann, G., 2011. A warm Miocene climate at low atmospheric CO_2 levels. Geophysical Research Letters 38 (20), L20701.

Knorr, W., 2000. Annual and interannual CO_2 exchanges of the terrestrial biosphere: process-based simulations and uncertainties. Global Ecology and Biogeography 9 (3), 225–252.

Knorr, W., Schnitzler, K. G., 2006. Enhanced albedo feedback in North Africa from possible combined vegetation and soil-formation processes. Climate Dynamics 26 (1), 55–63.

Köberle, C., Gerdes, R., 2003. Mechanisms Determining the Variability of Arctic Sea Ice Conditions and Export. Journal of Climate 16 (17), 2843–2858.

Koenig, S., DeConto, R., Pollard, D., 2011. Late Pliocene to Pleistocene sensitivity of the Greenland Ice Sheet in response to external forcing and internal feedbacks. Climate Dynamics 37 (5–6), 1247–1268.

Krapp, M., Jungclaus, J. H., 2011. The Middle Miocene climate as modelled in an atmosphere-ocean-biosphere model. Climate of the Past 7 (4), 1169–1188.

Krinner, G., Lezine, A. M., Braconnot, P., Sepulchre, P., Ramstein, G., Grenier, C., Gouttevin, I., 2012. A reassessment of lake and wetland feedbacks on the North African Holocene climate. Geophysical Research Letters 39, L07701.

Krylov, A. A., Andreeva, I. A., Vogt, C., Backman, J., Krupskaya, V. V., Grikurov, G. E., Moran, K., Shoji, H., 2008. A shift in heavy and clay mineral provenance indicates a middle Miocene onset of a perennial sea ice cover in the Arctic Ocean. Paleoceanography 23 (1), PA1S06.

Kump, L. R., Pollard, D., 2008. Amplification of Cretaceous Warmth by Biological Cloud Feedbacks. Science 320 (5873), 195.

Kutzbach, J. E., Bonan, G., Foley, J., Harrison, S. P., 1996. Vegetation and soil feedbacks on the response of the African monsoon to orbital forcing in the early to middle Holocene. Nature 384 (6610), 623–626.

Kutzbach, J. E., Guetter, P. J., 1986. The Influence of Changing Orbital Parameters and Surface Boundary Conditions on Climate Simulations for the Past 18000 Years. Journal of the Atmospheric Sciences, 1726–1759.

Kutzbach, J. E., Otto-Bliesner, B. L., 1982. The Sensitivity of the African-Asian Monsoonal Climate to Orbital Parameter Changes for 9000 Years B.P. in a Low-Resolution General Circulation Model. Journal of the Atmospheric Sciences (6), 1177–1188.

Kutzbach, J. E., Street-Perrott, F. A., 1985. Milankovitch forcing of fluctuations in the level of tropical lakes from 18 to 0 kyr BP. Nature 317 (6033), 130–134.

Lambeck, K., Esat, T. M., Potter, E.-K., 2002. Links between climate and sea levels for the past three million years. Nature 419 (6903), 199–206.

Larsen, N. K., Kjær, K. H., Funder, S., Möller, P., van der Meer, J. J. M., Schomacker, A., Linge, H., Darby, D. A., 2010. Late Quaternary glaciation history of northernmost Greenland – Evidence of shelf-based ice: APEX: Arctic Palaeoclimate and its Extremes. Quaternary Science Reviews 29 (25–26), 3399–3414.

Levis, S., Bonan, G. B., Bonfils, C., 2004. Soil feedback drives the mid-Holocene North African monsoon northward in fully coupled CCSM2 simulations with a dynamic vegetation model. Climate Dynamics 23 (7-8), 791–802.

Levitus, S., Boyer, T. P. (Eds.), 1994. Temperature: Vol. 4, World Ocean Atlas 1994. U.S. Department of Commerce, Washington and D.C.

Levitus, S., Burgett, R., Boyer, T. P. (Eds.), 1994. Salinity: Vol 3., World Ocean Atlas 1994. U.S. Department of Commerce, Washington and D.C.

Lin, H., 2011. Three Principles of Soil Change and Pedogenesis in Time and Space. Soil Science Society of America Journal 75, 2049–2070.

Lisiecki, L. E., Raymo, M. E., 2005. A Pliocene-Pleistocene stack of 57 globally distributed benthic $\delta^{18}O$ records. Paleoceanography 20 (1), PA1003.

Lohmann, G., Lorenz, S., 2000. On the hydrological cycle under paleoclimatic conditions as derived from AGCM simulations. Journal of Geophysical Research 105 (D13), 17417–17436.

Lohmann, G., Lorenz, S. J., Prange, M., 2005. Northern high-latitude climate changes during the Holocene as simulated by circulation models. In: Geophysical Monograph Series. Vol. 158. AGU, Washington, DC, pp. 273–288.

Lohmann, G., Pfeiffer, M., Laepple, T., Leduc, G., Kim, J.-H., 2012. A model-data comparison of the Holocene global sea surface temperature evolution. Climate of the Past Discussions 8 (2), 1005–1056.

Lorenz, S. J., Lohmann, G., 2004. Acceleration technique for Milankovitch type forcing in a coupled atmosphere-ocean circulation model: method and application for the Holocene. Climate Dynamics 23 (7–8), 727–743.

Lunt, D. J., Abe-Ouchi, A., Bakker, P., Berger, A., Braconnot, P., Charbit, S., Fischer, N., Herold, N., Jungclaus, J. H., Khon, V. C., Krebs-Kanzow, U., Langebroek, P. M., Lohmann, G., Nisancioglu, K. H., Otto-Bliesner, B. L., Park, W., Pfeiffer, M., Phipps, S. J., Prange, M., Rachmayani, R., Renssen, H., Rosenbloom, N., Schneider, B., Stone, E. J., Takahashi, K., Wei, W., Yin, Q., Zhang, Z. S., 2013. A multi-model assessment of last interglacial temperatures. Climate of the Past 9 (2), 699–717.

Lunt, D. J., Foster, G. L., Haywood, A. M., Stone, E. J., 2008. Late Pliocene Greenland glaciation controlled by a decline in atmospheric CO_2 levels. Nature 454, 1102–1105.

Lunt, D. J., Haywood, A. M., Schmidt, G. A., Salzmann, U., Valdes, P. J., Dowsett, H. J., Jan. 2010. Earth system sensitivity inferred from Pliocene modelling and data. Nature Geoscience 3 (1), 60–64.

MacDonald, R., Sakshaug, E., Stein, R., 2004. The Arctic Ocean: modern status and recent climate change. In: Stein, R., MacDonald, R. W. (Eds.), The organic carbon cycle in the Arctic Ocean. Springer, Heidelberg, pp. 6–21.

Macdonald, R. W., Bewers, J. M., 1996. Contaminants in the arctic marine environment: priorities for protection. ICES Journal of Marine Science: Journal du Conseil 53 (3), 537–563.

Marsland, S. J., Haak, H., Jungclaus, J. H., Latif, M., Röske, F., 2003. The Max-Planck-Institute global ocean/sea ice model with orthogonal curvilinear coordinates. Ocean Modelling 5 (2), 91–127.

Martinson, D., Pitman, W., 2007. The Arctic as a trigger for glacial terminations. Climatic Change 80, 253–263.

McIntosh, S. K., McIntosh, R. J., 1983. Current directions in West-African prehistory. Annual Review of Anthropology 12, 215–258.

Meinshausen, M., Smith, S. J., Calvin, K., Daniel, J. S., Kainuma, M. L. T., Lamarque, J.-F., Matsumoto, K., Montzka, S. A., Raper, S. C. B., Riahi, K., Thomson, A., Velders, G. J. M., Vuuren, D. P. P., 2011. The RCP greenhouse gas concentrations and their extensions from 1765 to 2300. Climatic Change 109 (1-2), 213–241.

Meland, M. Y., Jansen, E., Elderfield, H., 2005. Constraints on SST estimates for the northern North Atlantic/Nordic Seas during the LGM: Multiproxy Approach for the Reconstruction of the Glacial Ocean surface. Quaternary Science Reviews 24 (7-9), 835–852.

Micheels, A., Bruch, A. A., Eronen, J., Fortelius, M., Harzhauser, M., Utescher, T., Mosbrugger, V., 2011. Analysis of heat transport mechanisms from a Late Miocene model experiment with a fully-coupled atmosphere-ocean general circulation model. Palaeogeography, Palaeoclimatology, Palaeoecology 304 (3–4), 337–350, the Neogene of Eurasia: Spatial gradients and temporal trends - The second synthesis of NECLIME.

Micheels, A., Eronen, J., Mosbrugger, V., 2009. The Late Miocene climate response to a modern Sahara desert. Global and Planetary Change 67 (3–4), 193–204.

Milankovitch, M., 1941. Canon of insolation and the ice-age problem (Kanon der Erdbestrahlung und seine Anwendung auf das Eiszeitenproblem) Belgrade, 1941. Jerusalem, Israel Program for Scientific Translations;[available from US Dept. of Commerce, Clearinghouse for Federal Scientific and Technical Information, Springfield, Va.] 1969. 1.

Moran, K., Backman, J., Brinkhuis, H., Clemens, S. C., Cronin, T., Dickens, G. R., Eynaud, F., Gattacceca, J., Jakobsson, M., Jordan, R. W., Kaminski, M., King, J., Koc, N., Krylov, A., Martinez, N., Matthiessen, J., McInroy, D., Moore, T. C., Onodera, J., O'Regan, M., Palike, H., Rea, B., Rio, D., Sakamoto, T., Smith, D. C., Stein, R., St John, K., Suto, I., Suzuki, N., Takahashi, K., Watanabe, M., Yamamoto, M., Farrell, J., Frank, M., Kubik, P., Jokat, W., Kristoffersen, Y., JUN 1 2006. The Cenozoic palaeoenvironment of the Arctic Ocean. Nature 441 (7093), 601–605.

Mudelsee, M., Raymo, M. E., 2005. Slow dynamics of the Northern Hemisphere glaciation. Paleoceanography 20 (4), PA4022.

Müller, J., Massé, G., Stein, R., Belt, S. T., 2009. Variability of sea-ice conditions in the Fram Strait over the past 30,000 years. Nature Geoscience 2 (11), 772–776.

National Snow and Ice Data Center (NSIDC), 1997. Joint U.S. Russian Atlas of the Arctic Ocean, Oceanography Atlas for the Winter Period.

Nicholson, S. E., Tucker, C. J., Ba, M. B., May 1998. Desertification, Drought, and Surface Vegetation: An Example from the West African Sahel. Bulletin of the American Meteorological Society 79 (5), 815–829.

NOAA, 1988. Data Announcement 88-MGG-02, Digital relief of the Surface of the Earth.

Nørgaard-Pedersen, N., Spielhagen, R. F., Erlenkeuser, H., Grootes, P. M., Heinemeier, J., Knies, J., 2003. Arctic Ocean during the Last Glacial Maximum: Atlantic and polar domains of surface water mass distribution and ice cover. Paleoceanography 18 (3), 1063.

Nørgaard-Pedersen, N., Spielhagen, R. F., Thiede, J., Kassens, H., 1998. Central Arctic Surface Ocean Environment During the Past 80,000 Years. Paleoceanography 13 (2), 193–204.

Nürnberg, D., Wollenburg, I., Dethleff, D., Eicken, H., Kassens, H., Letzig, T., Reimnitz, E., Thiede, J., 1994. Sediments in Arctic sea ice: Implications for entrainment, transport and release. Marine Geology 119 (3-4), 185–214.

O'ishi, R., Abe-Ouchi, A., 2011. Polar amplification in the mid-Holocene derived from dynamical vegetation change with a GCM. Geophysical Research Letters 38 (14), L14702.

Otto, J., Raddatz, T., Claussen, M., 2009a. Climate variability-induced uncertainty in mid-Holocene atmosphere-ocean-vegetation feedbacks. Geophysical Research Letters 36 (23), L23710.

Otto, J., Raddatz, T., Claussen, M., 2011. Strength of forest-albedo feedback in mid-Holocene climate simulations. Climate of the Past 7 (3), 1027–1039.

Otto, J., Raddatz, T., Claussen, M., Brovkin, V., Gayler, V., 2009b. Separation of atmosphere-ocean-vegetation feedbacks and synergies for mid-Holocene climate. Geophysical Research Letters 36 (9), L09701.

Otto-Bliesner, B. L., Upchurch, G. R., 1997. Vegetation-induced warming of high-latitude regions during the Late Cretaceous period. Nature 385, 804–807.

Pagani, M., Liu, Z., LaRiviere, J., Ravelo, A. C., JAN 2010. High Earth-system climate sensitivity determined from Pliocene carbon dioxide concentrations. Nature Geoscience 3 (1), 27–30.

Pagani, M., Zachos, J. C., Freeman, K. H., Tipple, B., Bohaty, S., 2005. Marked Decline in Atmospheric Carbon Dioxide Concentrations During the Paleogene. Science 309 (5734), 600–603.

Paillard, D., 2001. Glacial cycles: Toward a new paradigm. Reviews of Geophysics 39 (3), 325–346.

PALEOSENS Project Members; Rohling, E., Sluijs, A., Dijkstra, H., Köhler, P., van de Wal, R., von der Heydt, A., Beerling, D., Berger, A., Bijl, P., Crucifix, M., Deconto, R., Drijfhout, S. S., Fedorov, A., Foster, G. L., Ganopolski, A., Hansen, J., Hönisch, B., Hooghiemstra, H., Huber, M., Huybers, P., Knutti, R., Lea, D. W., Lourens, L. J., Lunt, D., Masson-Demotte, V., Medina-Elizalde, M., Otto-Bliesner, B., Pagani, M., Pälike, H., Renssen, H., Royer, D. L., Siddall, M., Valdes, P., Zachos, J. C., Zeebe, R. E., 2012. Making sense of palaeoclimate sensitivity. Nature 491, 683–691.

Paul, A., Schäfer-Neth, C., 2003. Modeling the water masses of the Atlantic Ocean at the Last Glacial Maximum. Paleoceanography 18 (3), 1058.

Petit, J.-R., Jouzel, J., Raynaud, D., Barkov, N., Barnola, J.-M., Basile, I., Bender, M., Chappellaz, J., Davis, M., Delaygue, G., Delmotte, M., Kotlyakov, V. M., Legrand, M., Lipenkov, V. Y., Lorius, C., Pepin, L., Ritz, C., Saltzman, E., Stievenard, M., 1999. Climate and atmospheric history of the past 420,000 years from the Vostok ice core, Antarctica. Nature 399 (6735), 429–436.

Petit-Maire, N., 1989. Interglacial environments in presently hyperarid sahara: Palaeoclimatic implications. In: Leinen, M., Sarnthein, M. (Eds.), Paleoclimatology and Paleometeorology: Modern and Past Patterns of Global Atmospheric Transport. Vol. 282 of NATO ASI Series. Springer Netherlands, pp. 637–661.

Petit-Maire, N., Riser, J., 1981. Holocene lake deposits and palaeoenvironments in Central Sahara, Northeastern Mali. Palaeogeography, Palaeoclimatology, Palaeoecology 35 (0), 45–61.

Pfirman, S., GASCARD, J.-C., Wollenburg, I., Mudie, P., Abelmann, A., 1989. Particle-laden Eurasian Arctic sea ice: observations from July and August 1987. Polar Research 7 (1), 59–66.

Pflaumann, U., Sarnthein, M., Chapman, M., d'Abreu, L., Funnell, B., Huels, M., Kiefer, T., Maslin, M., Schulz, H., Swallow, J., van Kreveld, S., Vautravers, M., Vogelsang, E., Weinelt, M., 2003. Glacial North Atlantic: Sea-surface conditions reconstructed by GLAMAP 2000. Paleoceanography 18 (3), 1065.

Phillips, R. L., Grantz, A., 2001. Regional variations in provenance and abundance of ice-rafted clasts in Arctic Ocean sediments: implications for the configuration of late Quaternary oceanic and atmospheric circulation in the Arctic. Marine Geology 172 (1-2), 91–115.

Pälike, H., Spofforth, D. J. A., O'Regan, M., Gattacceca, J., 2008. Orbital scale variations and timescales from the Arctic Ocean. Paleoceanography 23 (1), PA1S10.

Polyak, L., Alley, R. B., Andrews, J. T., Brigham-Grette, J., Cronin, T. M., Darby, D. A., Dyke, A. S., Fitzpatrick, J. J., Funder, S., Holland, M., Jennings, A. E., Miller, G. H., O'Regan, M., Savelle, J., Serreze, M., St. John, K., White, J. W. C., Wolff, E., 2010. History of sea ice in the Arctic: Special Theme: Arctic Palaeoclimate Synthesis (PP. 1674-1790). Quaternary Science Reviews 29 (15–16), 1757–1778.

Polyak, L., Curry, W. B., Darby, D. A., Bischof, J., Cronin, T. M., 2004. Contrasting glacial/interglacial regimes in the western Arctic Ocean as exemplified by a sedimentary

record from the Mendeleev Ridge. Palaeogeography, Palaeoclimatology, Palaeoecology 203 (1–2), 73–93.

Polyak, L., Darby, D. A., Bischof, J. F., Jakobsson, M., 2007. Stratigraphic constraints on late Pleistocene glacial erosion and deglaciation of the Chukchi margin, Arctic Ocean. Quaternary Research 67 (2), 234–245.

Polyak, L., Edwards, M. H., Coakley, B. J., Jakobsson, M., 2001. Ice shelves in the Pleistocene Arctic Ocean inferred from glaciogenic deep-sea bedforms. Nature 410 (6827), 453–457.

Prange, M., Lohmann, G., 2003. Effects of mid-Holocene river runoff on the Arctic ocean/sea-ice system: a numerical model study. Holocene 13 (3), 335–342.

Prentice, I. C., Cramer, W., Harrison, S. P., Leemans, R., Monserud, R. A., Solomon, A. M., 1992. Special Paper: A Global Biome Model Based on Plant Physiology and Dominance, Soil Properties and Climate. Journal of Biogeography 19 (2), 117–134.

Prentice, I. C., Jolly, D., BIOME 6000 participants, 2000. Mid-Holocene and glacial-maximum vegetation geography of the northern continents and Africa. Journal of Biogeography 27 (3), 507–519.

Raddatz, T. J., Reick, C. H., Knorr, W., Kattge, J., Roeckner, E., Schnur, R., Schnitzler, K.-G., Wetzel, P., Jungclaus, J., 2007. Will the tropical land biosphere dominate the climate–carbon cycle feedback during the twenty-first century? Climate Dynamics 29 (6), 565–574.

Ravelo, A. C., Andreasen, D. H., Lyle, M., Lyle, A. O., Wara, M. W., 2004. Regional climate shifts caused by gradual global cooling in the Pliocene epoch. Nature 429 (6989), 263–267.

Raymo, M., Grant, B., Horowitz, M., Rau, G., 1996. Mid-Pliocene warmth: stronger greenhouse and stronger conveyor . Marine Micropaleontology 27 (1–4), 313–326.

Raymo, M. E., Huybers, P., 2008. Unlocking the mysteries of the ice ages. Nature 451, 284–285.

Rechid, D., Raddatz, T. J., Jacob, D., 2009. Parameterization of snow-free land surface albedo as a function of vegetation phenology based on MODIS data and applied in climate modelling. Theoretical and Applied Climatology 95 (3-4), 245–255.

Reimnitz, E., McCormick, M., Bischof, J., Darby, D. A., 1998. Comparing sea-ice sediment load with Beaufort Sea shelf deposits; is entrainment selective? Journal of Sedimentary Research 68 (5), 777–787.

Rimbu, N., Lohmann, G., Kim, J.-H., Arz, H. W., Schneider, R., 2003. Arctic/North Atlantic Oscillation signature in Holocene sea surface temperature trends as obtained from alkenone data. Geophysical Research Letters 30 (6), 1280.

Roeckner, E., Arpe, K., Bengtsson, L., Brinkop, S., Dümenil, L., Esch, M., Kirk, E., Lunkeit, F., Ponater, M., Rockel, B., Sausen, R., Schlese, U., Schubert, S., Windelband, M. (Eds.), 1992. Simulation of the present-day climate with ECHAM model: impact of model physics and resolution. Report 93. Hamburg.

Roeckner, E., Bäuml, G., Bonaventura, L., Brokopf, R., Esch, M., Giorgetta, M., Hagemann, S., Kirchner, I., Kornblueh, L., Manzini, E., Rhodin, A., Schlese, U., Schulzweida, U., Tompkins, A., 2003. The atmospheric general circulation model ECHAM5. PART I: Model description. Max- Planck-Institut für Meteorologie, Hamburg, Rep 349.

Roeckner, E., Brokopf, R., Esch, M., Giorgetta, M., Hagemann, S., Kornblueh, L., Manzini, E., Schlese, U., Schulzweida, U., 2006. Sensitivity of simulated climate to horizontal and vertical resolution in the ECHAM5 atmosphere model. Journal of Climate 19 (16), 3771–3791.

Rojas, M., Moreno, P., Kageyama, M., Crucifix, M., Hewitt, C., Abe-Ouchi, A., Ohgaito, R., Brady, E. C., Hope, P., 2009. The Southern Westerlies during the last glacial maximum in PMIP2 simulations. Climate Dynamics 32 (4), 525–548.

Romanova, V., Prange, M., Lohmann, G., 2004. Stability of the glacial thermohaline circulation and its dependence on the background hydrological cycle. Climate Dynamics 22, 527–538.

Ruddiman, W. F., 2006a. Ice-driven CO_2 feedback on ice volume. Climate of the Past 2 (1), 43–55.

Ruddiman, W. F., 2006b. Orbital changes and climate. Quaternary Science Reviews 25 (23–24), 3092–3112.

Ruddiman, W. F., 2010. A Paleoclimatic Enigma? Science 328 (5980), 838–839.

Salzmann, U., Dolan, A., Haywood, A., Chan, W.-L., Hill, D., Abe-Ouchi, A., Otto-Bliesner, B., Bragg, F., Chandler, M., Contoux, C., Jost, A., Kamae, Y., Lohmann, G., Lunt, D., Pickering, S., Pound, M., Ramstein, G., Rosenbloom, N., Sohl, L., Stepanek, C., Ueda, H., Zhang, Z., in revision. How well do models reproduce warm terrestrial climates of the Pliocene? Nature Climate Change.

Sangiorgi, F., van Soelen, E. E., Spofforth, D. J. A., Pälike, H., Stickley, C. E., St. John, K., Koç, N., Schouten, S., Sinninghe Damsté, J. S., Brinkhuis, H., 2008. Cyclicity in the middle Eocene central Arctic Ocean sediment record: Orbital forcing and environmental response. Paleoceanography 23 (1), PA1S08.

Schodlok, M. P., Hellmer, H. H., Rohardt, G., Fahrbach, E., 2006. Weddell Sea iceberg drift: Five years of observations. Journal of Geophysical Research 111 (C6), C06018.

Schurgers, G., Mikolajewicz, U., Groeger, M., Maier-Reimer, E., Vizcaino, M., Winguth, A., 2007. The effect of land surface changes on Eemian climate. Climate Dynamics 29 (4), 357–373.

Semenov, V. A., Park, W., Latif, M., 2009. Barents Sea inflow shutdown: A new mechanism for rapid climate changes. Geophysical Research Letters 36 (14), L14709.

Seneviratne, S. I., Corti, T., Davin, E. L., Hirschi, M., Jaeger, E. B., Lehner, I., Orlowsky, B., Teuling, A. J., 2010. Investigating soil moisture–climate interactions in a changing climate: A review. Earth-Science Reviews 99 (3–4), 125–161.

Seneviratne, S. I., Koster, R. D., Guo, Z., Dirmeyer, P. A., Kowalczyk, E., Lawrence, D., Liu, P., Mocko, D., Lu, C.-H., Oleson, K. W., Verseghy, D., 2006. Soil Moisture Memory in AGCM Simulations: Analysis of Global Land–Atmosphere Coupling Experiment (GLACE) Data. Journal of Hydrometeorology 7 (5), 1090–1112.

Shellito, C. J., Sloan, L. C., 2006. Reconstructing a lost Eocene Paradise, Part II: On the utility of dynamic global vegetation models in pre-Quaternary climate studies. Global and Planetary Change 50 (1–2), 18–32.

Shevenell, A. E., Kennett, J. P., Lea, D. W., 2004. Middle Miocene Southern Ocean Cooling and Antarctic Cryosphere Expansion. Science 305 (5691), 1766–1770.

Shin, S.-I., Liu, Z., Otto-Bliesner, B., Brady, E., Kutzbach, J., Harrison, S., 2003a. A Simulation of the Last Glacial Maximum climate using the NCAR-CCSM. Climate Dynamics (20), 127–151.

Shin, S.-I., Liu, Z., Otto-Bliesner, B. L., Kutzbach, J. E., Vavrus, S. J., 2003b. Southern Ocean sea-ice control of the glacial North Atlantic thermohaline circulation. Geophysical Research Letters 30 (2), 1096.

Siegert, M. J., Dowdeswell, J. A., 2004. Numerical reconstructions of the Eurasian Ice Sheet and climate during the Late Weichselian: Quaternary Environments of the Eurasian North (QUEEN). Quaternary Science Reviews 23 (11-13), 1273–1283.

Siegert, M. J., Marsiat, I., 2001. Numerical reconstructions of LGM climate across the Eurasian Arctic. Quaternary Science Reviews 20 (15), 1595–1605.

Sloan, L., Morrill, C., 1998. Orbital forcing and Eocene continental temperatures. Palaeogeography, Palaeoclimatology, Palaeoecology 144 (1–2), 21–35.

Sloan, L. C., Pollard, D., 1998. Polar stratospheric clouds: A high latitude warming mechanism in an ancient greenhouse world. Geophysical Research Letters 25 (18), 3517–3520.

Sloan, L. C., Walker, J. C. G., Moore, T. C., 1995. Possible role of oceanic heat transport in Early Eocene climate. Paleoceanography 10 (2), 347–356.

St. John, K., 2008. Cenozoic ice-rafting history of the central Arctic Ocean: Terrigenous sands on the Lomonosov Ridge. Paleoceanography 23 (1), PA1S05.

Stärz, M., Gong, X., Stein, R., Darby, D. A., Kauker, F., Lohmann, G., 2012. Glacial shortcut of Arctic sea-ice transport. Earth and Planetary Science Letters 357–358 (0), 257–267.

Stärz, M., Lohmann, G., Knorr, G., 2013. Dynamic soil feedbacks on the climate of the mid-Holocene and the Last Glacial Maximum. Climate of the Past Discussions 9 (3), 2717–2770.

Steele, M., Ermold, W., Häkkinen, S., Holland, D., Holloway, G., Karcher, M., Kauker, F., Maslowski, W., Steiner, N., Zhang, J., 2001. Adrift in the Beaufort Gyre: A model intercomparison. Geophysical Research Letters 28 (15), 2935–2938.

Stein, R., 2008. Arctic ocean sediments: Processes, proxies, and paleoenvironment: Developments in Marine Geology, 2. Elsevier, Amsterdam. 592 pp, 1st Edition. Elsevier Science, Amsterdam and Boston and London.

Stein, R., Schubert, C., Vogt, C., Fütterer, D., 1994. Stable isotope stratigraphy, sedimentation rates, and salinity changes in the Latest Pleistocene to Holocene eastern central Arctic Ocean. Marine Geology 119 (3-4), 333–355.

Stein, U., Alpert, P., 1993. Factor Separation in Numerical Simulations. Journal of Atmospheric Sciences 50 (14), 2107–2115.

Steiner, N., Harder, M., Lemke, P., 1999. Sea ice roughness and drag coefficients in a dynamic-thermodynamic sea ice model for the Arctic. Tellus 51, 964–978.

Stepanek, C., Lohmann, G., 2012. Modelling mid-Pliocene climate with COSMOS. Geoscientific Model Development, 1221–1243.

Stokes, C. R., Clark, C. D., Darby, D. A., Hodgson, D. A., 2005. Late Pleistocene ice export events into the Arctic Ocean from the M'Clure Strait Ice Stream, Canadian Arctic Archipelago. Global and Planetary Change 49 (3-4), 139–162.

Stokes, C. R., Clark, C. D., Winsborrow, M. C. M., 2006. Subglacial bedform evidence for a major palaeo-ice stream and its retreat phases in Amundsen Gulf, Canadian Arctic Archipelago. Journal of Quaternary Science 21 (4), 399–412.

Stuut, J.-B. W., Lamy, F., 2004. Climate variability at the southern boundaries of the Namib (southwestern Africa) and Atacama (northern Chile) coastal deserts during the last 120,000 yr. Quaternary Research 62 (3), 301–309.

Sundqvist, H. S., Zhang, Q., Moberg, A., Holmgren, K., Körnich, H., Nilsson, J., Brattström, G., 2010a. Climate change between the mid and late Holocene in northern high latitudes — Part 1: Survey of temperature and precipitation proxy data. Climate of the Past 6 (5), 591–608.

Sundqvist, H. S., Zhang, Q., Moberg, A., Holmgren, K., Körnich, H., Nilsson, J., Brattström, G., 2010b. Corrigendum to "Climate change between the mid and late Holocene in northern high latitudes — Part 1: Survey of temperature and precipitation proxy data" published in Clim. Past, 6, 591–608, 2010. Climate of the Past 6 (5), 739–743.

Texier, D., Noblet, N. d., Braconnot, P., 2000. Sensitivity of the African and Asian Monsoons to Mid-Holocene Insolation and Data-Inferred Surface Changes. Journal of Climate 13 (1), 164–181.

Texier, D., Noblet, N. d., Harrison, S. P., Haxeltine, A., Jolly, D., Joussaume, S., Laarif, F., Prentice, I. C., Tarasov, P., 1997. Quantifying the role of biosphere-atmosphere feedbacks in climate change: coupled model simulations for 6000 years BP and comparison with palaeodata for northern Eurasia and northern Africa. Climate Dynamics 13 (12), 865–882.

Tiedemann, R., Sarnthein, M., Shackleton, N. J., 1994. Astronomic timescale for the Pliocene Atlantic $\delta^{18}O$ and dust flux records of Ocean Drilling Program Site 659. Paleoceanography 9 (4), 619–638.

Timco, G. W., Frederking, R. M. W., 1990. Compressive strength of sea ice sheets. Cold Regions Science and Technology 17 (3), 227–240.

Timco, G. W., Weeks, W. F., 2010. A review of the engineering properties of sea ice. Cold Regions Science and Technology 60 (2), 107–129.

Tripati, A. K., Roberts, C. D., Eagle, R. A., 2009. Coupling of CO2 and Ice Sheet Stability Over Major Climate Transitions of the Last 20 Million Years. Science 326 (5958), 1394–1397.

Tuenter, E., Weber, S. L., Hilgen, F. J., Lourens, L. J., 2005. Sea-ice feedbacks on the climatic response to precession and obliquity forcing. Geophysical Research Letters 32 (24), L24704.

Valdes, P., 2011. Built for stability. Nature Geoscience 4 (7), 414–416.

Vamborg, F. S. E., Brovkin, V., Claussen, M., 2011. The effect of a dynamic background albedo scheme on Sahel/Sahara precipitation during the mid-Holocene. Climate of the Past 7 (1), 117–131.

van de Wal, R. S. W., de Boer, B., Lourens, L. J., Köhler, P., Bintanja, R., 2011. Reconstruction of a continuous high-resolution CO_2 record over the past 20 million years. Climate of the Past 7 (4), 1459–1469.

Varma, V., Prange, M., Merkel, U., Kleinen, T., Lohmann, G., Pfeiffer, M., Renssen, H., Wagner, A., Wagner, S., Schulz, M., 2012. Holocene evolution of the Southern Hemisphere westerly winds in transient simulations with global climate models. Climate of the Past 8 (2), 391–402.

Velichko, A. A., Kononov, Y. M., Faustova, M. A., 1997. The last glaciation of earth: Size and volume of ice-sheets. Quaternary International 41-42 (0), 43–51.

Vernal, A. d., Rosell-Melé, A., Kucera, M., Hillaire-Marcel, C., Eynaud, F., Weinelt, M., Dokken, T., Kageyama, M., 2006. Comparing proxies for the reconstruction of LGM sea-surface conditions in the northern North Atlantic. Quaternary Science Reviews 25 (21–22), 2820–2834.

Vinje, T., 2001. Fram Strait Ice Fluxes and Atmospheric Circulation: 1950–2000. Journal of Climate 14 (16), 3508–3517.

Vinje, T., Nordlund, N., Kvambekk, Å., 1998. Monitoring ice thickness in Fram Strait. Journal of Geophysical Research 103 (C5), 10437–10449.

Vogt, C., Knies, J., Spielhagen, R. F., Stein, R., 2001. Detailed mineralogical evidence for two nearly identical glacial/deglacial cycles and Atlantic water advection to the Arctic Ocean during the last 90,000 years: The late Quaternary stratigraphy and environments of northern Eurasia and the adjacent Arctic seas - new contributions from QUEEN. Global and Planetary Change 31 (1–4), 23–44.

Waelbroeck, C., Paul, A., Kucera, M., Rosell-Mele, A., Weinelt, M., Schneider, R., Mix, A. C., Abelmann, A., Armand, L., Bard, E., Barker, S., Barrows, T. T., Benway, H., Cacho, I., Chen, M. T., Cortijo, E., Crosta, X., de Vernal, A., Dokken, T., Duprat, J., Elderfield, H., Eynaud, F., Gersonde, R., Hayes, A., Henry, M., Hillaire-Marcel, C., Huang,

C. C., Jansen, E., Juggins, S., Kallel, N., Kiefer, T., Kienast, M., Labeyrie, L., Leclaire, H., Londeix, L., Mangin, S., Matthiessen, J., Marret, F., Meland, M., Morey, A. E., Mulitza, S., Pflaumann, U., Pisias, N. G., Radi, T., Rochon, A., Rohling, E. J., Sbaffi, L., Schaefer-Neth, C., Solignac, S., Spero, H., Tachikawa, K., Turon, J. L., Members, M. P., FEB 2009. Constraints on the magnitude and patterns of ocean cooling at the Last Glacial Maximum. Nature Geoscience 2 (2), 127–132.

Wang, G., 2005. Agricultural drought in a future climate: results from 15 global climate models participating in the IPCC 4th assessment. Climate Dynamics 25 (7–8), 739–753.

Wang, H. J., 1999. Role of vegetation and soil in the Holocene megathermal climate over China. Journal of Geophysical Research-Atmospheres 104 (D8), 9361–9367.

Wanner, H., Beer, J., Bütikofer, J., Crowley, T. J., Cubasch, U., Flückiger, J., Goosse, H., Grosjean, M., Joos, F., Kaplan, J. O., Küttel, M., Müller, S. A., Prentice, I. C., Solomina, O., Stocker, T. F., Tarasov, P., Wagner, M., Widmann, M., 2008. Mid- to Late Holocene climate change: an overview. Quaternary Science Reviews 27 (19–20), 1791–1828.

Wei, W., Lohmann, G., 2012. Simulated Atlantic Multidecadal Oscillation during the Holocene. Journal of Climate 25 (20), 6989–7002.

Wei, W., Lohmann, G., Dima, M., 2012. Distinct Modes of Internal Variability in the Global Meridional Overturning Circulation Associated with the Southern Hemisphere Westerly Winds. Journal of Physical Oceanography 42 (5), 785–801.

Willeit, M., Ganopolski, A., Feulner, G., 2013. On the effect of orbital forcing on mid-Pliocene climate, vegetation and ice sheets. Climate of the Past Discussions 9, 1703–1734.

Williamson, D. L., Kiehl, J. T., Ramanathan, V., Dickinson, R. E., Hack, J. J., 1987. Description of NCAR community climate model (CCM1). Climate and Global Dynamics Division, National Center for Atmospheric Research, Boulder, Colorado.

Wohlfahrt, J., Harrison, S. P., Braconnot, P., 2004. Synergistic feedbacks between ocean and vegetation on mid- and high-latitude climates during the mid-Holocene. Climate Dynamics 22 (2-3), 223–238.

Zachos, J., Thomas, E., Billups, K., Apr. 2001. Trends, Rhythms, and Aberrations in Global Climate 65 Ma to Present. Science 292 (5517), 686–693.

Zhang, X., Lohmann, G., Knorr, G., Xu, X., 2012. Two ocean states during the Last Glacial Maximum. Climate of the Past Discussions 8, 3015–3041.

Zhao, Y., Braconnot, P., Marti, O., Harrison, S. P., Hewitt, C., Kitoh, A., Liu, Z., Mikolajewicz, U., Otto-Bliesner, B., Weber, S. L., 2005. A multi-model analysis of the role of the ocean on the African and Indian monsoon during the mid-Holocene. Climate Dynamics 25 (7-8), 777–800.

Acknowledgments

First and foremost, I wish to thank my supervisor Gerrit Lohmann, for supporting me during my doctoral studies. His pleasant kind and humor made any discussion, whether in the office or on the rails, enjoyable and motivating. Hopefully, he maintains this kind of personality and his roguish enthusiasm, for the benefit of present and future students and colleagues, as long as possible.

I am thankful to Arne Micheels for his remote supervision and for introducing me to the renowned Senckenberg Research Institute. Its exciting natural history museum revived my childhood memories. I wish Arne the best for his private life and future career.

Thanks are dedicated to Rüdiger Stein and the marine geology group for introducing me to the AWI.

Further thanks are addressed to my helpful PhD committee members Jens Matthießen, Gregor Knorr and Christian Stepanek, who were hopefully pacified with enough of my nut triangles and rum balls.

Here, I also want to mention the comfortable atmosphere within the group of paleoclimate dynamics, which is sustained by our head, the senior scientists, postdocs, students and our pleasant secretary Stefanie Klebe.

Thanks to the organizers of the graduate school POLMAR, for some highlights, which splitted my normal working routine into digestible portions, and for a feeling of community, which is difficult to establish at a large institute as the AWI.

All the other unmentioned friends, flatmates, colleagues or a combination of these, should not feel forgotten. Regardless of whether we stay in contact or not, I will remember the moments we shared.